TOROIDAL INSTABILITIES IN THE PRESENCE OF CHARGE AND NON-NEWTONIAN FLUIDS

A Dissertation
Presented to
The Academic Faculty

By

Alexandros A. Fragkopoulos

In Partial Fulfillment
of the Requirements for the Degree
Doctor of Philosophy in the
School of Physics

Georgia Institute of Technology

August 2017

TOROIDAL INSTABILITIES IN THE PRESENCE OF CHARGE AND NON-NEWTONIAN FLUIDS

Approved by:

Professor Alberto Fernandez-Nieves, Advisor
School of Physics
Georgia Institute of Technology

Professor Paul Goldbart
School of Physics
Georgia Institute of Technology

Professor Michael Schatz
School of Physics
Georgia Institute of Technology

Professor Minami Yoda
School of Mechanical Engineering
Georgia Institute of Technology

Professor Justin Burton
Department of Physics
Emory University

Date Approved: April 28, 2017

In all things of nature there is something of the marvelous.

Aristotle

To everyone who has been there for me during this journey.

Thank you for the support all these year.

ACKNOWLEDGEMENTS

Firstly, I would like to express my gratitude to my advisor Prof. Alberto Fernandez-Nieves for the support of my Ph.D study, for his continuous motivation, and immense knowledge. His drive for excellence, enthusiasm, and knowledge helped me become the scientist I am.

Besides my advisor, I would like to thank the rest of my thesis committee: Prof. Paul Goldbart, Prof. Justin Burton, Prof. Minami Yoda, and Prof. Michael Schatz. A special thanks goes to Prof. Minami Yoda for being a great teacher, as well as having some insightful and helpful discussions.

I would like to thank members of the Fernandez lab past and present. Prof. Josefa Guerrero for her help and mentoring when I first joined the lab and for enduring me as an officemate all these years. The many early discussions laid the foundation of my understanding for my research. Perry Ellis for the many hours we spent working on homework, as well as countless discussions around our research, and of course for his support and encouragement as a friend. Prof. Ya-Wen Chang (aka Winnie!) who was always willing to spend time and help with any technical problem. I would like to thank the undergraduate students that I worked with over the past few years. Eric Berger performed many of the experiments and analysis using particle image velocimetry presented in Chapter 2. Aaron Aizenman carried experiments and analysis on viscous fingering presented at the end of Chapter 3. Finally, Luka Marinkovic, a high school student at the time, spent a few months in the lab and performed some of the experiments on the breakup of droplets inside shear-thinning fluids presented in Chapter 4. It was a pleasure working with all of you. I would like to thank Mike T. and Jonas for all the help regarding rheological measurements. Finally, I want to thank the rest of my labmates, John, Ekapop, Mike D., Caleb, and everyone else.

I would like to thank the Georgia Tech School of Physics, the GTfire program, the

Children's Healthcare of Atlanta, the IBB seed grant program, and Procter & Gamble for financial support.

My friends, for being there whenever I needed them; Stefanos, Stavros, and the rest of the crew, but especially Lea, who has been extremely supportive and understanding all these years.

Finally and most importantly, I would like to thank my family, without whom I would not have come to the U.S.A. for my studies and I would not be the person I am today, and specials thank to my mom that has been always there for me.

TABLE OF CONTENTS

LIST OF TABLES

LIST OF FIGURES

CHAPTER 1

INTRODUCTION AND MOTIVATION

Spherical bubbles and droplets are common to our everyday life. They make rain and clouds and are essential constituents of many of the health care and food products we often use and eat. Surface tension gives them their perfect spherical shape by minimizing the surface area for a given volume [1]. As a result, a cylindrical jet is inherently unstable and breaks into spherical droplets. This phenomenon is a direct consequence of the Laplace equation, relating the pressure jump, Δp, across an interface due to a nonzero surface tension, γ. The Laplace pressure is given by $\Delta p = 2\gamma H$, where $H = (\kappa_1 + \kappa_2)/2$ is the mean curvature, with κ_1 and κ_2 the principal curvatures at any point on the surface. For a droplet to be stable, Δp must be constant. As a consequence, only shapes with constant mean curvature can be stable; the sphere is an example, since $H = 1/r$, with r the radius of the sphere, which is constant. As a result, droplets and bubbles with non-constant mean curvature are not stable.

Toroidal droplets are fascinating systems for reasons other than their non-constant mean curvature. A torus has regions of positive, zero and negative Gaussian curvature, $G = \kappa_1 \cdot \kappa_2$. This is very different from the sphere, which is a surface with constant $G = \frac{1}{r^2}$, or even a cylinder for which $G = 0$.

Topologically, the torus also differs from the sphere. The result of integrating G over the whole surface results in a quantity, called the Euler characteristic of the surface, $\chi = \frac{1}{2\pi} \oiint_S G dS'$, which is equal to +2 for a sphere, while it is 0 for a torus. This quantity is an example of a topological invariant of the surface. Surfaces of equal Euler characteristic can be continuously deformed into each other without the need of ever breaking or tearing the surface. We say that these surfaces are topologically equivalent. As a result, a sphere and a torus are topologically distinct, since there is no way to transform a torus into a sphere

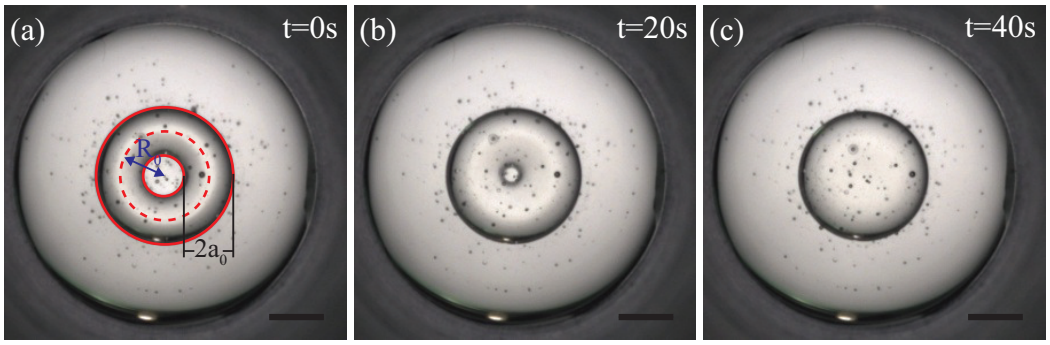

Figure 1.1: (a-c) The evolution of a torus with $\xi \approx 1.9$, illustrating how a torus shrinks over time. In (a) R_0 and a_0 are the central circle and tube radius of a torus, respectively. The scale bars represent a length of 4 mm.

unless we break the torus. In contrast, a cup of coffee with one handle is topologically equivalent to a torus, which also has a handle, as one can bend, stretch and twist the cup of coffee and convert it into a torus without the need of ever tearing the surface apart.

Interestingly, these mathematical differences also result in unusual physical phenomena. The lack of a constant mean curvature, for example, implies a non-constant Laplace pressure, which will cause toroidal droplets to evolve in remarkable ways. In fact, for toroidal droplets with sufficiently small aspect ratio $\xi = R_0/a_0$, where R_0 is the radius of the central circle of the torus and a_0 is the radius of the tube [see Fig. 1.1(a)], the droplet shrinks towards the center to eventually coalesce onto itself and become a single spherical droplet, as shown in Fig. 1.1(a-c) [2]. This shrinking instability is unique to the torus and is not seen for cylindrical jets [3]. The geometric and topological details of the droplet shape can bring about novel effects that are absent in simpler situations. Furthermore, they have rarely been studied before, reflecting in large measure, the difficulty in controllably generating droplets that are topologically different from the sphere.

Another example where the geometry and topology of the surface plays a relevant role is when studying ordered materials, like crystals or liquid crystals, that are forced to live on closed surface, like the sphere or the torus, or that are contained withing closed surfaces. Consider the case of rods on the surface of a sphere that are locally aligned pointing from

the south to the north pole. The two poles are points where the orientation of the rods is undefined, and no matter how we re-orient the rods there is no configuration for which the orientation is everywhere defined. This situation arises with nematic liquid crystals, which are composed of geometrically elongated molecules, aligned on average, along a common direction [4]. The link between the order and the presence of defects is provided by the Poincare-Hopf theorem [5, 6]. For the sphere, this theorem requires the presence of topological defects, which are regions in the material where the characteristic orientational order of the nematic becomes undefined. For the torus, in contrast, there are no defects required. In this case, there is no need to have defects in the order. Since defects play a central role in the response of a material to external mechanical stresses [7, 8], affect the low-temperature thermal conduction of many atomic crystals [9] and can be used as waveguides and cavities for light in photonic applications [10], their presence or not can dramatically affect the physical response of the material. The organization and properties of the ordered material when confined to a sphere or a torus can be dramatically different [11, 12].

In this thesis, we will build on our capability of generating toroidal droplets to study their stability and evolution. We will initially quantify the case of neutral toroidal droplets and then focus on the influence of charge. In this case, the already intriguing evolution of the toroidal droplet, due to its geometry and topology, will become even richer due to the additional effect of electric stresses and the charge distribution on the surface of the droplet as it evolves. The richness in the problem becomes evident after recalling the electrostatics that is involved. Consider an electrical conductor at certain potential. For the sphere, we find that the surface charge density is uniform; this results from solving Gauss' law. This is also true for a cylindrical surface. Now think of a toroidal conductor. In this case, the surface charge density will be larger in the outside of the torus than in the inside of the torus. Hence, the charge density distribution is not homogeneous. Since also the Laplace pressure is not constant, we expect an interesting interplay between electric and surface

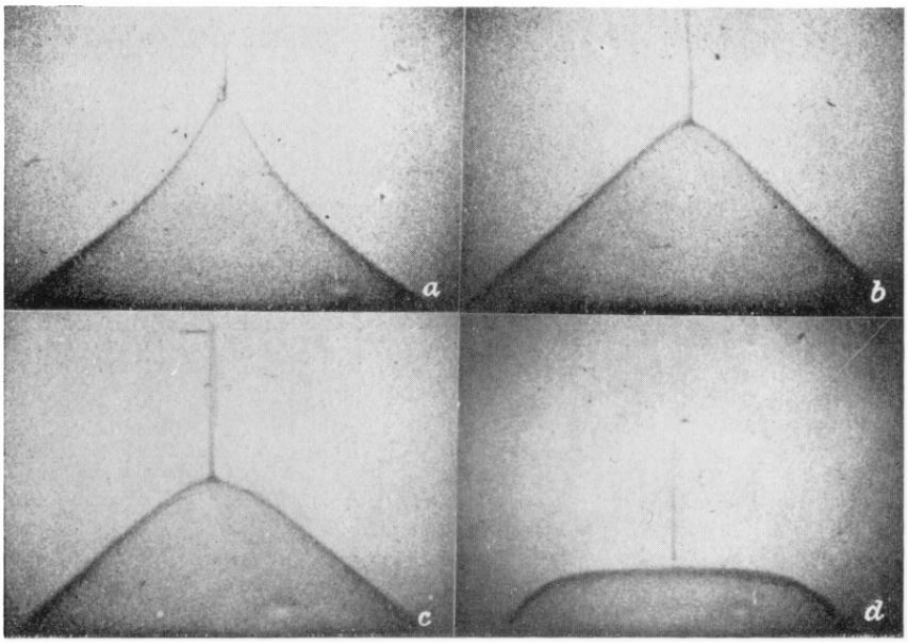

Figure 1.2: A figure from Taylor's paper on cone and jet formation from charged droplets [13], showing the formation of a cone (a) with the formation of a jet, and (b-d) the subsequent collapse.

tension stresses, which has never been considered before. In addition, we often observe that charged tori evolve by producing finger-like structures reminiscent of the Saffman-Taylor instability. Despite the three-dimensional character of our experiments, charge and geometry both combine to allow observing an instability that is most often seen in quasi-two dimensional situations.

In addition, it has been shown that in the thin torus limit, when ξ is high, the torus breaks in a manner reminiscent to the Rayleigh-Plateau instability [2], which refers to the break up of a cylindrical jet into spherical droplets due to capillary forces [14, 15]. Linear stability analysis predicts the size of the droplets that will result from the break up and how fast will the perturbations leading to drop formation develop [16]. Experimental results from neutral toroidal and thin droplets show that the breakup of a torus is in agreement with theory for the breakup of cylindrical jets [2]. As a result, we can use electrified toroidal droplets to study the effect of charge on the Rayleigh-Plateau instability. Note that, charged jets are usually formed by applying an electric field across a liquid droplet at the end of a nozzle

and a ground located at a distance away from the nozzle. Assuming the liquid is an electric conductor, the response of the material to screen the external electric field causes charge to accumulate at the interface. Since liquids are deformable, the electric field at the interface due to the presence of charge is able to stretch the meniscus. However, this deformation is opposed by surface tension. For strong enough electric fields, the only way for the interface to equilibrate surface tension with the electrical stresses is by forming a characteristic conical shape, often referred to as a Taylor cone [13, 17]. At the apex of the cone, where the electric field diverges, the cone gives way to a jet [18–20], which subsequently breaks into drops, as shown in Fig. 1.2. Interestingly, this problem has been theoretically studied by considering the evolution of equipotential jets [21–33]. However, the experimental evolution of charged jets do not conform with these studies. In experiments, the electrified jets are non-equipotential since the dynamics are so fast that the charge does not have time to relax to the interface. However, the dynamics of a toroidal droplet can last as long as tens of seconds, which allows enough time for charge to equilibrate. As a result, by considering the evolution of a charged thin torus, we can test theoretical predictions for equipotential jets.

We can further exploit the fact that a toroidal droplet breaks via the Rayleigh-Plateau instability, to study other breakup phenomena. Motivated by a collaboration with Procter & Gamble, we studied the breakup of toroidal droplets inside non-Newtonian and viscoelastic fluids. The behavior of such materials is very different compared to the behavior of simple fluids. In particular, a viscoelastic fluid in the linear regime exhibits a short time elastic response followed by a long-time viscous flow behavior. As a result, the fluid behaves as a solid for fast deformations, while it flows over long periods of time. Additionally, while for simple fluids, which are Newtonian, the viscosity simply reflects the resistance to shear deformations, viscoelastic liquids can also have an extensional viscosity that reflects the resistance of the liquid to extensional deformations. Experimental results show that the break up time of a viscoelastic jet is increased by many orders of magnitude compared

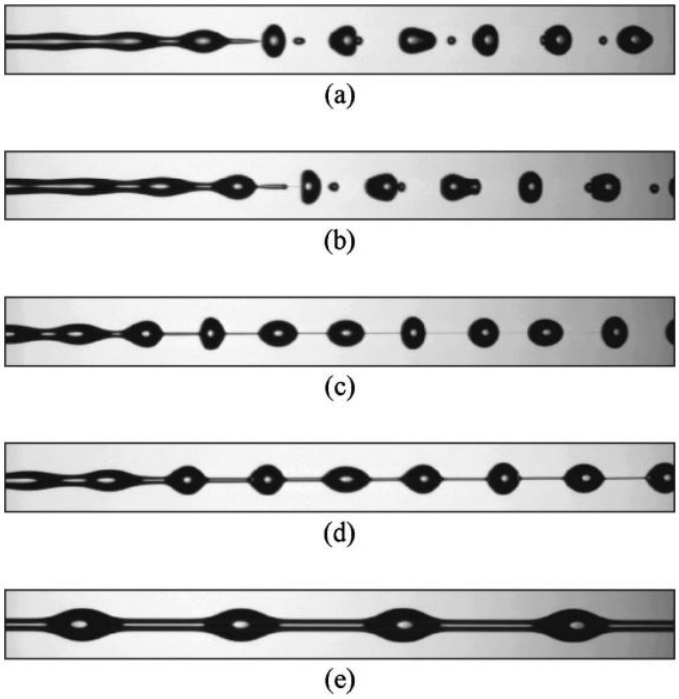

Figure 1.3: Figure taken from [37] showing the break up of (a) Newtonian 50/50 water/glycerol mixture; (b) 0.3% 100 kg/mol PEO; (c) 0.1% 300 kg/mol PEO, (d) 0.05% 1000 kg/mol PEO, and (e) 0.043% 5000 kg/mol PEO.

to Newtonian jets [34, 35], mostly due to the elasticity of the liquid and the fact that the growth of the instability is significantly slowed down once the jet has been considerably stretched. For dilute polymer solutions, the behavior changes as the molecular weight of the polymer increases. While for low molecular weights, the behavior is similar to that of Newtonian liquids, for high molecular weights, the so called beads-on-string configuration is observed [34, 36, 37], as shown in Fig. 1.3.

For the case of non-Newtonian materials, the viscosity can depend on the applied stress or applied shear rate [38]. For a Newtonian liquid, $\sigma = \mu\dot{\varepsilon}$, where σ is the shear stress, $\dot{\varepsilon}$ is the shear rate and μ is the constant viscosity. For non-Newtonian liquids, $\mu = \mu(\dot{\varepsilon})$. When $\mu(\dot{\varepsilon})$ is an increasing function of $\dot{\varepsilon}$, we say the liquid shear thickens. Similarly, when $\mu(\dot{\varepsilon})$ is a decreasing function of $\dot{\varepsilon}$, we say the liquid shear thins. This non-linearity in the viscosity can greatly affect the dynamics of jets made of non-Newtonian fluids; a shear-thickenning jet breaks slower than its Newtonian counterpart, while a shear-thinning fluid

exhibits much more abrupt dynamics [39].

While the break up of bridges [40–54] and jets [34, 55–65] of complex fluids has been extensively studied, the reverse situation, where the outer medium is a complex fluid, has never been looked at. We do this here using toroidal droplets.

Our main goal is to determine how geometry affects the evolution of neutral and charged toroidal droplets. Furthermore, by exploiting the fact that thin toroidal droplets evolve via the Rayleigh-Plateau instability, we study the break up of electrified jets that are equipotential. Finally, we study the evolution of a jet that is surrounded by a non-Newtonian material using toroidal droplets.

The thesis is structured as follows:

In chapter 2, we describe the method used to generate toroidal droplets, and show that these droplets exhibit a unique instability due to their geometry, i.e. they shrink during their evolution. We explore this behavior in detail by performing particle image velocimetry to extract the flow field inside a shrinking toroidal droplet. We compare our experimental results with existing theory, and we use our experiments as a guide to update the existing theory to accurately describe our observations.

In chapter 3, we study the effect of charge on the evolution of toroidal droplets. We find that shrinking can be reversed with the addition of charge leading to expanding tori. In addition, we quantify the effect of charge on the fastest unstable mode causing breakup and compare our results with theoretical predictions. By lowering surface tension, we find that expanding droplets can exhibit viscous fingers, an instability that occurs in quasi-two dimensional systems; we model the transition as a competition between instabilities.

In chapter 4, we study the break up dynamics of a toroidal droplet surrounded by a non-Newtonian fluid. In this case, the droplets resist break-up for long times compare to when we use simple liquids. We show that we can explain our data by incorporating the mechanical non-linearity in the linear theory of Newtonian jets through the strain-rate dependent viscosity.

Finally, in chapter 5, we summarize our results and indicate future work we feel is worth continuing.

CHAPTER 2

THE SHRINKING INSTABILITY OF TOROIDAL DROPLETS

2.1 Introduction

The impact of drops with superhydrophobic surfaces [66], the corona splash that results after a drop hits a liquid bath [67], and the behavior of falling rain drops [68] all involve formation of transient toroidal droplets or rings. These same structures have also been generated and studied via the Leidenfrost mechanism [69]. One thing in common is that all these structures are unstable. This is quite general, as isolated toroidal droplets are unstable and transform into spherical droplets [2, 70–72]. For thin tori, this happens via the Rayleigh-Plateau instability. In contrast, for thick enough toroidal droplets, there is no breakup and the toroidal droplet shrinks until it collapses onto itself to form a single spherical droplet [2]. In the process, the handle of the torus progressively disappears, while concomitantly and due to volume conservation, the tube radius grows. Importantly, this shrinking instability is always present and it is unique to the toroidal shape. Assuming that the cross section of the torus remains circular during the process and that the velocity at the interface is radial, in the reference frame of the circular cross section of the toroidal droplet, calculations of the shrinking speed were consistent with experimental observations [3]. However, recent simulations have found that the cross section does not remain circular, but that it deforms significantly as the torus shrinks [73].

In this chapter, we investigate in depth the shrinking instability and the reason of the discrepancy between theory and simulations, through the use of particle image velocimetry (PIV). We show that when sinking and shrinking are both present, we can use symmetry arguments to extract the flow field associated with only the shrinking instability. We then theoretically address the problem and elucidate which of the many possible modes are

required to capture the evolution and deformation of the toroidal drop.

2.2 Generating Toroidal Droplets

The method we used to generate the toroidal droplets follows the same procedure as in [2]. The setup consists of a rotating stage with a cuvette containing the outer liquid or continuous phase. The cuvette rotates at a constant angular speed, ω, with a metallic needle immersed below the free surface, as shown in Fig. 2.2(a). The inner liquid is then pumped through the needle into the continuous phase to form a curved jet, which in turn closes into itself to form a torus. An important quantity to consider in the generation of a toroidal droplet is the capillary number of the outer fluid, $Ca_o = \mu_o U/\gamma$, where μ_o is the viscosity of the outer liquid, γ the interfacial tension, and $U = \omega R_{tip}$ the speed at the tip of the needle with R_{tip} the distance from the center of rotation to the needle, as shown in Fig. 2.2(b). This capillary number compares the viscous stresses to the stresses due to surface tension. In co-flow microfludic devices, a dripping-to-jetting transition can be induced with Ca_o [74], provided that $We_i < 1$, where $We_i = \frac{\rho_i U\ a}{\gamma}$, with ρ_i the density of the inner fluid and a the radius of the nozzle [75]. The microfluidic device exhibits dripping for $Ca_o < 1$, while jetting for $Ca_o > 1$. This implies that when viscous stresses overcome surface tension stresses, the spherical droplet can be stretched into a jet. Hence, having $Ca_o > 1$ in our experiments is required in order to form a curved jet.

The second important aspect in the generation of toroidal droplets is that the curved jet closes onto itself before the jet breaks [see Fig. 2.2(c)]. The time scale for a jet to break in our experiments can be estimated using the stability analysis of a viscous thread immersed in another viscous liquid [16]. By considering that the initially formed jet has a radius comparable to the radius of the tip, a_{tip}, we find that the relevant time for a jet to break is $t_b \approx \mu_o a_{tip}\ f(\mu_i/\mu_o)/\gamma$, where μ_i is the viscosity of the inner liquid and f a function that depends on the viscosity contrast, μ_i/μ_o [16]. We then compare the breakup time to the time it takes for the curved jet to close onto itself, $T = 2\pi/\omega = 2\pi R_{tip}/U$. If

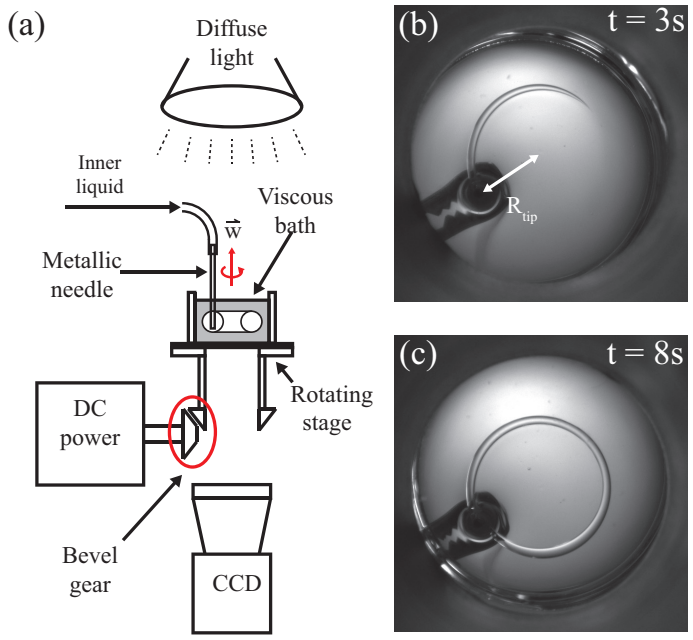

Figure 2.1: (a) A schematic of the experimental setup used to generate toroidal droplets by injecting the inner liquid through a metallic needle into the outer liquid as it rotates at a constant angular velocity, ω. For high enought ω, a curved jet is produced (b) that closes into itself (c) to form a torus.

$t_b > T$, the curved jet closes onto iteself before it breaks, while if $t_b < T$, the jet will break first. This condition can be rewritten in terms of the capillary number of the outer liquid: $Ca_o > (2\pi/f(\mu_i/\mu_o))R_{tip}/a_{tip}$. Experimentally, it has been found that $Ca_o > 2.2R_{tip}/a_{tip}$ is required for a torus to form [2]; in these experiments the inner liquid was a 16 mM sodium dodecyl sulfate solution in water, with $\mu_i \approx 1$ mPa $\cdot$ s, and the outer liquid was a silicone oil with viscosity of $\mu_o > 5000$ mPa $\cdot$ s [2]. Since $\mu_i/\mu_o << 1$, we take $f(\mu_i/\mu_o = 0) = 2$ [16], corresponding to $Ca_o > \pi R_{tip}/a_{tip}$ for the torus to form. This expectation is close to the experimental finding.

Importantly, our setup allows for experimental control over the geometry of the torus; by controlling R_{tip} and the total volume injected, we can modify the values of the radius of the central circle, R_o, and of the tube radius, a_o, of the torus [see Fig. 2.2(a,b)].

Our method for generating toroidal droplets works best if we generate the tori close to the free surface, such that the depth of the needle is close to $2a_0$. However, we are

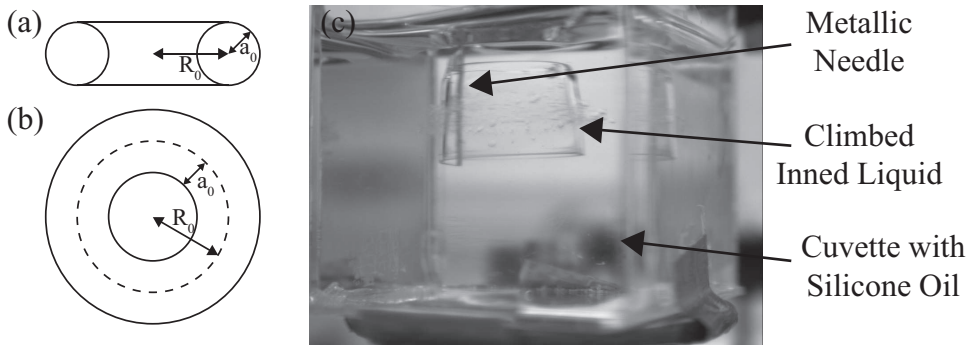

Figure 2.2: A schematic of the geometry of a torus using a (a) side and (b) top view showing the central cirlce radius, R_0, and tube radius, a_0. (c) A side-view of the cuvette containing 30,000 cSt silicone oil as a torus is generated. Due to the viscous stresses, the inner liquid climbs the needle forming a cylindrical sheet rather a torus.

also interested in generating toroidal droplets that are not close to the free surface. The challenge in making such toroids is a "climbing effect" that appears during the generation process and that consists of the inner liquid slowly climbing along the needle; as a result, the torus deforms to become a cylindrical sheet, as shown in Fig. 2.2(c). This effect is amplified as we increase ω and/or by performing many revolutions to make the toroid. Experimentally, we find it best to make a liquid torus with a total number of rotations between 4 and 6. In addition, it is also better to use as low ω as possible. We believe the observed climbing could be due to the high viscous stresses involved in the generation process. Note that we typically use silicone oil with $\mu_0 \geq 30,000$ mPa $\cdot$ s. Hence, if the inner liquid climbs along the needle, the viscous stresses decrease due to the inner liquid acting as a lubrication layer around the needle.

2.3 Shrinking Instability

A toroidal droplet is unstable and tries to minimize its surface area is due to surface tension. There are two ways for a torus to transform into one or more spherical droplets. The first way is to break via the Rayleigh-Plateau instability, as shown in Figs. 2.3(a-c) for two liquids with a high viscosity contrast. However, for toroidal droplets of aspect ratio $\xi = R_0/a_0 < 2$, breakup does not occur [2]; in this case, the handle of the torus progressively

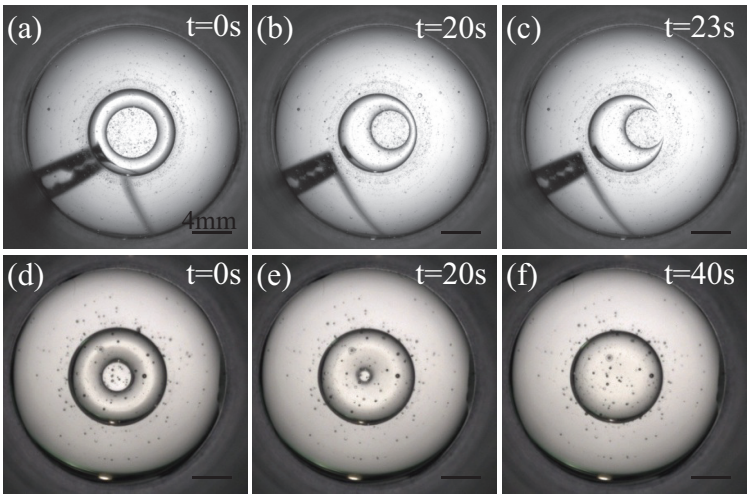

Figure 2.3: The evolution of a liquid torus in silicone oil with (a-c) $\xi \approx 3.4$ and (d-f) $\xi \approx 1.9$. The inner liquid constist of a solution of 16 mM SDS in water and the outer liquid is silicone oil with $30,000$ cSt viscosity.

shrinks until it disappears, resulting in a single spherical droplet [see Fig. 2.3(d-f)]. We refer to this process as shrinking. Note that shrinking is not observed only for $\xi < 2$, but for all ξ. This can be seen in Fig. 2.3(a,b) in the case of a breaking torus. By comparing the first two frames, it can be seen that the torus is shrinking in addition to breaking. We find that shrinking is always present in a toroidal geometry. The transition between shrinking while breaking to shrinking without breaking at $\xi \approx 2$ is reminiscent to the Rayleigh-Plateau criterion for the breakup of cylindrical jets[2], which states that a liquid cylinder is unstable to breaking as long as $L > 2\pi\alpha_0$, where L and α_0 are the length and radius of the cross section of the cylinder, respectively [15, 76]. Therefore, $\xi < 2$ corresponds to a Rayleigh-Plateau criterion for the breakup of toroidal droplets.

2.3.1 Sets of Toroidal Coordinates

Throughout the thesis there are two orthogonal toroidal coordinate systems we will use. The choice of which one to use depends on the type of problem. The first coordinate system is defined with respect to a given central circle radius, R_0, as:

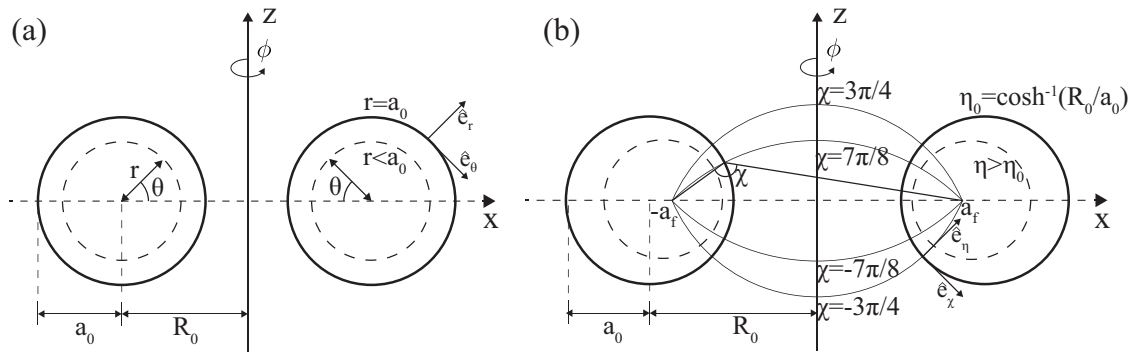

Figure 2.4: An illustration of the two toroidal coordinates (a) (r, θ, ϕ), and (b) (η, χ, ϕ), with their respective unit vectors $\hat{e}_r$, $\hat{e}_\theta$ and $\hat{e}_\eta$, $\hat{e}_\chi$. A torus is obtained by revolving around the z-axis.

$$x = (R_0 - r\ \cos(\theta))\ \cos(\phi) \tag{2.1}$$

$$y = (R_0 - r\ \cos(\theta))\ \sin(\phi) \tag{2.2}$$

$$z = r\ \sin(\theta) \tag{2.3}$$

where ϕ is the azimuthal angle, r the radial distance from the center of the cicular cross-section of the torus, and θ the polar angle that goes around the tube, as shown in Fig. 2.4(a). In this coordinate system, a toroidal surface is defined for a constant value of r. An important quantity of a vector space that depends on the chosen coordinate system is the metric tensor, which allows to locally measure distances along the different coordinates. Letting $(x_1, x_2, x_3) = (x, y, z)$ represent the Cartesian coordinates in $\mathbb{R}^3$, and (q_1, q_2, q_3) a general orthogonal coordinate system, the components of the 3x3 metric tensor, g_{ij}, are given by:

$$g_{ij} = \frac{\partial x_k}{\partial q_i}\frac{\partial x_k}{\partial q_j}, \tag{2.4}$$

where the indices follow the Einstein notation, which means that we are implicitly summing over the values of subscripts that occur twice in the expression. For $(q_1, q_2, q_3) = (r, \theta, \phi)$, this results in $g_{rr} = 1$, $g_{\theta\theta} = r^2$, and $g_{\phi\phi} = (R_0 - r\ \cos(\theta))^2$. The off-diagonal terms are all

zero, which is always true for an orthogonal coordinate system. Another important quantity we use is the unit vectors along the different coordinates. Given that $\vec{r} = (x, y, z)$, the unit vectors are calculated as $\hat{e}_i = \frac{d\vec{r}}{dq_i} / \left|\frac{d\vec{r}}{dq_i}\right|$. Explicitly, for $\hat{e}_r$, $\hat{e}_\theta$, and $\hat{e}_\phi$, we have:

$$\hat{e}_r = \frac{\frac{d\vec{r}}{dr}}{\left|\frac{d\vec{r}}{dr}\right|} = (-\cos(\theta)\ \cos(\phi),\ -\cos(\theta)\ \sin(\phi),\ \sin(\theta)), \tag{2.5}$$

$$\hat{e}_\theta = \frac{\frac{d\vec{r}}{d\theta}}{\left|\frac{d\vec{r}}{d\theta}\right|} = (\sin(\theta)\ \cos(\phi),\ \sin(\theta)\ \sin(\phi),\ \cos(\theta)), \tag{2.6}$$

$$\hat{e}_\phi = \frac{\frac{d\vec{r}}{d\phi}}{\left|\frac{d\vec{r}}{d\phi}\right|} = (-\sin(\phi),\ \cos(\phi),\ 0). \tag{2.7}$$

An illustration of the unit vectors $\hat{e}_r$ and $\hat{e}_\theta$ is shown in Fig. 2.4(a). It can be easily confirmed that the unit vectors are all orthogonal to each other, as expected for an orthogonal coordinate system.

The other coordinate system used is defined by rotating the two dimensional bipolar coordinate system, (η, χ), along the azimuthal angle ϕ. The bipolar coordinate system is defined with respect to two focal points located at $(x, z) = (\pm a_f, 0)$, where $a_f = \sqrt{R_0^2 - a_0^2} < R_0$. After rotating the bipolar rotating system around z, this toroidal coordinate system is given by:

$$x = \frac{a_f\ \sinh(\eta)\ \cos(\phi)}{\cosh(\eta) - \cos(\chi)} \tag{2.8}$$

$$y = \frac{a_f\ \sinh(\eta)\ \sin(\phi)}{\cosh(\eta) - \cos(\chi)} \tag{2.9}$$

$$z = \frac{a_f\ \sin(\chi)}{\cosh(\eta) - \cos(\chi)}. \tag{2.10}$$

The angle χ is defined as the angle between the two lines formed from a given point on (x, z) and the two focal points, and it takes values $\chi \in (-\pi, \pi]$. Note that for the toroidal coordinate system, we are dealing with a focal circle of radius a_f on the $z = 0$ plane, and not just two focal points, as in the bipolar coordinate system. A curve of constant χ in the

bipolar coordinate system defines a part of a circle that connects the two focal points, as shown in Fig. 2.4(b) for different values of χ, and in toroidal coordinates that translates to a spherical cap. The coordinate η defines the surface of a torus. If we define η_0 to be the surface that corresponds to our torus, then $\cosh(\eta_0) = \xi$. Hence, η is the variable that determines the inside or outside of our torus. For points inside our torus, the aspect ratio is higher, [see Fig. 2.4(b)] and therefore $\eta > \eta_0$. Similarly, points outside our toroidal surface correspond to $\eta < \eta_0$.

In this coordinate system the components of the metric tensor are:

$$g_{\eta\eta} = \left(\frac{a_f}{\cosh(\eta) - \cos(\chi)}\right)^2 \tag{2.11}$$

$$g_{\chi\chi} = \left(\frac{a_f}{\cosh(\eta) - \cos(\chi)}\right)^2 \tag{2.12}$$

$$g_{\phi\phi} = \left(\frac{a_f \ \sinh(\eta)}{\cosh(\eta) - \cos(\chi)}\right)^2, \tag{2.13}$$

with, as before, all diagonal terms being equal to zero. The unit vectors are:

$$\hat{\boldsymbol{e}}_{\boldsymbol{\eta}} = \left(\frac{(1 - \cosh(\eta)\ \cos(\chi))\cos(\phi)}{\cosh(\eta) - \cos(\chi)}, \frac{(1 - \cosh(\eta)\ \cos(\chi))\sin(\phi)}{\cosh(\eta) - \cos(\chi)}, -\frac{\sinh(\eta)\ \sin(\chi)}{\cosh(\eta) - \cos(\chi)}\right), \tag{2.14}$$

$$\hat{\boldsymbol{e}}_{\boldsymbol{\chi}} = \left(-\frac{\sinh(\eta)\ \sin(\chi)\cos(\phi)}{\cosh(\eta) - \cos(\chi)}, -\frac{\sinh(\eta)\ \sin(\chi)\sin(\phi)}{\cosh(\eta) - \cos(\chi)}, -\frac{(1 - \cosh(\eta)\ \cos(\chi))}{\cosh(\eta) - \cos(\chi)}\right), \tag{2.15}$$

$$\hat{\boldsymbol{e}}_{\boldsymbol{\phi}} = (-\sin(\phi),\ \cos(\phi),\ 0). \tag{2.16}$$

The unit vectors $\hat{\boldsymbol{e}}_{\boldsymbol{\eta}}$ and $\hat{\boldsymbol{e}}_{\boldsymbol{\chi}}$ are illustrated in 2.4(b). Observe that $\hat{\boldsymbol{e}}_{\boldsymbol{\eta}} = -\hat{\boldsymbol{e}}_{\boldsymbol{r}}$ and $\hat{\boldsymbol{e}}_{\boldsymbol{\chi}} = -\hat{\boldsymbol{e}}_{\boldsymbol{\theta}}$.

Finally, it is important throughout the thesis to be able to convert from one coordinate system to the other. Perhaps most importantly is to convert the angle χ to the angle θ, since θ is a lot easier to think about physically. The two are related by:

$$\theta(\eta, \chi) = \tan^{-1}\left(\frac{\sin(\chi)\sinh(\eta)}{1 - \cosh(\eta)\ \cos(\chi)}\right). \tag{2.17}$$

Note that for $\xi \to \infty$, $\eta \to \infty$, and $\tan(\theta) = -\tan(\chi)$, which implies that $\chi = \pi - \theta$.

Lastly, it is also important to invert the toroidal coordinates and obtain them in terms of the Cartesian coordinates:

$$\eta = \tanh^{-1}\left(\frac{2\, a_f\, \rho}{\rho^2 + z^2 + a_f^2}\right), \tag{2.18}$$

$$\chi = sgn(z)\ \cos^{-1}\left(\frac{z^2 + \rho^2}{\sqrt{z^4 + 2z^2(\rho^2 + a_f^2) + (\rho^2 - a_f^2)^2}}\right), \tag{2.19}$$

where $\rho^2 = x^2 + y^2$ and $sgn(z)$ is the sign function.

2.3.2 Calculation of the Laplace Pressure and Free Energy for Toroidal Droplets

We can understand the shrinking of a toroidal droplet by either considering the stresses on the torus or by considering its free energy. In order to calculate the stresses on the torus, we consider the normal stress balance at the interface given by the Young-Laplace equation:

$$p_{in} - p_{out} = 2\gamma H, \tag{2.20}$$

where p_{in} and p_{out} are the pressures at the interface for the inner and outer liquids, respectively, γ is the interfacial tension, and H is the mean curvature, which can be calculated as $2\ H\ =\ \boldsymbol{\nabla} \cdot \hat{\boldsymbol{n}}$, with $\hat{\boldsymbol{n}}$ the normal vector of our surface pointing outwards. Note that this convention to calculate H is used mainly in fluid dynamics, while in mathematics, one usually writes $2\ H = -\boldsymbol{\nabla} \cdot \hat{\boldsymbol{n}}$. In our case $\hat{\boldsymbol{n}} = \hat{\boldsymbol{e}}_{\boldsymbol{r}}$. For any orthogonal coordinate system (q_1, q_2, q_3) with $h_i = \sqrt{g_{ii}}$, the divergence of a vector function $\boldsymbol{F}(q_1, q_2, q_3)$ is defined as:

$$\boldsymbol{\nabla} \cdot \boldsymbol{F} = \frac{1}{h_1 h_2 h_3}\left(\frac{\partial\,(F_1 h_2 h_3)}{\partial q_1} + \frac{\partial\,(F_2 h_3 h_1)}{\partial q_2} + \frac{\partial\,(F_3 h_1 h_2)}{\partial q_3}\right). \tag{2.21}$$

By using the metric tensor [see Section 2.3.1], we find that for our torus $2H = \frac{\xi - 2\cos(\theta)}{a_0(\xi - \cos(\theta))}$. As a result:

$$p_{in}(\theta) - p_{out} = \frac{\gamma}{a_0}\frac{\xi - 2\ \cos(\theta)}{\xi - \cos(\theta)}. \tag{2.22}$$

Here, we assume that p_{out} is constant, since the hydrostatic pressure of the outer liquid sets this pressure. Finally, we compare the pressures at $\theta = \pi$ and $\theta = 0$ and find that:

$$p_{in}(\theta = \pi) - p_{in}(\theta = 0) = \frac{\gamma}{a_0}\frac{2\xi}{\xi^2 - 1} > 0, \tag{2.23}$$

which is always positive since $\xi > 1$. Hence, this pressure difference will induce a flow from $\theta = \pi$ towards $\theta = 0$, causing the torus to shrink.

From the thermodynamic perspective, we consider the grand potential, Ω, of a surface:

$$\Omega = \gamma A, \tag{2.24}$$

where A is the area. For a perfect torus $A = (2\pi a_0)(2\pi R_0) = 4\pi^2 R_0 a_0$. In our problem, the total volume, Vol $= (\pi a_0^2)(2\pi R_0) = 2\pi^2 R_0 a_0^2$, of the torus remains constant. Therefore, $d(\text{Vol}) = 0$ and $dR_0 = -2\xi da_0$, where the minus sign indicates that a_0 decreases with increasing R_0 at constant volume. We can then calculate the change in Ω using this condition and obtain:

$$d\Omega = \gamma dA = 2\pi^2 a_0 \gamma\ dR_0, \tag{2.25}$$

where we have assumed that γ is constant. Since $a_0 > 0$ and $\gamma > 0$, we see that Ω is minimized if R_0 decreases and, thus, if the torus shrinks.

2.4 Velocity field of a shrinking toroidal droplet

We perform Particle Image Velocimetry (PIV) to extract the flow field inside shrinking toroidal droplets. Existing theory assumed that as a toroidal droplet shrinks the tube of the torus expands uniformly keeping the cross section of the torus circular [3]. Using this

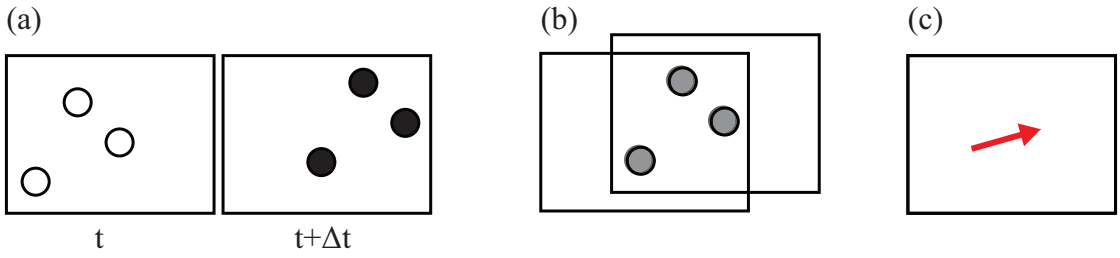

Figure 2.5: (a) Schematic showing optical inhomegeneities in an interrogation area for two consecutive frames. The optical inhomogeneities are spatially correlated (b) and (c) define a vector of the overall motion for the interrogation area.

hypothesis, the calculated shrinking speed of a toroidal droplet was in good agreement with experimental observations. In addition, the theory also provided the velocity field as the torus shrinks using the same hypothesis. More recently, the evolution of toroidal droplets has been numerically simulated. In this work, the instantaneous velocity field was calculated using the Oseen tensor that calculates the velocity field of a point force in Stokes flow [77]. This is equivalent to the Green's function for Stokes' equations. A force distribution based on Laplace's pressure for their interface was then used to find the velocity field everywhere, which was subsequently used to evolve the system in time [73]. The authors found that the torus shrinks, and that it did with a shrinking speed also in agreement with the experimental observations. However, in their case the cross section of the interface was not kept circular, and deformed significantly, especially close to the inside of the torus. Here we address experimentally this discrepancy between theory and experiments. In addition, we theoretically address the problem in the viscous regime, and compare with our experimental results to elucidate which of the many possible modes are needed to successfully account for our experimental observations.

2.4.1 Calibration Tests

PIV is a method of flow visualization that is based on monitoring the evolution of optical inhomegeneities [78]. In order to generate the optical inhomegeneities, the fluid is

seeded with tracer particles, which, if small enough, follow the velocity of the fluid. The fluid is then illuminated such that the light scattered from the particles creates the optical inhomogeneities. Unlike particle tracking, where individual particles are monitored over time, PIV spatially correlates these optical inhomegeneities between consecutive frames to assign nearly instantaneous local velocities. Specifically, each frame is split into smaller areas, called interrogation windows. By correlating these interrogation windows between consecutive frames, we can assign a displacement vector to each of them. We do this by finding the direction where the correlation is maximum [see Fig. 2.5]. This corresponds to motion of the fluid in the local area in the time between consecutive frames. Thus, this vector can then be translated to a velocity by using the time between frames. We can then assign a local velocity to each interrogation window and obtain th complete flow field in the field of view.

We use polystyrene beads, with an average diameter of $d_p = 16.2$ μm and a density of $\rho_p = 1.06$ g/mL, as tracer particles. As mentioned earlier, an important assumption in order to perform PIV is that the tracer particles follow the velocity of the surrounding flow. This assumption depends on the Stokes number, $Stk = \frac{t_o u_o}{l_o}$, where t_o is the relaxation time of a particle required for it to acquire the velocity of the surrounding fluid, and u_o and l_o are the characteristic velocity and length of the system, respectively. The Stokes number is the ratio of the time it takes for a particle to change its velocity and the characteristic time associated to the velocity field. In our case, $u_o \approx 0.01$ mm/s and $l_0 \approx 1$ mm corresponding to the shrinking velocity and the droplet size. In addition, the Reynolds number for the inner liquid is $Re \approx 10^{-2}$. Therefore, we are well within the Stokes regime and we can calculate t_o using the Stokes drag. The drag force acting on a spherical particle is $F_D = -3\pi\mu d_p \Delta U$, where ΔU is the difference between the particle speed and the speed of the surrounding fluid [79]. From Newton's second law, $F_D = m_p(\Delta\dot{U}) = \frac{1}{6}\pi d_p^3 \rho_d (\Delta\dot{U})$, with m_p the mass of the particle. Therefore, $(\Delta\dot{U}) = -\frac{\Delta U}{t_0}$, where $t_o = \rho_p d_p^2/(18\mu)$. Since we will be putting tracer particles in the inner liquid, $\mu = \mu_i \approx 1$ mPa·s, and we obtain that $Stk \approx 10^{-5} << 1$.

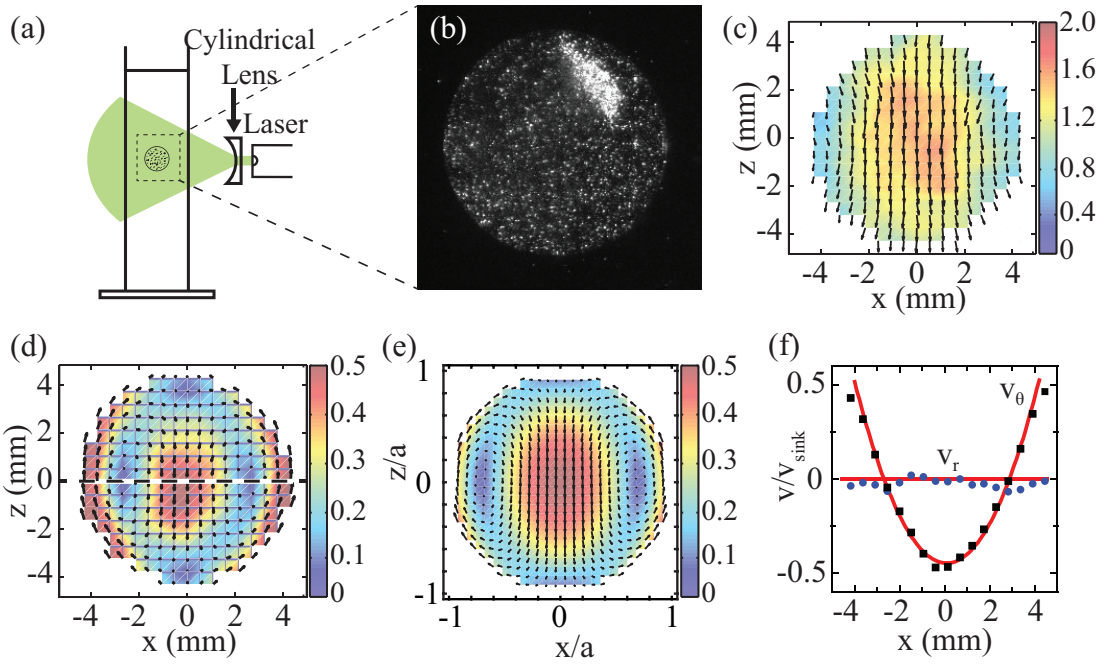

Figure 2.6: (a) Schematic of the experimental setup for a sinking spherical droplet. Not drawn to scale. (b) A water spherical droplet containing polystyrene particles sinking in 1,000 cSt silicone oil. A laser sheet illuminates the central cross section of the droplet. (c) The velocity field in the lab frame of one frame. (d) Averaged experimental flow field in the drop frame of reference. (e) The theoretical velocity field inside a sinking droplet. (c) Experimental v_r (●) and v_θ (■) along the dashed line highlighted in panel (b) together with the theoretical expectations. All color code corresponds to the speed normalized with the sinking speed, v_{sink}.

As a result, we are confident that the particles will follow the velocity field.

We first perform experiments with sedimenting spherical droplets to validate our PIV experiments and analysis. In the case of a sedimenting liquid sphere, the expected flow field is well known for any inner and outer liquid viscosities [79–82]. We note that we choose the radius of these droplets so that they match the typical tube radius of our toroidal droplets, which is on the order of $a_0 \approx 2-4$ mm. Since the liquid-liquid interface in our experiments is curved, light refraction could be significant, depending on the optical contrast between the liquids. Hence, these experiments also allow us to test whether these effects play a dominant role in our experiments with toroidal droplets. The outer liquid is a 1,000 cSt silicone oil, while the spherical droplets are made of deionized water containing the tracer

particles. Since the respective densities are $\rho_o \approx 0.97$ g/mL and $\rho_i \approx 0.99$ g/mL, the droplet sinks. We visualize the flow by illuminating the center of the droplet with a laser sheet, as shown in Fig. 2.6(a,b). An example of the flow field obtained from two consecutive frames is shown in Fig. 2.6(c). To acquire a better flow field, we average the field obtained in six consecutive frames. Since the frame rate used is 15 fps, this corresponds to averaging for ≈ 0.4 s. Using the sinking velocity of our experiment, we find that the droplet has moved about 1% of its diameter during this time and, therefore, the averaging process does not significantly alter the flow field. After performing PIV, we subtract the sinking velocity from the flow field and obtain the typical circulation profile in the reference frame of the drop, as shown in Fig. 2.6(d). The sinking speed, v_{sink}, was measured independently by measuring the distance travelled by the center of the droplet in 10 s. We use this velocity to normalize the flow fields reported. Theoretically, the velocity field, for the case where $\mu_i << \mu_o$, is given by [82]:

$$v_r = \frac{v_{sink}}{2} \cos\theta \left(1 - \frac{r^2}{a^2}\right) \tag{2.26a}$$

$$v_\theta = -\frac{v_{sink}}{2} \sin\theta \left(1 - \frac{2r^2}{a^2}\right) \tag{2.26b}$$

where r and θ are the usual two spherical coordinates, and v_r and v_θ are the velocities along the associated directions. We plot this result in Fig. 2.6(e). Note that the velocity has azimuthal symmetry. To quantitatively compare the experimental result and the theoretical expectations, we consider v_r and v_θ along the dashed line in Fig. 2.6(b). Both experiments and theory agree with each other, as shown in Fig. 2.6(f), confirming the robustness of our set-up, experimental procedures, and data analysis.

It is important to mention that there are potential effects on the sinking of spherical droplets due to the presence of surfactants in the liquids. In particular, surfactants are molecules that reside at the interface. Due to the circulation inside the droplet, we can potentially have a higher concentration of surfactant at the top of the droplet than at the

bottom of the droplet causing a tangential surface stress due to the Marangoni effects, which will oppose the circulation. As a results, such droplet can sink similarly to solid spheres [83]. However, given the fact that the velocity field from PIV scaled with the terminal velocity, which was measured independently, agrees with theoretical predictions, we believe that we are not in this situation. In addition, we looked at the shrinking of tori with different surfactant concentrations, and found there is no effect on the shrinking velocity that cannot be accounted with the surface tension [see Appendix B].

2.4.2 PIV of a Shrinking Torus

To perform PIV of a shrinking toroidal drop, we constructed a larger cuvette in order to suppress potential wall effects that could affect the evolution of the torus. Specifically, we constructed a parallelepiped cuvette with a square base of side 6 cm and a height of 5 cm.

In addition, we need to carefully choose the inner liquid. One idea was to index match the inner and outer liquids such that we will not have any effect of refraction in our experiments. The reported value for 60,000 cSt silicone oil (ClearCo) is $n_{S.O.} = 1.406$, while for water it is $n_w = 1.333$. We can make a solution of 53 w/w glycerol in water with a refractive index equal to $n_{S.O.}$. This mixture can be estimated to have a density of $\rho \approx 1.12$ g/mL. Since $\rho_{S.O.} \approx 0.97$, experiments using these liquids were greatly affected by sinking; the toroidal droplet in fact sinks faster than it shrinks, dramatically affecting the cross section of the torus, thus complicating the study of the shrinking instability.

Since from the sinking sphere experiments, we know that refraction does not play a significant role on the acquired flow field, we instead chose the inner liquid to be a solution containing 0.1 w/w poly-ethylene glycol (PEG) with a molecular weight of 8,000 g/mol in water, which also contain tracer particles at a volume of fraction of 0.001. For the outer liquid, we chose a 60,000 cSt silicone oil. In this case, $\rho_o \approx 0.97$ g/mL and $\rho_i \approx 0.99$ g/mL, which implies that sinking, albeit present, is not expected to have a large effect. In addition, the two liquids have different refractive indices: $n_i = 1.33$ and $n_o = 1.40$. To generate the

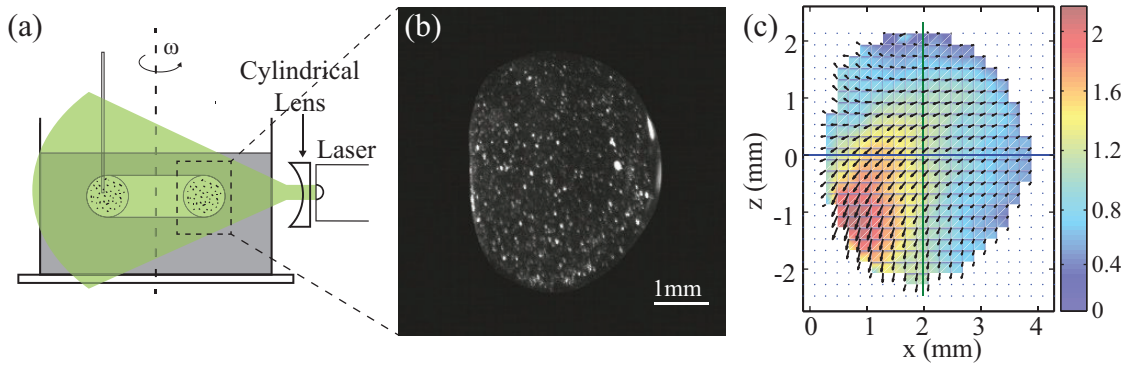

Figure 2.7: (a) Schematic of the experimental setup for the generation of toroidal droplets together with the PIV setup. Not drawn to scale. The cuvette is a parallelepiped with a square base of side 6 cm; the flat walls enable illuminating and imaging without refraction. Typical angular velocities are $\approx 2\pi$ rad/s. (b) Typical snapshot of a shrinking toroidal droplet with $R_0/a_0 \approx 1.2$. (c) Flow field obtained using PIV.

toroidal droplets, we use $\omega \sim 5-10$ rad/s, and a typical flow rate and injection volume that are 30−40 mL/hr and 0.35 mL, respectively. After the injection of the inner liquid, the tip is carefully removed and we terminate the rotation of the continuous phase. The PEG is used to lower the surface tension, and hence slow the subsequent dynamics to allow enough time for any flow field due to the generation process to dissipate. Specifically, we measured the surface tension using the pendant drop method [see Appendix A] to be $\gamma = 28 \pm 1$ mN/m, while without PEG it is $\gamma = 41 \pm 2$ mN/m. Since the typical time scale for the torus to shrink is given by the capillary time, $t_{cap} = \mu_o a_0/\gamma$, this decrease in γ increases the experimental time by about 30%. We note that increasing the time further would imply more significant sinking. Since the speed of sinking is not affected by γ, longer experiments will cause the torus to shrink more significantly, which is undesirable as we are interested in studying the shrinking of the torus.

As for a sinking spherical droplet, the flow inside a shrinking torus has azimuthal symmetry. It is thus enough to image the flow in a two-dimensional cross-section. We do this by using a laser sheet, as shown in Fig. 2.7(a).

A typical snapshot of a toroidal droplet during the shrinking process is shown in Fig. 2.7(b); this droplet had an aspect ratio of $R_0/a_0 \approx 1.2$, which is below the threshold where

Rayleigh-Plateau modes can develop and cause break-up. Hence, these droplets can only evolve via shrinking. From the image we realize that the cross section of the torus is not circular. Instead, we observe that the initial circular cross section elongates vertically and is slightly flatter near the inside of the torus. This is qualitatively similar to what was seen in computer simulations [73]. We then use PIV to determine the flow field inside the torus. The result associated to the image shown in Fig. 2.7(b) is presented in Fig. 2.7(c). Note that the color scale corresponds to the measured velocity divided by the shrinking speed, v_{sh}. We obtain the shrinking velocity by averaging the x-component of the velocity through the whole cross section of the torus. The lack of up-down symmetry in the velocity field indicates that the observed flow field is not purely due to shrinking; it also includes contributions from the sinking of the toroidal droplet due to the small density mismatch of the inner and outer liquids.

2.4.3 Velocity Field Decomposition

To isolate the flow associated to shrinking, we recall that the Reynolds number in our experiments is $Re \sim O\left(10^{-6}\right)$ for the outer liquid and $Re \sim O\left(10^{-2}\right)$ for the inner liquid, implying we are within the Stokes regime, where:

$$\mu \Delta \mathbf{u} = \nabla p, \tag{2.27}$$

with $\mathbf{u}$ the velocity and p the pressure. Since the governing equations in our problem are linear, we can use the superposition principle and think of the flow in Fig. 2.7(c) as the sum of the flow associated to sinking and the flow associated to shrinking. Interestingly, these flows have different up-down symmetries. Consider sinking first. In this case, v_x is antisymmetric under a $z \rightarrow -z$ operation [$v_x(z) = -v_x(-z)$], while v_z is symmetric under a $z \rightarrow -z$ operation [$v_z(z) = v_z(-z)$], as clearly seen in the schematic in 2.8(a), where, for the sake of simplicity, we illustrate the situation for a thin toroidal droplet; the up-down sym-

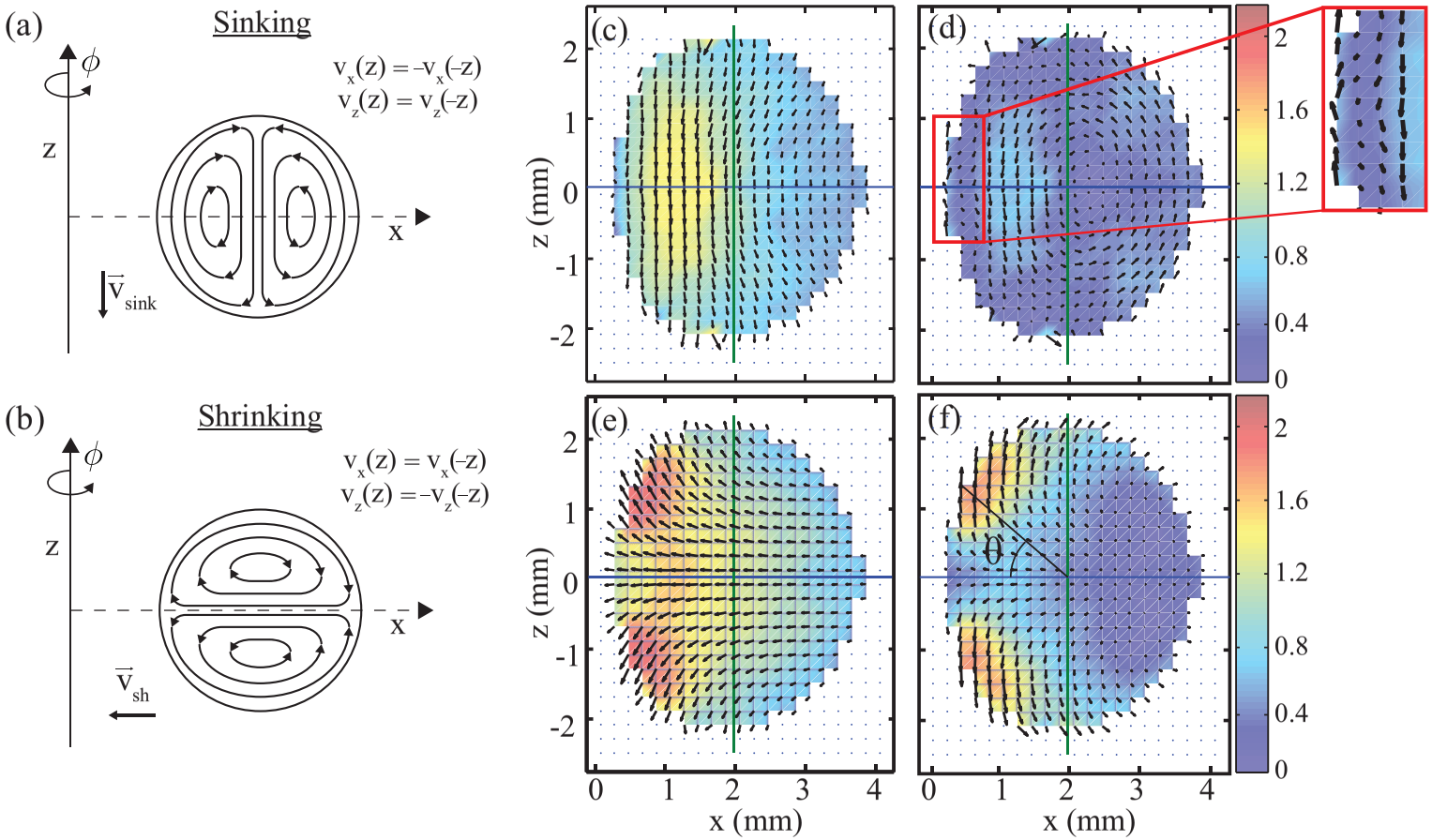

Figure 2.8: Schematic illustrating the flow field in the drop frame inside a very thin toroidal droplet that either (a) sinks or (b) shrinks. The up-down symmetries of the flow are highlighted on the top right of each panel. (c,e) Flow field associated to sinking and shrinking in the lab frame and (d,f) in the drop frame, respectively. The color scale correspond to the measured velocity normalized with v_{sink} in (c,d), and v_{sh} in (e,f).

metry reflected here, however, is general and maintained irrespective of the aspect ratio. For a shrinking torus, however, $v_x(z) = v_x(-z)$ and $v_z(z) = -v_z(-z)$, as clearly seen in the schematic in 2.8(b), where again we illustrate the situation for a thin toroidal droplet. We then obtain the symmetric and antisymmetric components of each of the velocity components, $v_i^S = [v_i(z) + v_i(-z)]/2$ and $v_i^A = [v_i(z) - v_i(-z)]/2$, with $i = x, z$.

Hence, by taking the antisymmetric part of v_x and the symmetric part of v_z, we isolate the sinking velocity field. The result is shown in Fig. 2.8(c). By subtracting v_{sink}, we obtain the velocity field in the frame of reference of the droplet as shown in Fig. 2.8(d). Note that the flow now has the expected up-down symmetry for sinking. Interestingly, we observe the expected double circulation with the circulation near $\theta = 0$ heavily suppressed. This is reasonable, since as the aspect ratio decreases, the radius of the handle at $\theta = 0$ becomes smaller. The flow through the handle will be impeded and the fluid moves faster around the torus than through the torus.

Similarly, we can calculate the shrinking part of the velocity field using the symmetric part of v_x and the antisymmetric part of v_z. The result is shown in Fig. 2.8(e). We observe that the velocity is higher near the inside of the torus, reflective of the shrinking process. By subtracting v_{sh} we obtain the flow field in the drop frame, as shown in Fig. 2.8(f). It is now evident that the velocity is not radial at the interface, but that instead there are both radial and tangential components of the velocity. Since, we are working in the Stokes regime where viscous stresses dominate and the only tangential stresses acting on the interface are viscous stresses, the tangential component of the velocity is probably mainly due to viscosity effects. The tangential velocity in turn causes circulation inside the droplet. Hence, the viscous stresses are responsible for the circulation seen inside the droplet. In this frame of reference, we also see that there is a source near the outer part of the torus. This results from volume conservation; as the torus shrinks, the tube radius must increase.

To test the flow decomposition we are using to isolate the shrinking components, we perform computer simulations. We use the level-set method for two-phase flows in COM-

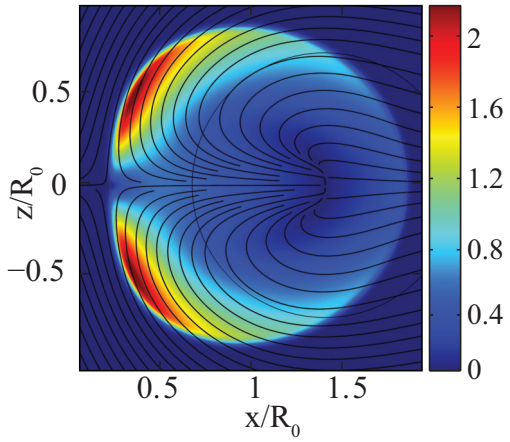

Figure 2.9: Computational flow fields in the reference frame of the cross section for a torus with $\xi \approx 1.2$. The color bars have been scaled with v_{sh}.

SOL Multiphysics [84] and simulate the experimental situation in the absence of gravity. We find that the overall drop deformation and flow field agrees well with our experimental findings, as shown in Fig. 2.9. This confirms the procedure to isolate the shrinking flow from the experimental flow field.

2.4.4 Streamfunction in Toroidal Coordinates

To theoretically describe the experimental velocity field, we use the stream function for Stokes flow. In Appendix C, we show the general form of the differential equation describing the stream function in the Stokes regime for a two-dimensional flow where one of the components of the velocity is zero. Specifically, a two-dimensional flow means that the velocity depends only on two coordinates and the zero velocity component is along the third coordinate. For a coordinate system (q_1, q_2, q_3), this is written as:

$$\vec{u} = u_1(q_1, q_2)\hat{\boldsymbol{e}}_{\mathbf{1}} + u_2(q_1, q_2)\hat{\boldsymbol{e}}_{\mathbf{2}}. \tag{2.28}$$

In our case the velocity is independent of ϕ, and there is no component of the velocity along $\hat{e}_\phi$ due to the azimuthal symmetry of the shrinking problem. An additional condition for using the stream function is that the metric tensor, g_{ij}, is independent of ϕ, which is true for

the two toroidal coordinate systems. As a result, we can use the general form of the stream function, as detailed in Appendix C. Using the (η, χ) coordinate system, the stream function satisfies $E^2E^2\Psi = 0$, where E^2 is a second order operator defined as [see Eq. C.18]:

$$E^2 = \frac{\sinh(\eta)(\cosh(\eta) - \cos(\chi))}{a_f} \left(\frac{\partial}{\partial \eta} \left(\frac{(\cosh(\eta) - \cos(\chi))}{a_f \sinh(\eta)} \frac{\partial}{\partial \eta} \right) + \frac{\partial}{\partial \chi} \left(\frac{(\cosh(\eta) - \cos(\chi))}{a_f \sinh(\eta)} \frac{\partial}{\partial \chi} \right) \right). \tag{2.29}$$

This partial differential equation has been solved analytically, and the solution takes the form of an infinite series [85]:

$$\Psi = \frac{a_f \sinh(\eta)}{(s - \cos(\chi))^{3/2}} \sum_{n=0}^{\infty} \{\sin(n\chi), \cos(n\chi)\} \left\{ P^1_{n-3/2}(s), P^1_{n+1/2}(s), Q^1_{n-3/2}(s), Q^1_{n+1/2}(s) \right\}, \tag{2.30}$$

where P^m_l, and Q^m_l are the associated Legendre polynomials of the first and second kind of order (l, m), respectively, and $s = \cosh(\eta)$. We note that the Legendre polynomials that have a half-integer order l are also known as toroidal functions. In the above expression, the curly brackets refer to a linear superposition of the terms inside the brackets. The stream function for $\cos(n\chi)$ corresponds to flow fields that purely sink, while for $\sin(n\chi)$ it corresponds to flow fields that purely shrink. In addition, the identities $P_{n+1/2} = P_{-n-3/2}$ and $Q_{n+1/2} = Q_{-n-3/2}$ hold, and hence, we can extend the sum to $n \in (-\infty, \infty)$ and eliminate the $P_{n+1/2}$ and $Q_{n+1/2}$ terms. Finally, the inside of the torus corresponds to $\eta \in [\eta_0, \infty)$, where $\eta_0 = \cosh^{-1}(R_0/a_0)$ [see Section 2.3.1]. Since, $P^1_{n-3/2} \to \infty$ as $\eta \to \infty$, we must take the coefficients of the $P^1_{n-3/2}$ terms to be identically equal to zero. As a result, the form of the stream function inside a torus for a purely shrinking flow field is:

$$\Psi = \frac{a_f \sinh(\eta)}{(\cosh(\eta) - \cos(\chi))^{3/2}} \sum_{n=-\infty}^{\infty} C_n \sin(n\chi) Q^1_{n-3/2}(\cosh(\eta)). \tag{2.31}$$

From Ψ, we can calculate the velocities along $\hat{e}_\eta$ and $\hat{e}_\chi$ by using equations C.10 and

C.11 [see Appendix C]. We obtain:

$$v_\eta = \frac{(\cosh(\eta) - \cos(\chi))^2}{a_f \ \sinh(\eta)} \frac{\partial \Psi}{\partial \chi}, \tag{2.32a}$$

$$v_\chi = -\frac{(\cosh(\eta) - \cos(\chi))^2}{a_f \ \sinh(\eta)} \frac{\partial \Psi}{\partial \eta}. \tag{2.32b}$$

We note we have re-derived these equations, since there are discrepancies in the literature with respect to the prefactor of the derivatives [3, 85–88].

To plot the flow fields associated to these velocities, we need to convert them from the toroidal coordinate system to the Cartesian coordinate system using the corresponding expression for $\hat{e}_\eta$ and $\hat{e}_\chi$ [see Eq. 2.14,2.15]. We calculate the half integer P_l^m and Q_l^m using the following relations [89, 90]:

$$P^m_{n-1/2} = \frac{(-1)^m \Gamma\left(n + \frac{1}{2}\right)}{\Gamma\left(n - m + \frac{1}{2}\right)} \int_0^\pi \frac{\cos(m\ \phi)\ d\phi}{(\cosh(\eta) + \sinh(\eta)\ \cos(\phi))^{n+1/2}}, \tag{2.33}$$

$$Q^m_{n-1/2} = \frac{(-1)^m \Gamma\left(n + \frac{1}{2}\right)}{\Gamma\left(n - m + \frac{1}{2}\right)} \int_0^\infty \frac{\cosh(m\ t)\ d\ t}{(\cosh(\eta) + \sinh(\eta)\ \cosh(t))^{n+1/2}}, \tag{2.34}$$

which we can numerically integrate. Note that the definition of $Q^m_{n-1/2}$ in equation 2.34 is divided by a π compared with the original paper on toroidal functions [89]. As a result any theorems used in [89] need to be checked and properly rescaled. However, in our case this is of no importance, since we will absorb this factor in the constants C_n. Finally, the derivatives in equations 2.32a and 2.32b are calculated using the finite difference method with $\Delta\eta = \Delta\chi = 0.0005$ [91].

The final code first creates a (x, z) grid. Then at each point it calculates η and χ using equations 2.18 and 2.19. Using these values we then calculate Ψ using equation 2.30. From there, we use the finite difference method to calculate v_η and v_χ, and convert these velocities to v_x and v_z using equations 2.14 and 2.15.

We first plot the vector fields of the various modes in the case of $\xi = 10$, since such

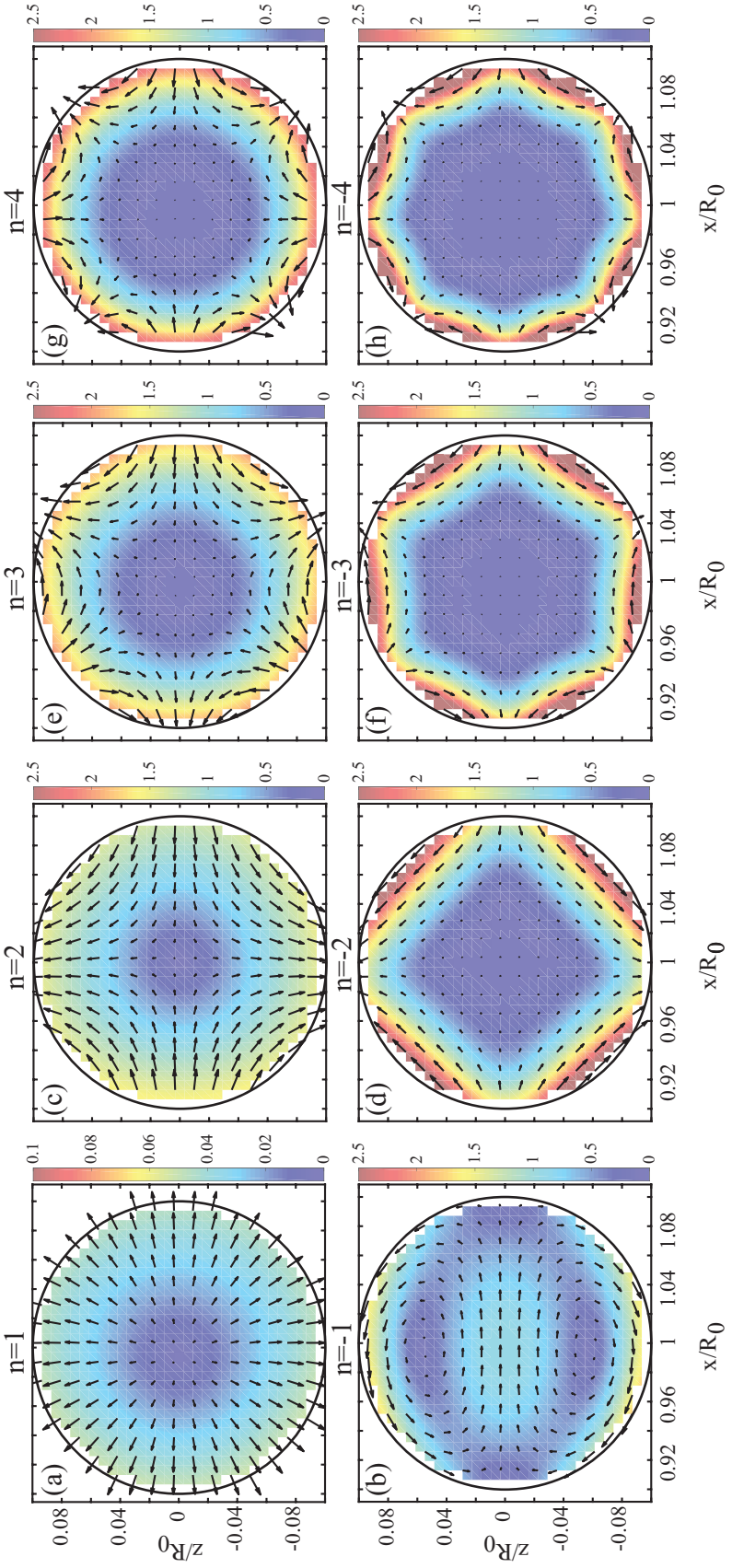

Figure 2.10: The flow field for a torus with $\xi = 10$, for the modes (a) $n = 1$, (b) $n = -1$, (c) $n = 2$, (d) $n = -2$, (e) $n = 3$, (f) $n = -3$, (g) $n = 4$, and (h) $n = -4$. Each mode has been normalized with each average velocity magnitude, $\langle|\vec{v}|\rangle$.

a thin torus can be locally viewed almost as a cylinder. For further intuition, we subtract the shrinking velocity of each mode, which is calculated as $v_{sh,mode} = \langle v_{x,mode} \rangle$. However, in this case we are not scaling each mode with its corresponding $v_{sh,mode}$ since $v_{sh,mode}$ can be very small in the thin torus limit. Instead, we normalize the speeds using $\langle |\vec{v}| \rangle$. In the frame of reference of the circular cross section, we find that the $n = 1$ captures the increase in a_0 due to volume conservation, while the $n = -1$ mode describes the circulation inside the torus [see Fig. 2.10(a,b)]. Note that for $n = 1$, the velocity is radial at the boundary, while for $n = -1$ it is tangential. For $n = \pm 2$, we find that there is flow from $\theta = 0, \pi$ towards $\theta = \pi/2, 3\pi/2$, which will deform the shape along the vertical [see Fig. 2.10(c,d)]. The direction of the velocity field is very similar for both of these modes, but the magnitudes are different. For the $n = -2$ mode, the magnitude of the velocity changes more dramatically as you go around the torus, while for the $n = 2$ mode, the magnitude remains almost the same. In addition, the magnitude of the velocity decreases much more rapidly from the interface to the center of the torus for the $n = -2$ mode compared to the $n = 2$ mode. Finally, as we increase the number of modes, we find that number of times the velocity normal to the interface changes direction increases with n as shown in Fig. 2.10(e-h) for $n = \pm 3$ and $n = \pm 4$. This reflects the fact that the stream function depends on $\sin(n\chi)$ [see Eq. 2.31]. However, the differences between the $n = 3$ and $n = -3$ modes, and the $n = 4$ and $n = -4$ modes are similar to the $n = \pm 2$ modes, where the magnitude of the velocity decreases more rapidly from the interface to the center of the torus for the $n = -3$ and $n = -4$ modes compare to the $n = 3$ and $n = 4$ modes.

We now consider the case of $\xi = 1.6$, which is close to the experimental situation described before. For $n = 1$ the flow field still causes a_0 to increase, but this is more important in the region around $\theta = 0$, as shown in Fig. 2.11(a). In addition, the circulation for $n = -1$ has also moved closer to $\theta = 0$ [see Fig. 2.11(b)]. The later is understandable, since the outer fluid in the "hole" of the torus must be displaced as the torus shrinks. For thick tori, there is not a lot of space within the "hole" and the only possibility of to displace

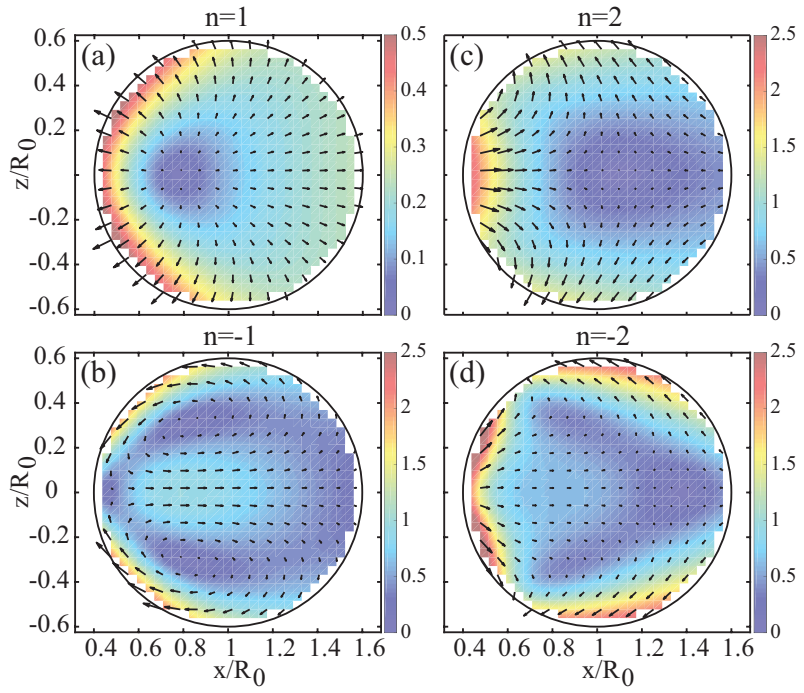

Figure 2.11: The flow field for a torus with $\xi = 1.6$, for the modes (a) $n = 1$, (b) $n = -1$, (c) $n = 2$, and (d) $n = -2$. Each mode has been normalized with each average velocity magnitude, $\langle|\vec{v}|\rangle$.

it along the $\pm z$ direction, which will cause an extra circulation in this region of the torus due to the no-slip boundary condition. For $n = \pm 2$, the corresponding modes cause the interface to deform at angles $\theta < \pi/2$. These modes would produce the vertical elongation of the torus seen experimentally.

2.4.5 Shrinking Tori - Comparing Theory and Experiment

To compare our experimental results with the theory, we need to find the constants, C_n, associated to the modes in equation 2.31. We obtain these constants by determining the experimental velocity at the interface and obtaining the radial, v_r, and tangential, v_t, components as a function of the polar angle θ. To do this, we define the center of the tube of the torus as the centroid of the cross section. From there, we find the distance, d, to the interface for every θ, and assign the velocity to be the average of all the points within 5% of d from the interface. Finally, we assign v_r to be the component radially out from the

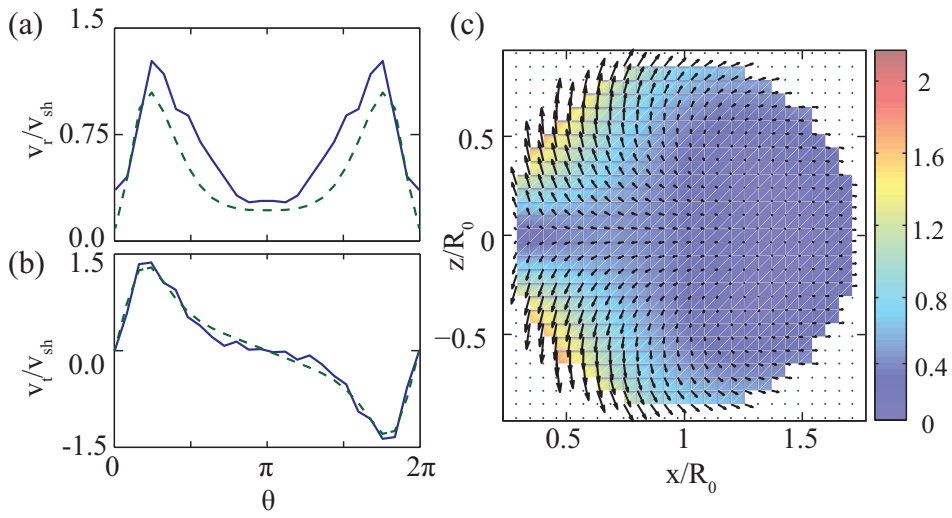

Figure 2.12: (a) Radial, v_r, and (b) tangential, v_t, velocities at the surface of the torus versus the polar angle θ. Solid lines correspond to experiments while dashed lines are theoretical fits. Note $\vec{v_r} = -v_r\hat{e_\eta}$ and $\vec{v_t} = -v_t\hat{e_\chi}$. (c) Flow field calculated from the stream function using the experimental boundary velocities. All velocities are scaled with v_{sh}.

centroid, and v_t as $|\vec{v} - v_r\hat{\boldsymbol{e}}_{\boldsymbol{r}}|$.

We find that v_r is not constant, but that instead, it peaks at $\theta \approx 50^o$ and $\theta \approx -50^o$, as shown by the blue line in Fig. 2.12(a), and consistent with the polar angle in the inside region of the torus below which the cross section of the toroidal droplet is most deformed from the circular shape [see Fig. 2.8(f)]. Similarly, v_t also has extrema at approximately the same angles, as shown by the blue line in Fig. 2.12(b). Also note that v_r is an even function about $\theta = \pi$, while v_t is an odd function about $\theta = \pi$. This reflects the symmetries of the flow field in the shrinking problem.

We then fit the theoretical velocity to the experimental velocity at the interface and obtain the constants C_n. We find that by only considering the $n = -2, -1, 1, 2$ modes, we are able to capture all experimental features. We perform a single simultaneous fit for both v_r and v_t while constraining the value of the constants C_n by forcing the resultant velocity field to have the same shrinking speed as in the experiment. We are able to accurately reproduce the experimental velocities, as shown with the dashed lines in Figs. 2.12(a,b).

We obtain $C_{-2} = (0.2 \pm 0.1)v_{sh}$, $C_{-1} = (0.50 \pm 0.06)v_{sh}$, $C_1 = (-1.33 \pm 0.06)v_{sh}$ and

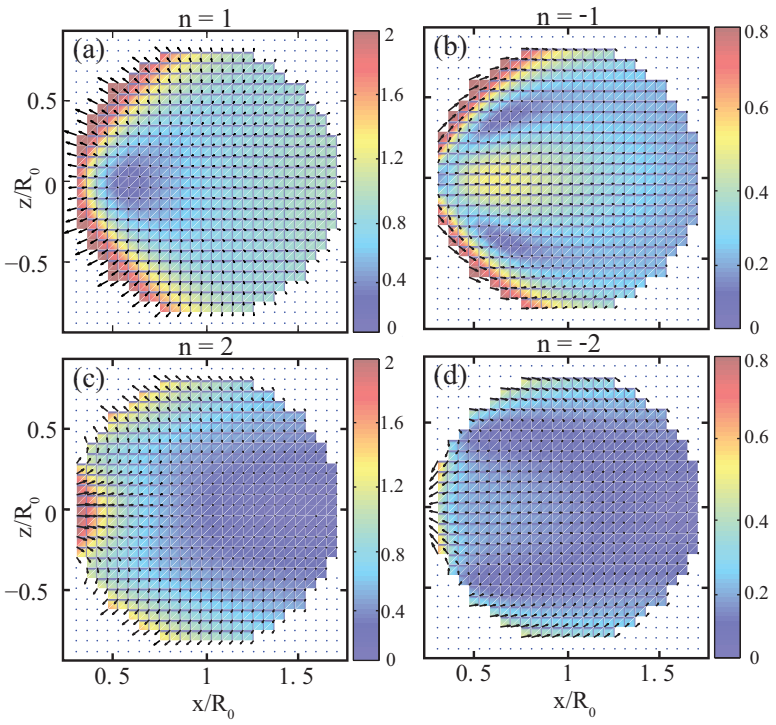

Figure 2.13: (a) $n = 1$, (b) $n = -1$, (c) $n = 2$ and (d) $n = -2$. The color code corresponds to the measured speeds normalized with v_{sh}.

$C_2 = (-0.4 \pm 0.1)v_{sh}$. Using these constants, we obtain the flow field inside the toroidal droplet. The result, shown in Fig. 2.12(c) in the drop frame, captures all relevant features seen in the experiments [see Fig. 2.8(e)], including the circulation due to viscous stresses, the higher velocities in the inner region of the torus compared to those in the outer region of the torus, and the presence of a source in the flow field near the outer part of the torus. We now consider each mode separately; these are shown in Figs. 2.13 in the drop frame. The $n = 1$ mode is radial at the interface, as shown in Fig. 2.13(a), and has the largest weight of all four modes. This was the only mode considered in Ref. [3] and is responsible for the increase in the tube radius as the torus shrinks. Note that in the presence of this mode only, the cross-section of the torus would remain approximately circular throughout the shrinking process and the velocity would be only radial at the interface. In contrast, the $n = -1$ mode is tangential at the interface, as shown in Fig. 2.13(b), and is responsible for the circulation seen experimentally. Finally, the $n = \pm 2$ modes can account for the

shape deformation we observe. The $n = 2$ mode produces a flow field that slows down the interface in the inside region of the torus, at $\theta \approx 0^o$, as shown in Fig. 2.13(c), hence promoting the experimental flattening in this region. The $n = -2$ mode, shown in Fig. 2.13(d), is very similar to the n = 2 mode, but with inverted velocities. Note the difference in the absolute values in the velocities, though, reflecting that the $n = 2$ mode dominates over the $n = -2$. Note also that the flow fields for each mode are all consistent with the expected up-down symmetries.

2.4.6 Sinking Tori - Comparing Theory and Experiment

For completeness, we also consider the sinking problem. For a sinking torus, the stream function is:

$$\Psi = \frac{a_f \ \sinh(\eta)}{(\cosh(\eta) - \cos(\chi))^{3/2}} \sum_{n=-\infty}^{\infty} D_n \cos(n\chi) Q^1_{n-3/2}(\cosh(\eta)). \tag{2.35}$$

As before, let us consider the case of $\xi = 10$ first. In this case, the $n = 1$ mode shows the full circulation of the torus, as shown in Fig. 2.14(a). This is a flow field expected in the case of a toroidal vortex, but not for a sinking torus. In contrast, for $n = -1$, the flow field is very similar to the one expected for a thin torus, which is also similar to the flow field obtained in the case of a sinking spherical droplet; this is shown in Fig. 2.14(b). In the case of $n = \pm 2$, it is similar to the shrinking case, but with an expected deformation of the surface along the diagonal and not along the horizontal [see Fig. 2.14(c,d)]. By decreasing ξ to 1.6, we find that the $n = 1$ mode does not change significantly. The velocity still varies as we go around θ, almost as it did for $\xi = 10$ [see Fig. 2.14(e)]. However, for $n = -1$ the changes are more significant. In this case, the circulation close to $\theta = 0$ has been pushed to the inside of the torus [see Fig. 2.14(f)]. Finally, for $n = \pm 2$ the deformation angle is also moved closer to $\theta = 0$. This is similar to the change of the $n = \pm 2$ modes in the case of shrinking.

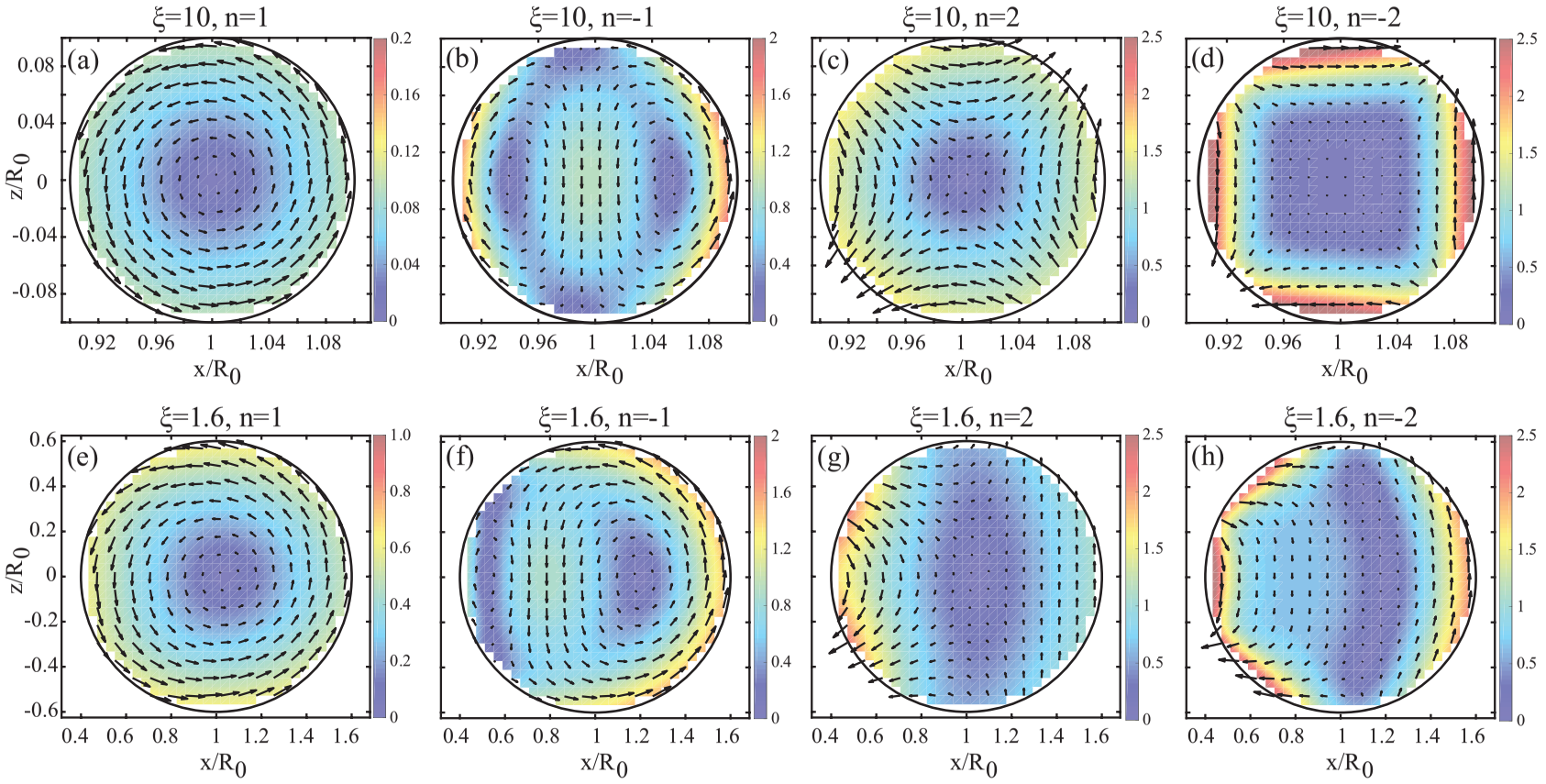

Figure 2.14: We compare the $n = \pm 1$ and $n = \pm 2$ modes for tori with aspect ratio of (a,b) $\xi = 10$ and (c,d) $\xi = 1.6$. All color codes for the flow fields are scaled with $\langle|\vec{v}|\rangle$.

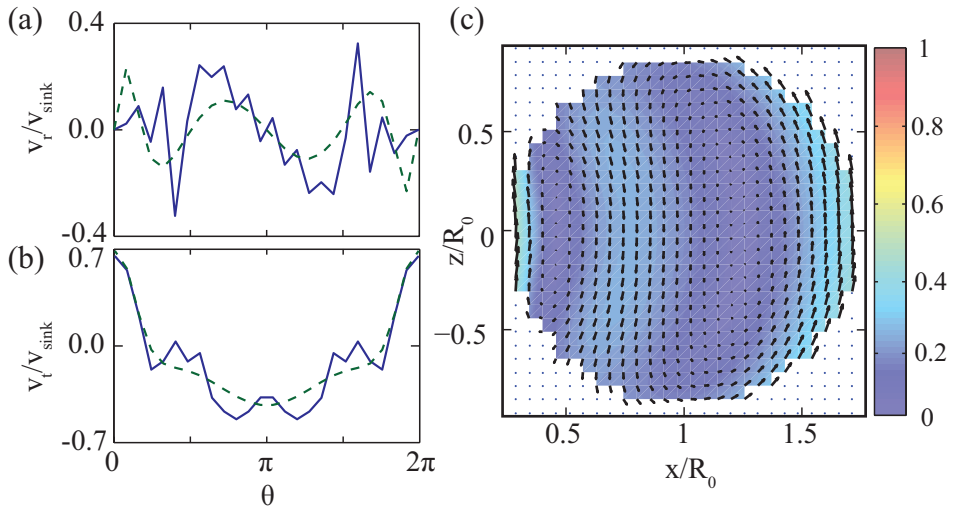

Figure 2.15: (a) Radial, v_r, and (b) tangential, v_t, velocities at the surface of the torus versus the polar angle θ corresponding to the sinking flow field of the torus. Solid lines correspond to experiments while dashed lines are theoretical fits. (c) Flow field calculated from the stream function using the experimental boundary velocities. All velocities are scaled with v_{sink}.

As with the experimental results for a shrinking torus, we can measure v_r and v_t experimentally, as seen in Figs. 2.15(a,b) for a sinking torus. First we observe that the obtained velocities are noisier than what we obtained in the case of a shrinking torus. Due to the small density difference, sinking is small and its magnitude in the reference frame of the droplet is also small. As a result, the noise in the data is more significant. Regardless of the noisy velocity at the interface, we find that v_r and v_t are odd and even functions about $\theta = \pi$, respectively, in contrast to the symmetries for the shrinking flow field, and consistent with the symmetries expected for a sinking flow field.

Using these results, we perform a simultaneously fit of the data considering the $n = 0, \pm 1, \pm 2$ modes. However, we do not enforce the total velocity to be the same as v_{sink}. This is because the polystyrene beads are not density-matched with the inner liquid, and therefore they will likely exhibit an additional contribution to the sinking flow field due to sedimentation. Note that in this case, we must consider the $n = 0$ mode, even though this mode does not contribute to the shrinking problem, since $\sin(n\chi) = 0$ for $n = 0$.

We find that $D_0 = (-1.0 \pm 0.1)v_{sink}$, $D_1 = (-0.26 \pm 0.06)v_{sink}$, $D_{-1} = (-0.6 \pm 0.1)v_{sink}$,

$D_2 = (-0.4 \pm 0.1)v_{sink}$, and $D_{-2} = (0.2 \pm 0.1)v_{sink}$. We see that despite the noise in the data, the fits are reasonable, especially in the case of v_t [see Fig. 2.15(a,b)]. From these coefficients, we reconstruct the flow field everywhere inside the torus, as shown in Fig. 2.15(c). The reconstructed flow field is similar to the one obtained in experiments [see Fig. 2.8(d)]; it shows the larger circulation near $\theta = \pi$. However, the magnitude of the velocities is very different. The theoretical velocities are a factor of two smaller than the ones observed experimentally. This reflects the lack of accuracy in the experimental sinking data due to slow sinking dynamics.

2.5 Conclusions

We have experimentally obtained the flow field inside shrinking toroidal droplets using PIV and exploited the linearity and symmetry properties of the flow in the problem. We observed that the cross section of the torus does not remain circular over time, but that it rather flattens in the inside region of the torus. Furthermore, the velocity at the interface has both radial and tangential components. We account for these facts theoretically and solve the Stokes equations using the stream function in toroidal coordinates (η, χ). Four modes are sufficient to account for all experimental features. Of all modes, the $n = 1$ mode is the most significant one and accounts for the flow field due to the expansion of the tube of the torus. The additional modes are needed to account for the observed circulation and deformation of the toroidal drop during shrinking.

CHAPTER 3
INSTABILITIES OF CHARGED TOROIDAL DROPLETS

3.1 Introduction

Charge affects the dynamics of drops and jets. Zeleny [92], and later Taylor [13], studied the deformation of the interface of charged liquids. These experiments consisted of a nozzle with a small amount of liquid that formed a droplet. A voltage difference was then applied across the liquid and a grounded plate located a small distance away from the nozzle. This resulted in an electric field in the region of the droplet. In this situtation, the liquid polarizes, causing the accumulation of charge at the interface, which further resulted in an additiontal stress at the interface. To balance this electric stress and the capillary stress, the interface deforms and adopts the shape of a cone pointing along the electric field towards the grounded plate; this occurs when the electric stresses are large enough. At this point, a jet emerges from the apex of the cone, which subsequently breaks into spherical droplets via the Rayleigh-Plateau instability. Interestingly, this phenomenon is exploited in electrospray technology [17, 93]. Note however, that the Rayleigh-Plateau instability for charged jets differs from its neutral counterpart.

Stability analysis for the Rayleigh-Plateau instability shows that a cylindrical jet is unstable for a range of wavelengths. The one that is seen experimentally is the wavelength that grows the fastest; the associated mode is referred to as the fastest unstable mode. When charge is added to the system, the wavelength of the fastest unstable mode progressively decreases with increasing charge [25, 26, 31, 94, 95].

New phenomenology can also result from charging jets. The occurrence of whipping modes, which are unstable non-axisymmetric modes driving the jet off-axis, is perhaps the most remarkable example [96]; these modes are exploited in applications like electro-

spinning [97–99]. Notably, both in electrospray and electrospinning the charged jet is not equipotential; the dynamics are so fast that the charges are unable to relax towards the interface, preventing a precise control over the surface charge density on the jet. Achieving this, however, is of interest. Consider adding charge on a toroidal droplet. As with the mean curvature, H, which varies around the tube of the torus, the surface charge density, σ_q, on the torus will be non-uniform as well. This can be seen by considering the fact that near the handle of the torus in one of the two circular cross sections the electric field produced by the opposite circular cross section, will be more appreciable at $\theta = 0$ than at $\theta = \pi$, due to proximity effects. This uneven charge distribution competes with the uneven H and will result in interesting phenomenology.

Here, we address how charge affects the evolution of toroidal droplets. We find that due to the unique geometry of the torus, shrinking reverts to expansion for sufficiently high voltages. We develop a simple model based on a stress balance to understand this new phenomenon. In addition, our charged toroidal droplets are electrostatically equilibrated, since the evolution of the torus takes about tens of seconds, which is much larger than the time needed for the charge to relax to the interface. In addition, given that in the thin torus limit, toroidal droplets break via the Rayleigh-Plateau instability, we study the effect of charge on the breakup of equipotential cylindrical jets. We use our experiments to test theories developed for equipotential jets.

3.2 Charge Distribution on a Liquid Torus

3.2.1 Experimental Capacitance of the Apparatus and Liquid Spheres

Our experiments involve charging a liquid toroidal droplet in a cuvette of silicone oil. To calibrate our experiments, we first charge the needle inside the silicone oil bath without the presence of a droplet. The silicone oil used has a viscosity of $30,000$ cSt, as this is the one for most experiments with toroidal droplets. This allows measuring the capacitance of the apparatus itself, which will then be used to correct the capacitance measured in the

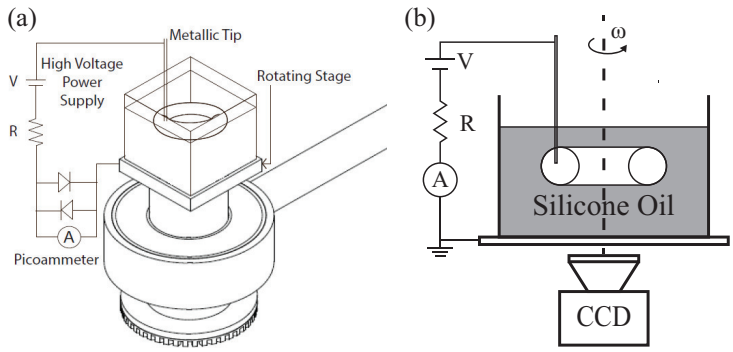

Figure 3.1: (a) SolidEdge model and (b) schematic of the apparatus used to generate charged toroidal droplets. The cuvette used in the experiments has a diameter of 2.5 cm, and the needle is made out of stainless steel. The silicone oil used is an insulator with conductivity of 10^{-12} S/m.

presence of droplets.

A schematic of the setup is shown in Fig. 3.1; it includes a high voltage power supply and a voltmeter. To measure the current, we use a picoammeter (Keithley 6485) with a pair of diodes to protect it from large voltage drops, as the picoammeter can only operate at voltages below 550 V; those diodes are located with opposite polarity. In the forward direction, a voltage of $V_F = 0.7$ V is needed for current to flow in the case of silicon diodes, while a voltage of $V_R = 50$ V is needed for current to flow in the reverse direction. As a result, the pair of diodes keeps the voltage drop across the picoammeter to less than 0.7 V. This is the configuration recommended by Keithley for measuring the capacitance of a system. We choose the resistance in Fig. 3.1 to be $R = 80$ MΩ. The high resistance is important for two reasons. First, it increases the accuracy of our charge measurement. Since we calculate our charge as the integral of the current over time, slowing down the charging process gives us the time resolution needed to obtain an accurate integral. Second, the high resistance further protects the picoammeter and diodes from large voltage drops, as it acts as a voltage divider, causing the applied voltage to mainly drop across the resistor and not across the picoammeter.

The picoammeter is controlled through a custom script in Matlab. This script inputs

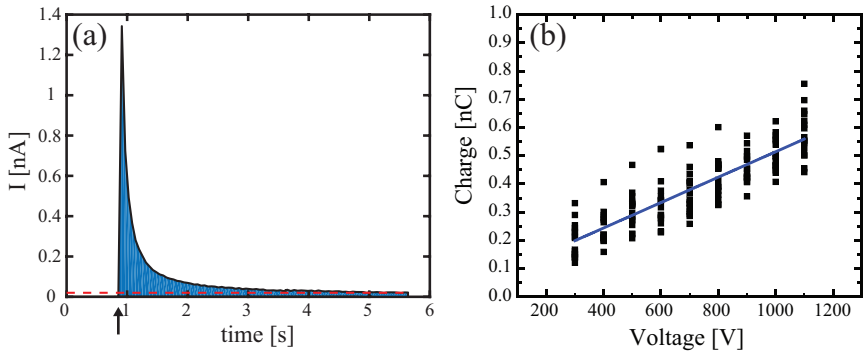

Figure 3.2: (a) A typical curve of current vs. time. The dashed line represents the long time current that is subtracted. (b) The measured Q as a function of V of just the needle immersed in silicone oil. The line is the best fit to find the capacitance.

the relevant parameters, corrects for zero currents, tells the picoammeter when to start and for how long to record, and transfers the data from the picoammeter to the computer. An important input parameter is the number of power line cycles (NPLC), which is the number of cycles over which the picoammeter outputs an average current. In USA, the frequency of the power is 60 Hz. Therefore, 1 NPLC means that the current will be the average over $1/60$ s. This also sets the rate at which the apparatus can record data. For an non-integer NPLC the noise is high since it integrates over part of a power cycle. At the same time a high NPLC means that it records a data point over a long period of time. We chose a NPLC of 1, since this selection results in good accuracy and high recording rate. At this NPLC the picoammeter records data every 0.0576 s, and thus it takes 17 measurements per second.

A typical current (I) versus time is shown in Fig. 3.2(a). The arrow indicates the time we apply the voltage V. We find that I increases abruptly, to then decrease in time. This corresponds to charging the metallic needle. We see that for this particular experiment the maximum current is ≈ 1.3 nA, as seen in Fig. 3.2(a). An isolated conductor, like the needle, has a capacitance that corresponds to the charge needed to increase its voltage by 1 V, with reference to infinity. This is what is called the self-capacitance, which is what we need to measure in order to correct future experiments.

Note that the current does not go to zero at longer times, as indicated by the dashed line

in Fig. 3.2. This small residual current most likely corresponds to charge leaking though the silicone oil. The conductivity of silicone oil is $\sigma_E \approx 10^{-12}$ S/m. We can calculate the resistance as $R = l/(A\sigma_E)$, where l is the length of the resistor and A its cross-sectional area. In our case, we are using a cubic cuvette with a diameter of 2.5 cm. As a result the resistance of the silicone oil is $R_{S.O.} \approx 4 \cdot 10^{13}$ Ω. In this particular experiment, the voltage applied is 10^3 V, and therefore the residual current corresponds to $I_{res} = V/R_{S.O.} = 25$ pA, which is in agreement with the experimental value of (20 ± 6) pA.

We perform experiments at different voltages while the needle is inside the silicone oil, and we integrate the I vs. t curve after the initial abrupt increase numerically to find the total charge. We perform the integration after we have subtracted I_{res}, to avoid measuring the leaking charge. We measure I for the same V ten times [see Fig. 3.2(b)]. The spread in the data is likely due to variations in the geometry between different experiments. We perform experiments with different needle lengths submerged in the silicone oil, and slightly different distances from the ground, which will likely cause the total charge to vary between experiments. Finally, we perform a linear fit, and identify the slope as the capacitance of the needle; we obtain $C_n = (0.3 \pm 0.1)$ pF. For the linear fit, we do not restrict the intercept to go through zero, but we are leaving it as a free parameter. We find that the intercept of the fit is (0.06 ± 0.02) nC, which is reasonable, since the capacitance should be zero when the applied voltage is zero.

We note that for a capacitor charging at a constant voltage V, the characteristic time is $\tau = R \cdot C$. From the measurement of the capacitance, we find that this would correspond to $\tau \approx 0.1$ ms, which is much smaller than the time we see in our experiments [see Fig. 3.2(a)]. A reason for this difference is that the power supply itself does not reach immediately the desired voltage, and this would translate in the current measurement. Another reason is the fact that the silicone oil is not a perfect insulator, but it has a finite resistance. As a result the presence of the silicone oil could change the effective resistance of the system altering the dynamics.

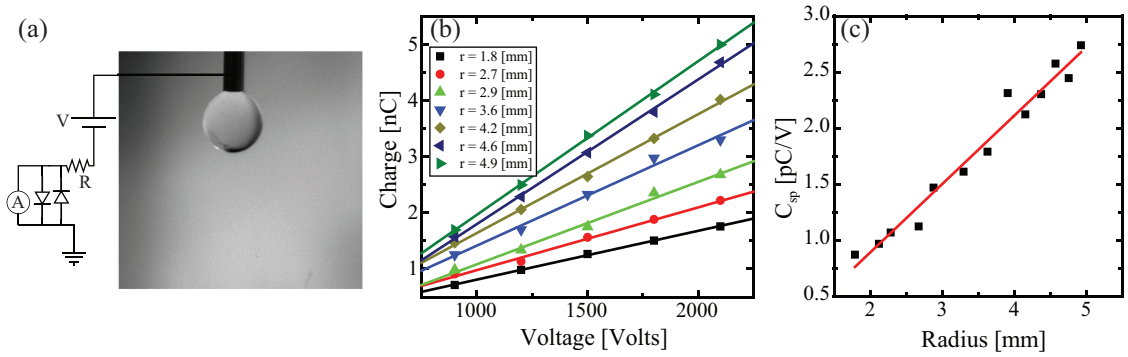

Figure 3.3: (a) The experimental setup for charging spheres. The ground is still the rotating stage. (b) Q as a function V for different values of r. We extract the capacitance, C_{sp}, from the linear fits. (c) The measured C_{sp} as a function r. the fit to the line allows us to measure ϵ_r.

To further test our experimental procedures for charging and measuring Q, we use spherical droplets of water in the silicone oil [see Fig. 3.3(a) for an example]. For isolated spheres the relation between Q, the radius of the spherical droplet r, and the applied voltage V is well known: $V = Q/(4\pi\epsilon_r\epsilon_0 r)$, with ϵ_0 the vacuum permittivity and ϵ_r the relative dielectric constant of the outer medium [100]. Hence, the capacitance is: $C_{sp} = Q/V = 4\pi\epsilon_r\epsilon_0 r$.

We perform experiments for spheres of different volume, and thus, different r, ranging from $r = 1.8$ mm to $r = 4.9$ mm. Similarly to when we charged the needle, we subtract the residual current before integrating the intensity versus time curve. In addition, we subtract the charge associated to the needle, which is given by $Q_n = C_n \cdot V$. Note that Q_n is much smaller than the charge on the sphere, usually less than 10%. We plot Q as a function of V for each individual sphere and we find that they are linearly related [see Fig. 3.3(b)]. We perform linear fits for experiments with constant r to measure the associated capacitance, C_{sp}. Since the capacitance for a sphere is linear in r, we then plot C_{sp} vs. r, as shown in Fig. 3.3(c). We can then perform another linear fit to obtain ϵ_r. We find $\epsilon_r = 4.6 \pm 0.4$. Note that for a silicone oil similar to ours, we have that $\epsilon_r = 3$ at 100 Hz, which is comparable to our results. A reason for the small difference could be due to image charge effects related to the

interaction between the droplet and the air/silicone oil free surface. The image charge Q' represents the surface charge at the free surface. Since silicone oil and air are dielectrics, the image charge is given by [100]:

$$Q' = \frac{\epsilon_{S.O.} - \epsilon_{air}}{\epsilon_{S.O.} + \epsilon_{air}} Q, \tag{3.1}$$

where Q in our case is the charge of the sphere. Taking $\epsilon_{air} = 1$ and $\epsilon_{S.O.} = 3$, we find that the image charge is $Q' = Q/2$, effectively increasing the charge we are measuring by a factor of 1.5, and hence making the effective $\epsilon_r = 4.5$, in agreement with our results. This establishes that we can use our setup to experimentally measure the charge on a liquid droplet. Note that the influence of the needle is not relevant when C is an order of magnitude greater than that measured with the needle alone.

3.2.2 Theoretical Capacitance of a Toroidal Conductor

In order to perform charging experiments with toroidal droplets, we need to understand what to theoretically expect. In addition, an important quantity needed to understand the behavior of charged toroidal droplets is the stress that is exerted on the interface due to the presence of charge. We assume that due to the characteristic time in our experiments, the charge has time to completely relax to the interface, which is then equipotential. Therefore, we treat the torus as a conductor, which implies that the electric field inside the torus is $E_i = 0$ everywhere, and the electric field outside the torus, E_o, is perpendicular to the interface. Using Maxwell's stress tensor for an electric conductor, the total stress on the interface is given by $\tau_E = \frac{1}{2}\epsilon_r\epsilon_0 E_o^2$, where ϵ_r is the relative dielectric permittivity of the outer medium, which is silicone oil in our case [100].

Gauss' Law states that $\boldsymbol{\nabla} \cdot \boldsymbol{E_o} = \frac{\rho}{\epsilon_r\epsilon_0}$, where ρ is the volume charge density. In our case, all the charge resides on the interface of the torus, and therefore $\rho = 0$ outside the torus. In addition, we can write the electric field as $\boldsymbol{E} = -\boldsymbol{\nabla}\Phi$, where Φ is the electric

potential [100]. Combining this with Gauss' law with $\rho = 0$ results in Laplace's equation for the electric potential, i.e. $\nabla^2\Phi = 0$. This equation is separable in the toroidal coordinate system (η, χ, ϕ) if we write the potential as [101]:

$$\Phi(\eta, \chi, \phi) = \sqrt{\cosh(\eta) - \cos(\chi)} H(\eta) X(\chi) \varphi(\phi), \tag{3.2}$$

where $H(\eta)$, $X(\chi)$, and $\varphi(\phi)$ are single variable functions. The Laplacian for a scalar field, ∇^2, in toroidal coordinates is given by:

$$\begin{aligned}\nabla^2\Phi = &\frac{(\cosh(\eta) - \cos(\chi))^3}{a_f^2 \sinh(\eta)} \left[\frac{\partial}{\partial \chi} \left(\frac{\sinh(\eta)}{\cosh(\eta) - \cos(\chi)} \frac{\partial}{\partial \chi} \right) + \frac{\partial}{\partial \eta} \left(\frac{\sinh(\eta)}{\cosh(\eta) - \cos(\chi)} \frac{\partial}{\partial \eta} \right) \right. \\ &\left. + \frac{1}{\sinh(\eta)(\cosh(\eta) - \cos(\chi))} \frac{\partial^2}{\partial \phi^2} \right] \Phi. \end{aligned} \tag{3.3}$$

Substituting equation 3.2 into 3.3, and using separation of variables, we find that the following differential equations must be satisfied:

$$(1 - s^2) \frac{d^2 H}{ds^2} - 2s \frac{dH}{ds} + \left(\left(\left(n - \frac{1}{2} \right) + 1 \right) \left(n - \frac{1}{2} \right) - \frac{m^2}{1 - s^2} \right) H = 0 \tag{3.4}$$

$$\frac{d^2 X}{d\chi^2} + n^2 X = 0 \tag{3.5}$$

$$\frac{d^2 \varphi}{d\phi^2} + m^2 \varphi = 0 \tag{3.6}$$

where $s = \cosh(\eta)$, and m and n are constants. Note that equations 3.4 is the general Legendre differential equation of degree $n - \frac{1}{2}$ and order m. As a result the solution is $H = \left\{ P^m_{n-1/2}(s), Q^m_{n-1/2}(s) \right\}$, a linear superposition of the associated Legendre polynomials of the first and second kind; the curly brackets denote a linear superposition of the arguments for different n and m.

The solution to equation 3.5 is $X(\chi) = \{\cos(n\chi), \sin(n\chi)\}$, while the solution to equation 3.6 is $\varphi(\phi) = \{\cos(m\phi), \sin(m\phi)\}$. A torus is 2π-periodic in χ and ϕ. Hence, the electric potential should be the same at χ and at $\chi + 2\pi$, and similarly for ϕ. Due to these periodic

boundary conditions, $m, n \in \mathbb{N}$. In addition, due to the azimuthal symmetry, the electric potential does not depend on ϕ. Therefore, $m = 0$ and $\varphi = constant$. In addition, we have up-down symmetry with respect to the $z = 0$ plane, which implies that $X(\chi) = X(-\chi)$ and thus that $X(\chi) = \{\cos(n\chi)\}$. Finally, we are looking to calculate the electric field ouside the torus, that is for $\eta < \eta_0 = \cosh^{-1}(R_0/a_0)$. However, $Q_n^m(\cosh(\eta))$ diverges at $\eta = 0$. Therefore the coefficients in the linear expansion of $H(\eta)$ corresponding to the Q_n^m polynomials are set equal to zero. With all these considerations, the general form for the electric potential outside of a torus is [101]:

$$\Phi = \sqrt{\cosh(\eta) - \cos(\chi)} \sum_{n=0}^{\infty} A_n \cos(n\chi) P_{n-\frac{1}{2}}(\cosh(\eta)), \tag{3.7}$$

where $P_{n-\frac{1}{2}} = P^0_{n-\frac{1}{2}}$ and A_n are coefficients that need to be determined. We find A_n by using a boundary condition: $\Phi = V$ at the interface, where V is the applied voltage, and the interface is defined by $\eta = \eta_0$. We isolate the sum in equation 3.7 and we write it as:

$$\frac{V}{\sqrt{\cosh(\eta_0) - \cos(\chi)}} = \sum_{n=0}^{\infty} A_n \cos(n\chi) P_{n-\frac{1}{2}}(\cosh(\eta_0)). \tag{3.8}$$

Therefore, the right hand side can be interpreted as the cosine Fourier series of the left-hand side function. Note that this function is a 2π-periodic even function, and that it fulfills the Dirichlet conditions. Therefore, it can be expanded in a cosine Fourier series. Hence, the coefficients in this expansion are:

$$A_n P_{n-\frac{1}{2}}(\cosh(\eta_0)) = \frac{2 - \delta_{0n}}{2\pi} \int_{-\pi}^{\pi} \frac{V \cos(n\chi')d\chi'}{\sqrt{\cosh(\eta_0) - \cos(\chi')}},\ n = 0, 1, 2, 3... \tag{3.9}$$

Since $Q_{n-\frac{1}{2}}(\cosh(\eta)) = \frac{1}{2\sqrt{2}} \int_{-\pi}^{\pi} \frac{\cos(n\chi)d\chi}{\sqrt{\cosh(\eta)-\cos(\chi)}}$ [89], then:

$$A_n = \frac{\sqrt{2}V(2 - \delta_{on})}{\pi} \frac{Q_{n-\frac{1}{2}}(\cosh(\eta_0))}{P_{n-\frac{1}{2}}(\cosh(\eta_0))}. \tag{3.10}$$

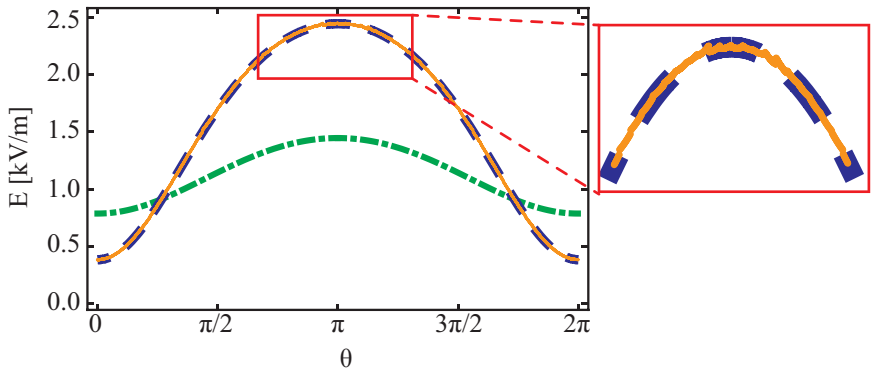

Figure 3.4: Analytical calculation of E_o as a function of θ with $V = 2$ kV, $a_0 = .4$ m for $\xi = 2.5$ $(- -)$ and $\xi = 20$ $(- \cdot -)$. The solid line corresponds to the numerical simulation using COMSOL in the case of $\xi = 2.5$.

We then know the electric potential everywhere outside the torus. To obtain the electric field, we use the gradient in generalized orthogonal coordinates:

$$\boldsymbol{\nabla} = \frac{\hat{\boldsymbol{e}}_{\mathbf{1}}}{h_1}\frac{\partial}{\partial q_1} + \frac{\hat{\boldsymbol{e}}_{\mathbf{2}}}{h_2}\frac{\partial}{\partial q_2} + \frac{\hat{\boldsymbol{e}}_{\mathbf{3}}}{h_3}\frac{\partial}{\partial q_3}, \tag{3.11}$$

where $h_i^2 = g_{ii}$. We are interested in the normal component of the electric field at the interface. This is given by:

$$E_\eta = -\frac{\cosh(\eta) - \cos(\chi)}{a_f}\frac{\partial \Phi}{\partial \eta}. \tag{3.12}$$

We use the relation between χ and θ, and look at how $-E_\eta(\eta = \eta_0) = E_o(r = a_0)$ depends on θ. We see that for a torus with $R_0/a_0 = 2.5$, $E_o(r = a_0)$ is significantly larger at $\theta = \pi$ than at $\theta = 0$, as shown by the dashed line in Fig. 3.4. Increasing the aspect ratio results in a smaller difference between the value of $E_o(r = a_0)$ at $\theta = 0$ and at $\theta = \pi$. In the limit of $\xi \to \infty$, we approach the cylindrical limit, where no asymmetry is expected. Increasing ξ, reduces the role of curvature resulting in a more uniform charge distribution.

To validate the analytical solution, we perform finite element simulations using COMSOL for the electric field around a conducting torus. Since it is not possible in the simu-

lation to set the ground to be at infinity, we set the ground to be a sphere of radius $100R_0$ around the torus. The result is shown by the solid line in Fig. 3.4, for the case of $\xi = 2.5$. We see that the analytical and simulation curves lie on top of each other. The small bumps in the simulation seen in the magnified panel in Fig. 3.4 come from the individual finite coarse elements in the simulation.

Note that the normal vector $\hat{\boldsymbol{n}} = -\hat{\boldsymbol{e}}_{\eta}$, since $\hat{\boldsymbol{e}}_{\eta}$ points towards the inside of the torus. The surface charge density, σ_q, can be obtained from the fact that the electric field jumps from zero to $\boldsymbol{E}|_{\eta=\eta_0}$ at the interface:

$$\sigma_q(\chi) = \epsilon_r\epsilon_0\hat{\boldsymbol{n}}\cdot\boldsymbol{E}\Big|_{\eta=\eta_0} = -\epsilon_r\epsilon_0 E_{\eta}(\eta=\eta_0) \Rightarrow$$
$$\sigma_q = \frac{\epsilon_r\epsilon_0\sinh(\eta_0)}{a_f}\left(\frac{V}{2} + (\cosh(\eta_0)-\cos(\chi))^{\frac{3}{2}}\sum_{n=0}^{\infty}A_n\cos(n\chi)P'_{n-\frac{1}{2}}(\cosh(\eta_0))\right) \tag{3.13}$$

Note that the prime denotes a derivative with respect to the argument, i.e. $s_0 = \cosh(\eta_0)$, and it is not to be confused with differentiation with respect to η_0.

To obtain Q for a toroidal conductor, we need to integrate equation 3.13 over the surface of the torus. In order to do this, we use the chain rule and write that $\sum_{n=0}^{\infty}A_n\cos(n\chi)P'_{n-\frac{1}{2}}(s_0) = \frac{\partial}{\partial s_0}\left(\sum_{n=0}^{\infty}A_n\cos(n\chi)P_{n-\frac{1}{2}}(s_0)\right) - \sum_{n=0}^{\infty}\frac{\partial A_n}{\partial s_0}\cos(n\chi)P_{n-\frac{1}{2}}(s_0)$, where $s_0 = \cosh(\eta_0)$. The first term is simplified using equation 3.8. Taking the derivative of this term, results in a contribution that cancels out with the $\frac{V}{2}$ term in equation 3.13. Using the result for A_n (see equation 3.10), we find that:

$$\frac{\partial A_n}{\partial s_0} = \frac{\sqrt{2}V(2-\delta_{on})}{\pi}\frac{Q'_{n-\frac{1}{2}}(s_0)P_{n-\frac{1}{2}}(s_0) - P'_{n-\frac{1}{2}}(s_0)Q_{n-\frac{1}{2}}(s_0)}{(P_{n-\frac{1}{2}}(s_0))^2} \Rightarrow$$
$$= -\frac{\sqrt{2}V(2-\delta_{on})}{\pi}\frac{1}{(P_{n-\frac{1}{2}}(s)\sinh(\eta_0))^2}$$

where we have used the identity $P'_{n-\frac{1}{2}}Q_{n-\frac{1}{2}} - P_{n-\frac{1}{2}}Q'_{n-\frac{1}{2}} = \frac{1}{\sinh^2(\eta)}$, where as before the prime

denotes a derivative with respect to $s = \cosh(\eta)$ [90]. Finally:

$$\sigma_q = \frac{\epsilon_r \epsilon_0}{a_f}(\cosh(\eta_0) - \cos(\chi))^{\frac{3}{2}} \sum_{n=0}^{\infty} \frac{\sqrt{2}V(2-\delta_{on})}{\pi} \frac{\cos(n\chi)}{P_{n-\frac{1}{2}}(\cosh(\eta_0))\sinh(\eta_0)}. \tag{3.14}$$

We then use that the area element in toroidal coordinates is $dA = \sqrt{g_{\chi\chi} g_{\phi\phi}} d\chi d\phi$, and obtain the total charge as:

$$Q = \int_0^{2\pi} \int_{-\pi}^{\pi} \sigma_q \sqrt{g_{\chi\chi} g_{\phi\phi}} d\chi d\phi. \tag{3.15}$$

Using the equations for $g_{\chi\chi}$ and $g_{\phi\phi}$ (equation 2.11), and trivially integrating over ϕ, we arrive at:

$$Q = \sum_{n=0}^{\infty} \frac{2\sqrt{2}\epsilon_r \epsilon_0 V(2-\delta_{on}) a_f}{P_{n-\frac{1}{2}}(\cosh(\eta_0))} \left[\int_{-\pi}^{\pi} \frac{\cos(n\chi')d\chi'}{\sqrt{\cosh(\eta_0) - \cos(\chi')}} \right]. \tag{3.16}$$

The integral inside brackets is equal to $2\sqrt{2} Q_{n-\frac{1}{2}}(\cosh(\eta_0))$, with $\cosh(\eta_0) = R_0/a_0 = \xi$ and $a_f = \sqrt{R_0^2 - a_0^2} = a_0\sqrt{\xi^2 - 1}$. The capacitance of a torus, $C = Q/V$, is thus given by:

$$\frac{C}{a_0} = 8\epsilon_r \epsilon_0 \sqrt{\xi^2 - 1} \sum_{n=0}^{\infty} (2 - \delta_{0n}) \frac{Q_{n-\frac{1}{2}}(\xi)}{P_{n-\frac{1}{2}}(\xi)}. \tag{3.17}$$

Note that, C scales linearly with a_0 and also depends on ξ. We recall that this formula is the same as the one reported in Ref. [101], where they calculated Q by using an asymptotic expansion of E_o as $\eta \to 0$, which corresponds to the far-field approximation of E_o. Then by using Gauss' Law and calculating the electric flux for a large sphere, they obtained Q.

3.2.3 The Capacitance of Liquid Tori

To obtain the capacitance of a toroidal droplet, we proceed as in our prior experiments and apply a voltage V, measure $I = I(t)$, and obtain Q by integration. We do this for different aspect ratios and find that C/a_0 increases with increasing aspect ratio, as shown in Fig. 3.5. A fit of the data to equation 3.17 with ϵ_r as a free parameter correctly captures

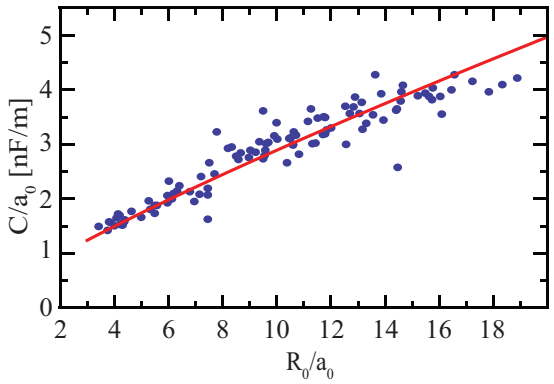

Figure 3.5: The experimental measured C/a_0 as a function of ξ, with the solid line corresponding to the best fit to the analytical solution.

the experimental results, as shown by the line in Fig. 3.5. We obtain $\epsilon_r = 3.7 \pm 0.4$, consistent with our results for spheres. The small difference with spherical droplets can be due to small distance differences from the grounded rotating stage, since the capacitance will increase with decreasing distance.

The observed agreement with the theory for a conducting toroidal capacitor implies that we can treat the toroidal droplets as a perfect conductor in the remainder of our experiments. This is consistent with the fact that the charge relaxation time for our system is much smaller than any other relevant time scale in our experiments. The charge relaxation time is given by $\tau_\epsilon = \epsilon_i/\sigma_i$, where ϵ_i and σ_i are the dielectric constant and conductivity of the inner liquid, respectively. In our experiments, we generate toroidal droplets using glycerol, therefore $\epsilon_{glyc} = 42.5\epsilon_0$ and $\sigma_{glyc} = 2.87 \cdot 10^{-6}$ S/m [102] resulting in $\tau_\epsilon = \epsilon_{glyc}/\sigma_{glyc} \approx 0.13$ ms. Since this time is about four orders of magnitude smaller than the typical time scale in our experiments, the charge has enough time to relax to the interface of the torus. As additional confirmation, we did experiments with a mixture of water and 16 mM sodium dodecyl sulfate as inner liquid, which has $\tau_\epsilon = 6.4$ ns. The results were consistent with the glycerol experiments.

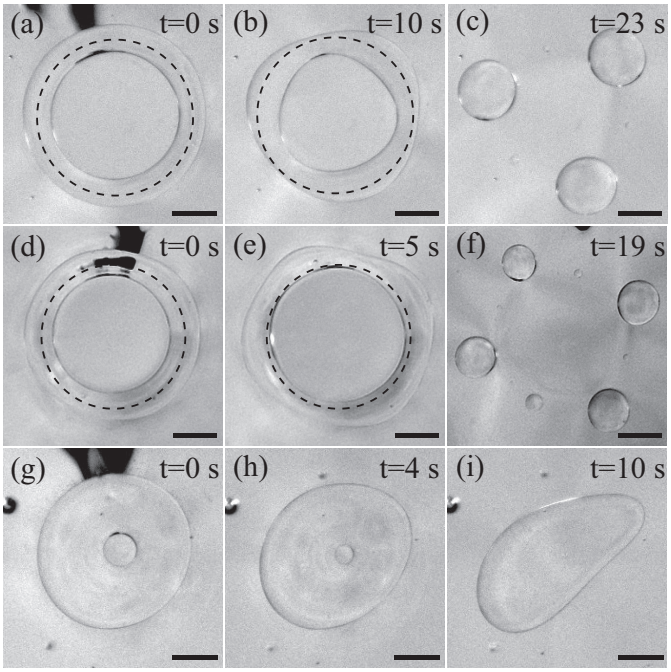

Figure 3.6: Snapshots of the evolution of a torus with (a-c) $R_0/a_0 \approx 5.3$ and $V = 2$ kV, (d-f) $R_0/a_0 \approx 5.1$ and $V = 4$ kV, and (g-i) $R_0/a_0 \approx 1.6$ and $V = 4$ kV. The dashed circles in (a,b) and (c,d) correspond to the central circle at time t=0. While in (b) the handle has clearly shrunken, in (e) it has clearly expanded. The scale bar in all images is 2 mm.

3.3 Shrinking vs. Expansion

3.3.1 Observations Indicating a Shrinking to Expansion Transition

The evolution of the charged toroidal droplet qualitatively changes compared with its uncharged counterpart; while for $\xi \approx 5.3$ and $V = 2$ kV, the droplet shrinks, as shown in Fig. 3.6(a-c), where we highlight the central circle at time $t = 0$ with a dashed line, for $\xi \approx 5.1$ but at a higher voltage of $V = 4$ kV, the toroidal droplet expands, as shown in Fig. 3.6(d-f). In addition, while the toroidal droplet breaks into three spheres for $V = 2$ kV, it breaks into four for 4 kV. This suggests that the wavelength of the fastest unstable mode is smaller with a larger charge, consistent with theoretical expectations [33]. Interestingly, in the case of tori with low ξ and high V, we observe that the inner radius decreases while the outer radius expands. This results in unconventional shape changes, as shown in Fig. 3.6(g-i). We note that the black shadow in the upper part of Fig. 3.6(a,d,g) is due to the

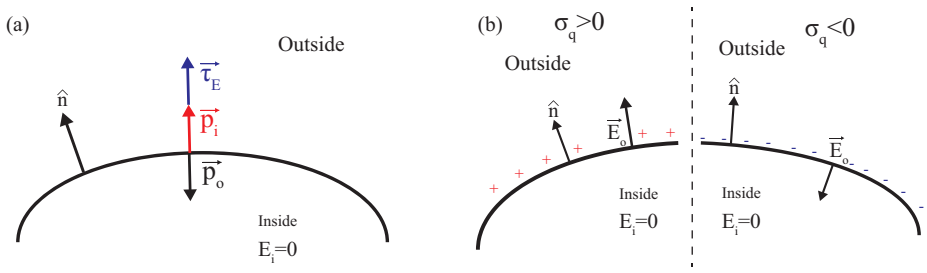

Figure 3.7: (a) A schematic of the stress balance at a charge interface showing that the electric stress is perpendicular at the interface and along $\hat{\boldsymbol{n}}$. (b) A schematic of the direction of the electric field based on the sign of σ_q and the direction of the electric field.

injection needle, which we remove after the formation and charging of the toroidal droplet. To understand the behavior of an expanding torus, we return to the arguments from Section 2.3.2 on the evolution of neutral toroidal droplets, where we looked at the pressure jump at the interface of a torus to explain the behavior.

3.3.2 Pressure Jump in a Charged Liquid Torus

Let us consider the normal stress balance at a charged interface. We define the normal vector $\hat{\boldsymbol{n}}$ such that it points towards the outer liquid, as shown in Fig. 3.7(a). The pressure is an isotropic normal stress; this implies that for any arbitrary imaginary interface, the stress is normal to the interface and it has always the same magnitude. Therefore, $\vec{p_{in}} = p_{in}\hat{\boldsymbol{n}}$, while $\vec{p_{out}} = -p_{out}\hat{\boldsymbol{n}}$ as shown in Fig. 3.7. The electric stress, $\vec{\tau_E} = \frac{1}{2}\sigma_q\vec{E_o}$, points along $\hat{\boldsymbol{n}}$, due to electrostatic repulsions between the charges in the torus. This can be easily seen by considering $\vec{E_o}$ and σ_q. In the case of positive surface charge density, $\sigma_q = \epsilon_r\epsilon_0\vec{E_o}\cdot\hat{\boldsymbol{n}} > 0$, and thus $\vec{E_o}$ must point along $\hat{\boldsymbol{n}}$ [see Fig. 3.7(b)]. As a result, $\vec{\tau_E} = \frac{1}{2}\sigma_q\vec{E_o} = \frac{1}{2}\epsilon_r\epsilon_0|E_o|^2\hat{\boldsymbol{n}}$. For the case of negative surface charge density, $\sigma_q = \epsilon_r\epsilon_0\vec{E_o}\cdot\hat{\boldsymbol{n}} < 0$, and thus $\vec{E_o}$ must point along $-\hat{\boldsymbol{n}}$ [see Fig. 3.7(b)]. As a result, $\vec{\tau_E} = \frac{1}{2}\sigma_q\vec{E_o} = \frac{1}{2}\epsilon_r\epsilon_0|E_o|^2\hat{\boldsymbol{n}}$. In either case, $\vec{\tau_E}$ acts perpendicular to the interface along $\hat{\boldsymbol{n}}$. Therefore, the jump in the normal stress at the

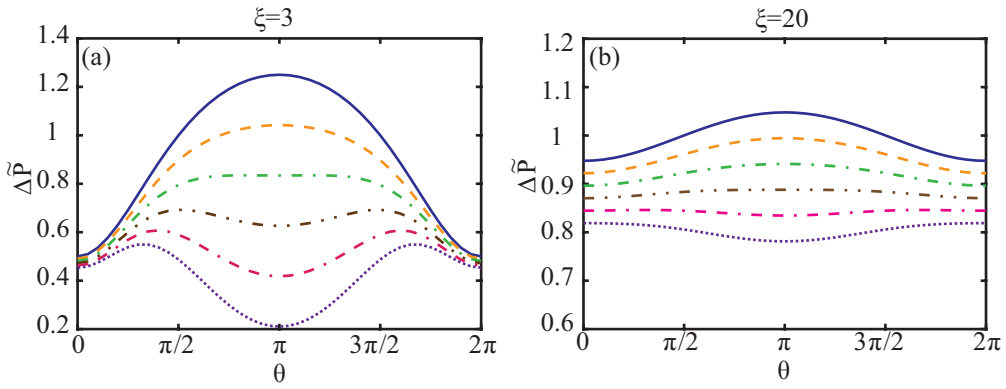

Figure 3.8: The non-dimensional pressure, $\tilde{p}$, as a function of θ in the case of (a) $\xi = 3$ and (b) $\xi = 20$ for different $N_E = 0$ (−), $N_E = 2$ (−−), $N_E = 4$ (− · −), $N_E = 6$ (− · ·−), $N_E = 8$ (· − −·), $N_E = 10$ (··).

interface can be written as:

$$(p_{in} + \frac{1}{2}\epsilon_r\epsilon_0 E^2)\hat{\boldsymbol{n}} - p_{out}\hat{\boldsymbol{n}} = 2\gamma H\hat{\boldsymbol{n}} \Rightarrow p_{in} - p_{out} = 2\gamma H - \frac{1}{2}\epsilon_r\epsilon_0 E^2. \tag{3.18}$$

We see that the presence of charge at the interface results in a decrease in the pressure jump across the interface, and therefore the electric stress acts against the Laplace pressure.

To better understand the effect of charge in the pressure jump across the interface, we non-dimensionalize our pressures. Introducing $\tilde{p} = p/(\gamma/a_0)$ and $\tilde{E} = E/(V/a_0)$; the pressure drop becomes:

$$\Delta\tilde{p}=\tilde{p}_{in} - \tilde{p}_{out} = \frac{\xi - 2\cos(\theta)}{\xi - \cos(\theta)} - N_E\tilde{E}^2(\xi, \theta), \tag{3.19}$$

indicating that $\Delta\tilde{p}$ depends on ξ, θ, and $N_E = \frac{\epsilon_r\epsilon_0 V^2}{2\gamma a_0}$, which is known as the electrocapillary number or electric Bond number, expressing the relative strength of electric and surface tension stresses. We note that the electric field is calculated using the analytical solution for E, as derived in Section 3.2.2.

For $N_E = 0$, which corresponds to the neutral case, the pressure at $\theta = \pi$ is always higher than at $\theta = 0$, as shown in Fig. 3.8(a) for $\xi = 3$. This pressure drop causes shrinking

of the toroidal drop, as discussed in Chapter 2. As we increase N_E, we observe that the maximum in $\Delta\tilde{p}$ at $\theta = \pi$ progressively decreases. Around $N_E = 4$, this peak becomes a local minimum and two maxima appear around $\theta \approx \pi/3$ and $\theta \approx 5\pi/3$. At around $N_E = 8$, $\Delta\tilde{p}$ at $\theta = \pi$ becomes smaller than $\Delta\tilde{p}$ at $\theta = 0$; this would revert the shrinking behavior causing the toroidal droplet to expand. Note that $\Delta\tilde{p}$ cannot be balanced everywhere. As a result, charge is unable to stabilize the toroidal shape and the toroidal droplet will always evolve. Situations where differences in $\Delta\tilde{p}$ between $\theta = 0$ and $\theta = \pi$ are small might correspond to unconventional evolutions like that observed for the thick torus shown in Fig. 3.6(g-i).

The plot in Fig. 3.8(a) corresponds to a torus with $\xi = 3$. For $\xi = 20$, where the torus is locally closer to a cylinder, and we see that $\Delta\tilde{p}$ is much more uniform with respect to θ, as shown in Fig. 3.8(b).

3.3.3 Modeling the Transition to an Expanding Torus

We have seen that for a torus that shrinks, $p_{in}(\theta = \pi) > p_{in}(\theta = 0)$, so we should expect that a torus will expand if $p_{in}(\theta = \pi) < p_{in}(\theta = 0)$. We then model the transition from a shrinking to an expanding torus with the condition: $p_{in}(\theta = 0) = p_{in}(\theta = \pi)$. Using equation 3.19, this results in a cricital $N_{E,c}$ given by:

$$N_{E,c}(\xi) = \frac{\frac{2\xi}{\xi^2-1}}{\tilde{E}^2(\xi,\pi) - \tilde{E}^2(\xi,0)}. \tag{3.20}$$

We find that the critical $N_{E,c}$ increases drastically as $\xi \to 1$, as shown by the solid line in Fig. 3.9(a). This means that we need to apply an increasingly higher V to cause a thick torus to expand, since for low ξ, surface tension stresses are most relevant.

An alternative condition to describe the shrinking to expanding transition can result by considering the energy. The surface tension contribution is γA (see Chapter 2). The

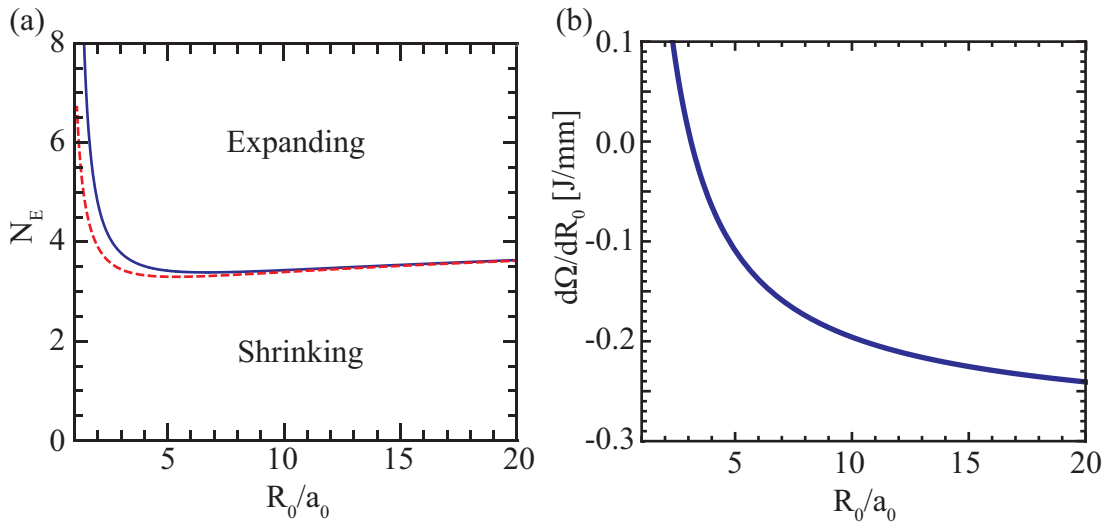

Figure 3.9: (a) The critical N_E to transition from shrinking to an expanding torus from a pressure balance (−) and energy (− −) perspective. (b) $d\Omega/dR_0$ as a function of ξ for a 0.05 ml toroidal droplet using $\gamma = 32$ mN/m, $\epsilon_r = 3.7$, and $V = 2.5$ kV.

electrostatic contribution is given by:

$$E_E = \frac{1}{2}\frac{Q^2}{C} = \frac{1}{2}V^2C. \tag{3.21}$$

At constant Q, the electrostatic energy change due to a change in the capacitance, C, is: $dE_E\big|_Q = -\frac{1}{2}V^2dC$. Therefore:

$$d\Omega = \gamma dA - \frac{1}{2}V^2dC. \tag{3.22}$$

To simplify the math, we write $C = \epsilon_r\epsilon_0 a_0 f(\xi)$, where $f(\xi) = 8\sqrt{\xi^2-1}\sum_{n=0}^{\infty}(2-\delta_{0n})\frac{Q_{n-\frac{1}{2}}(\xi)}{P_{n-\frac{1}{2}}(\xi)}$. Since the volume, Vol $= 2\pi^2\xi a_0^3$, is conserved $da_0 = -\frac{a_0}{3\xi}\,d\xi = -\frac{dR_0}{2\xi}$. As a result, the change in free energy is:

$$d\Omega = \left(2\pi^2 a_0\gamma - \frac{1}{2}\epsilon_r\epsilon_0 V^2\left(\frac{3}{2}\frac{df}{d\xi} - \frac{f}{2\xi}\right)\right)dR_0. \tag{3.23}$$

A torus will shrink if Ω decreases as R_0 decreases, while it will expand if Ω decreases as R_0 increases. At the transition, the torus will remain at the fixed R_0, corresponding to $d\Omega = 0$. Therefore, this condition provides an alternative critical $N_{E,c}$ for the shrinking to expanding

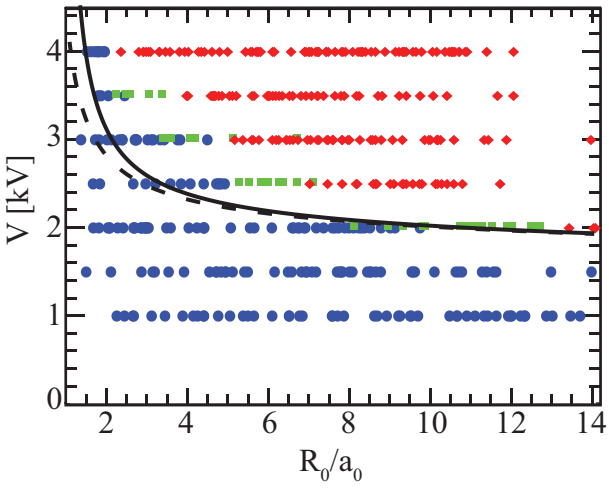

Figure 3.10: Shrinking tori (circles), expanding tori (rhombus), and tori whose centra circle remain stationary (squares) in a $V - \xi$ state diagram. The solid line is the theoretical transition line separating shrinking from expanding tori using the pressure balance ($-$) and energy minimization ($--$).

transition:

$$N_{E,c} = \frac{2\pi^2}{\left(\frac{3}{2\sqrt{\xi^2-1}}\frac{df}{d\xi} - \frac{f}{2\xi}\right)}. \tag{3.24}$$

This critical $N_{E,c}$, shown by the dashed line in Fig. 3.9(a), qualitatively agrees with the critical $N_{E,c}$ obtained using the pressure. This agreement is quantitative at high ξ. At lower ξ, the $N_{E,c}$ obtained using the energy arguments is lower that the $N_{E,c}$ using the pressure jump. This deviation is probably due to the fact that for the stress balance model, we only considered the pressure at two points, $\theta = 0$ and $\theta = \pi$, and we did not consider the contribution to the stress along the direction of expansion for all θ.

Note that $d\Omega/dR_0$ is a decreasing function of ξ, as shown in Fig. 3.9(b). As a results, $\frac{d^2\Omega}{dR_0^2} < 0$, and therefore Ω is a maximum at $N_{E,c}$, reflecting that the situation is of unstable equilibrium, emphasizing that stabilizing a torus with charge is not possible.

In either model, $N_{E,c}$ exhibits a minimum around $\xi = 4$. We hypothesize that this is because both ξ and N_E depend on a_0. If we consider a process where a toroidal droplet with a constant volume and constant V expands, its tube radius, a_0, decreases as the aspect ratio increase, hence causing N_E to increase. In addition, as ξ approaches its minimum

value of 1, curvature will dominate causing $N_{E,c}$ to increase. As a result a minimum will appear in the theoretical models. We also note that both of these approaches to calculate $N_{E,c}$ are based on the assumption that the torus remains a torus at all ξ; that is, that the cross section remains circular.

To test the expectations from our model, we perform experiments with a constant injected volume of 0.05 mL and changed the applied voltage and the aspect ratio of the torus. We plot our results in a $V-\xi$ diagram in Fig. 3.10, using circles for tori that shrink, rhombi for tori that expand, and squares for tori whose central circle remains unchanged. We can easily translate $N_{E,c}$ to a critical V since all of our experiments are performed at constant volume. This is done by calculating a_0 for our given volume and as a function of ξ, and use this a_0 to convert N_E to V for all ξ. We find that the data follow both models qualitatively, as shown in Fig. 3.10. The deviations from the models seen at lower aspect ratios are likely due to the fact that the cross section of the toroidal droplets for high V and low ξ is far from circular, as assumed in our model. Note that we do not have a minimum for the critical value for V, compared to $N_{E,c}$. This is because we performed the experiments at constant volume. As a result, a_0 decreases as ξ increases, and thus, the voltage needed to maintain a constant N_E decreases. Nevertheless, the simple balance expressed in our models captures reasonably well the transition from shrinking to expanding seen experimentally.

3.4 Shape and Flow Field of Expanding Toroidal Droplets

We have seen that charge brings qualitative changes to the behavior of a liquid torus. However, the governing equations of motion are still the Stokes equations, since charge only affects the normal stress balance at the interface. Hence, the stream function derived in Chapter 2 is still valid for an expanding torus. As we did for the neutral case in Chapter 2, we can obtain the theoretical velocity field inside the torus as it expands by matching the experimental and theoretical speeds at the interface. However, the charged case is not as easy, because the cross section of the torus deforms much more significantly from a circular

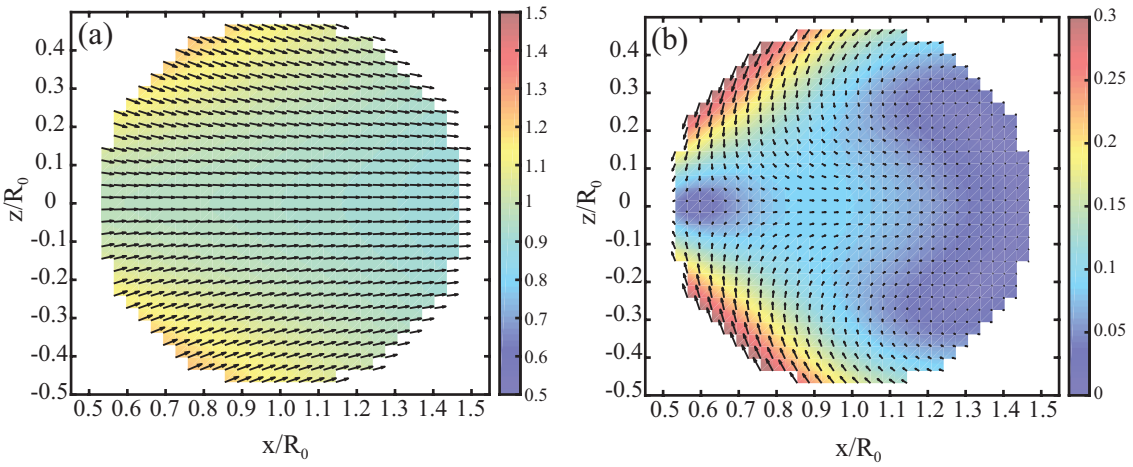

Figure 3.11: The theoretical flow field of a torus with $\xi = 2$ in the (a) lab frame and (b) the frame of reference of the cross section. The magnitude for each mode used is the same and opposite from the one obtained for a shrinking torus in Chapter 2. Colorbars have been scaled with $\langle|\vec{v}|\rangle$

cross section. We can then proceed differently, by considering that the difference between the charged and the neutral case only appears in the normal stress balance. As a result, we expect a velocity field for an expanding torus that is similar to that of a shrinking torus, but with reversed velocity directions. This is reasonable also from considering that the Stokes' equations satisfy time-reversal symmetry. In that case, an expanding droplet has exactly the same and opposite flow field compared to a neutral droplet.

This is shown in Fig. 3.11 (a,b) for a torus with $\xi = 2$, where we have used the inverted coefficients for the different modes as calculated in Section 2.4.5. We find that in the lab frame, the flow field shows that the torus will expand and that the velocity is maximum around $\theta \approx \pm\pi/4$. By subtracting the velocity of expansion, $\vec{v}_{exp}$, we find the flow field in the frame of reference of the cross section, as shown in Fig. 3.11(b). Similarly to the uncharged case, the velocity is maximum around $\theta \approx \pm\pi/4$. In addition, we observe that the velocity points radially outwards at $\theta = 0$ and $\theta = \pi$, while it points radially inwards at $\theta \approx \pm\pi/4$. As a result, we expect the shape of the cross section of the torus to elongate horizontally, in contrast to the neutral case, where it elongated vertically.

To test these expectations, we perform experiments with a torus with $\xi \approx 2.2$ and $V = 6$

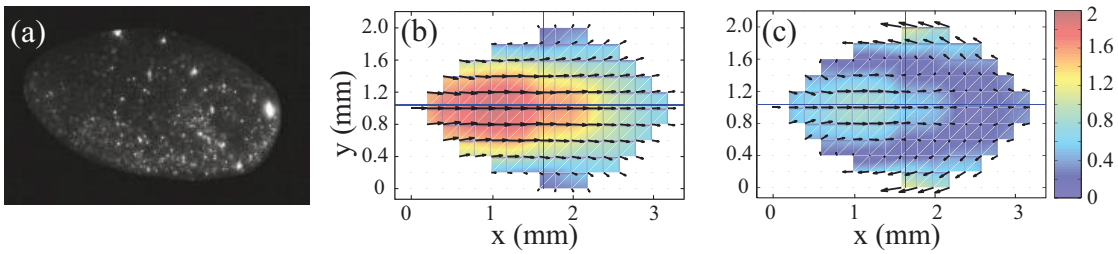

Figure 3.12: (a) An expanding torus, with $\xi \approx 2.2$ and $a_0 \approx 1.6$ mm at $V = 6kV$. (b-c) The flow field inside the torus after the flow field decomposition at the lab frame and in the frame of reference of the cross section, respectively. The magnitude has been scaled with the expanding velocity, v_{ex}.

kV. Right after charging, the torus indeed elongates horizontally, as shown in Fig. 3.12(a). Note however, that the cross section is not symmetric, but rather tilted downwards; the region around $\theta = 0$ is higher than the region around $\theta = \pi$. We believe this is due to the electrostatic repulsion between the needle and the charged torus. Since σ_q is higher at $\theta = \pi$ than at $\theta = 0$, as soon as charging begins, the region around $\theta = \pi$ feels a larger repulsive force than the region around $\theta = 0$, causing the observed asymmetry. From the PIV data, we can obtain the flow field as in Chapter 2, and use the symmetry of a torus to extract the flow field associated to expanding, as shown in Fig. 3.12(b). We then determine the expansion speed by finding the average v_x in the acquired PIV flow field and subtract it to get the flow field in the frame of reference of the cross section [see Fig. 3.12(c)]. We observe a few features that are similar to the theoretical expectations. For example, the velocity is larger closer to the center and for $-\pi/2 < \theta < \pi/2$.

Since obtaining the theoretical flow field assumes a circular cross section, and experimentally the shape is not only not circular, but also not symmetric, comparing the experimental and theoretical boundary velocities does not yield accurate results. Performing a more complete theoretical description, which could account for the coupling between charge, $\vec{v}$ and shape, is thus required. We hope that our experiments here open the way to continuing to develop the theory of charged toroidal droplets.

3.5 Rayleigh-Plateau Instability of Charged Toroidal Droplets

3.5.1 Stability Analysis of Neutral and Charged Viscous Jets

The breakup of a cylindical liquid jet has been a focus of study since the pioneering work of Plateau [76] and Rayleigh [15], who were the first to realize the importance of surface tension in the dynamics of a jet. Rayleigh, specifically, developed the theory for the breakup of an inviscid jet using linear perturbation theory, or linear stability analysis.

Perturbation theory is based on first solving the system of equations in question for the base solution corresponding to the unpertubed system. Then, a perturbation term is added to the base solution and, by using the same set of equations, one finds the condition for the perturbation to either grow or die out. Let p_0, $\boldsymbol{u}_0$, and α_0 be the pressure, velocity, and radius of an unperturbed jet. The corresponding perturbed quantities can then be written as:

$$p = p_0 + \tilde{p}\, e^{\omega t + ikz}, \tag{3.25}$$

$$\boldsymbol{u} = \boldsymbol{u}_0 + \tilde{\boldsymbol{u}}\, e^{\omega t + ikz}, \tag{3.26}$$

$$\alpha = \alpha_0 + \tilde{\alpha}\, e^{\omega t + ikz}, \tag{3.27}$$

where $\tilde{p}$, $\tilde{\boldsymbol{u}}$, and $\tilde{\alpha}$ are the amplitude of the perturbation at $t = 0$, ω is the the growth rate, and $k = \frac{2\pi}{\lambda}$ is the wavenumber of the perturbation, with λ the corresponding wavelength. Equations (3.25,3.26,3.27) are introduced in the equations of motion; the Navier-Stokes equations in our case:

$$\rho\left(\frac{\partial \boldsymbol{u}}{\partial t} + (\boldsymbol{u}\cdot\nabla)\,\boldsymbol{u}\right) = -\boldsymbol{\nabla} p + \mu\Delta\boldsymbol{u}, \tag{3.28}$$

$$\boldsymbol{\nabla}\cdot\boldsymbol{u} = 0, \tag{3.29}$$

where ρ and μ are the density and viscosity of the liquid, respectively. The perturbed

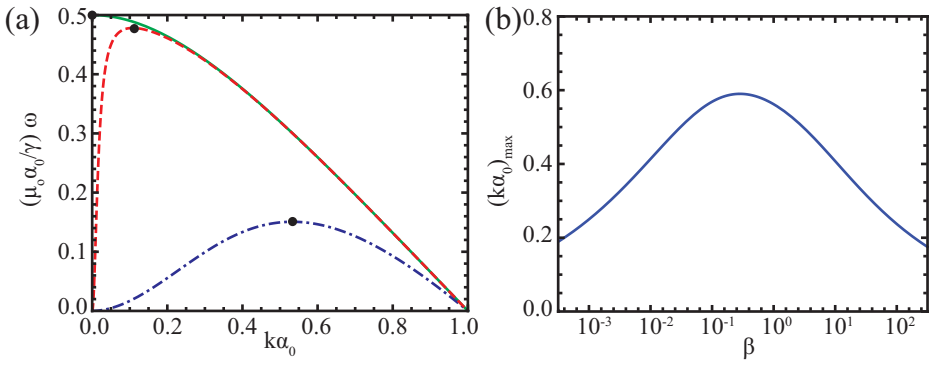

Figure 3.13: (a) The dispersion relation by Tomotika for $\beta = 0$ (−), $\beta = 10^{-3}$ (− −), and $\beta = 1/20$ (− · −). The circles correspond to the maxima of the dispersion relation. (b) $(k\alpha_0)_{max}$ as a function of β.

quantities are also used in the boundary conditions (BCs); these are the kinematic BC that states that both liquids have the same velocity at the interface, the continuity of the tangential stress at the interface that in our case only includes the viscous stress, and the normal stress balance at the interface, which is given by Laplace's equation. Since we are performing a linear stability analysis, we assume that $\frac{\tilde{p}}{p_0}, \frac{\tilde{\boldsymbol{u}}}{\boldsymbol{u}_0}, \frac{\tilde{\alpha}}{\alpha_0} << 1$, and only retain terms up to first order, that is, terms of $O\left(\frac{\tilde{p}}{p_0}\right)$, $O\left(\frac{\tilde{\boldsymbol{u}}}{\boldsymbol{u}_0}\right)$ and $O\left(\frac{\tilde{\alpha}}{\alpha_0}\right)$.

Tomotika performed this stability analysis in the limit of $\rho \to 0$, for a viscous jet inside another immiscible viscous liquid. In this case, he found that:

$$\omega = \frac{\gamma\left(1-(ka)^2\right)}{2\alpha_0\mu_o} g(k\alpha_0, \beta), \tag{3.30}$$

where $\beta = \mu_i/\mu_o$ with μ_i and μ_o the viscosities of the inner and outer liquids, respectively. The relation between the growth rate, ω, and the dimensionless wavenumber, $k\alpha_0$, is called the dispersion relation. We plot equation 3.30 as a function of $k\alpha_0$ for $\beta = 0$, $\beta = 1/1000$, and $\beta = 1/20$ in Fig. 3.13(a). In all cases, the dispersion relation has a maximum; the corresponding mode has dimensionless wavenumber $(k\alpha_0)_{max}$, and corresponds to the fastest unstable mode. Since $(k\alpha_0)_{max}$ grows faster than any other mode, the fastest unstable mode will most likely dominate the dynamics in an experiment [103]. As a result, this will be the

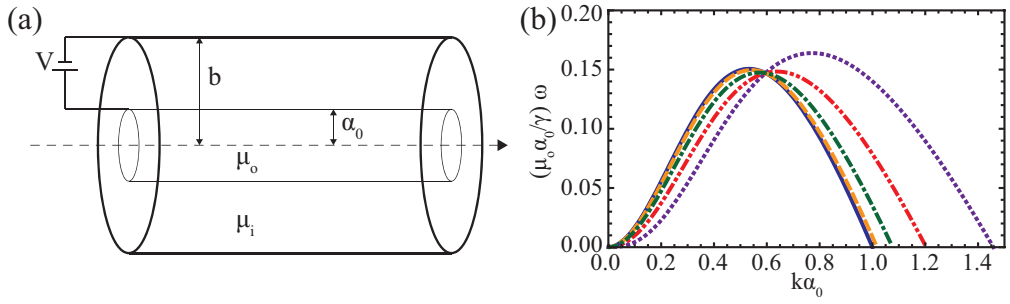

Figure 3.14: (a) Schematic of the geometry for the stability analysis by Wang. A voltage V is applied between the liquid thread and calyndrical wall of radii α_0 and b, respectively. (b) The dispersion relation by Wang with $\beta = 1/20$, $d = 100$, for values $N_E = 0$ $(-)$, $N_E = 0.8$ $(--)$, $N_E = 3.3$ $(-\cdot-)$, $N_E = 7.4$ $(-\cdot\cdot-)$, and $N_E = 13.2$ $(\cdot\cdot)$.

mode most likely to cause breakup of the jet. Interestingly, for $k\alpha_0 > 1 \Rightarrow \lambda < 2\pi\alpha_0$, ω in equation 3.30 is complex with the real part being negative. Therefore, the perturbation decays exponentially in time and the jet does not break; this is the case for all β, and is known as the Rayleigh-Plateau criterion, which was mentioned earlier in Section 2.3. Similar to the free energy argument for a shrinking torus, it can be shown that an infinitesimal perturbation of a jet will decrease Ω only for $\lambda > 2\pi\alpha_0$ [15]. Hence, surface tension is directly responsible for both the stability of a jet to short wavelengths as well as the instability of a jet for longer wavelengths.

Interestingly, we find that $(k\alpha_0)_{max}$ is symmetric with respect to β, as shown in Fig. 3.13(b). However, this symmetry is not about $\beta = 1$, but instead about $\beta \approx 0.28$. As a consequence, a simple exchange of the inner and outer liquids does not correspond to the same situation; in particular, the size of the resultant droplets after breakup will be different.

Wang and Papageorgiou [33] performed a similar stability analysis for a charged viscous jet in another immiscible viscous liquid. In their analysis, the jet is at the center of a cylindrical capillary with radius b. The voltage, V, is applied between the jet, which has a radius α_0, and the outer walls, as shown in Fig. 3.14(a). In this case, the electric field, $\boldsymbol{E}$,

is another quantity that is perturbed:

$$\boldsymbol{E} = \boldsymbol{E_0} + \tilde{\boldsymbol{E}} e^{\omega t + ikz}, \tag{3.31}$$

where $\boldsymbol{E_0}$ the electric field of the base solution and $\tilde{\boldsymbol{E}}$ the amplitude of the perturbation for the electric field at $t = 0$ s. The inner liquid is considered a conductor, and therefore all the charge accumulates at the interface of the jet. As a result, the equations of motion are still the Navier-Stokes equations. However, the electric field in the outer liquid needs to be solved using Laplace's equation, i.e. $\nabla^2\Phi = 0$ where Φ is the electric potential. In addition, the BCs will change. In particular, the outer liquid must satisfy the no-slip boundary condition at the cylindrical capillary with radius b, and the normal stress balance is modified to include the charge as:

$$p_{in} - p_{out} = 2\gamma H - \frac{1}{2}\epsilon_r \epsilon_0 |\boldsymbol{E}|^2. \tag{3.32}$$

As a result, the dispersion relation now depends on two additional parameters, $d = b/\alpha_0$ and $N_E = \frac{\epsilon_r \epsilon_0 V^2}{2\gamma\alpha_0}$. To see the effect of charge, we plot the dispersion relation for different N_E with $\beta = 1/20$ and $d = 100$ [see Fig. 3.14(b)]. We see that $(k\alpha_0)_{max}$ increases as N_E increases implying that the wavelenght of the fastest unstable mode decreases as V increases and that the resultant droplets will have a smaller size. In contrast, the growth rate associated to the fastest ustable mode remains nearly unchanged in the N_E range considered, as shown in Fig. 3.14(b). Additionally, the Rayleigh-Plateau criterion changes, and the jet can still be unstable for $k\alpha_0 > 1$. This is consistent with other theories for inviscid charged liquid jets [31, 94].

3.5.2 Breakup of Charged Toroidal Droplets

Charged toroidal droplets most often break into spherical droplets, irrespective of whether they shrink or expand. In this case, since the torus enforces periodic boundary conditions,

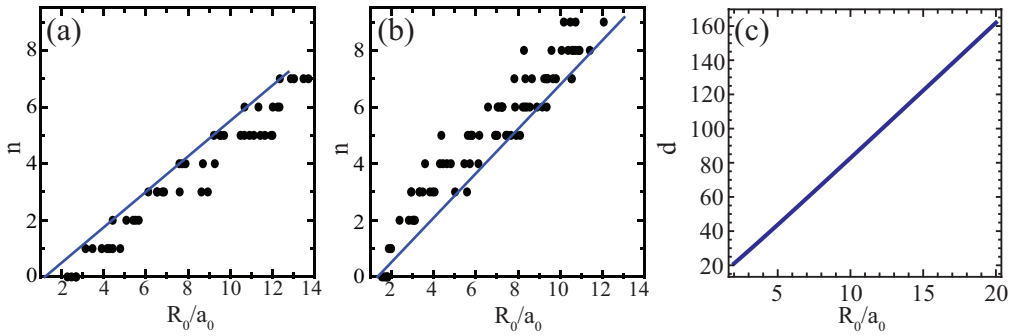

Figure 3.15: Number of droplets, n, as a function of ξ for tori at (a) $V = 1$ kV and (b) $V = 4$ kV. In (a), all tori shrink, and thus we use the leftmost points of the steps to obtain the value of ka_0 associated to the fastest unstable. In (b), all tori expand, and thus we use the rightmost points of the steps to obtain ka_0. (c) The value of d as a function of ξ for which E is on average the same for a torus and a cylinder.

breakup results in an integer number of droplets, n, which depends on the number of wavelengths of the fastest unstable mode that can fit around the circumference of the torus, that is, in a length equal to $2\pi R_0$. As a result,

$$n = \frac{2\pi R_0}{\lambda} = ka_0\, R_0/a_0 = ka_0\, \xi \tag{3.33}$$

Hence, we expect n to be linear with ξ. However, note that n is a discrete variable, and as a result, plotting n versus ξ does not result in a continuous curve; this is true irrespective of V. Our experiments illustrate this, as shown in Fig. 3.15(a,b) for two representative values of V. However, while for small V, the behavior is dominated by shrinking, and thus the torus typically shrinks before it can fit an integer number of wavelengths of the fastest unstable mode, at higher V, the torus typically expands before it can fit an integer number of wavelengths of the fastest unstable mode. The steps reflect that a torus of a given ξ does not typically have an integer length-to-wavelength ratio. As a result, the torus either shrinks or expands before it can fit an integer number of wavelengths of the fastest unstable mode. As this happens, ξ changes along a step until breakup can happen. At that point, the torus breaks. Hence, to obtain the value of ka_0 associated to the fastest unstable mode at different V, we use the leftmost points of the steps at low V, where the torus

Table 3.1: The fastest unstable mode, ka_0, for different voltages obtained from experiments and theory. We quantify the effect of d by calculating the theoretical mode for different values of d.

V	ka_0	Theory: $d = 100$	Theory: $d = 70$	Theory: $d = 40$
1.0 kV	0.59 ± 0.01	0.53	0.53	0.53
1.5 kV	0.60 ± 0.03	0.54	0.54	0.55
2.0 kV	0.63 ± 0.03	0.57	0.57	0.58
3.5 kV	0.79 ± 0.04	0.74	0.81	0.95
4.0 kV	0.85 ± 0.05	0.85	0.94	1.14

shrinks [see Fig. 3.15(a)], and the rightmost points of the steps at high V, where the torus expands [see Fig. 3.15(b)]. Using these points, we confirm that n is linear with ξ, consistent with our expectations. The slopes of the corresponding linear fits provide the value of ka_0 corresponding to the fastest unstable mode. We find that ka_0 increases with increasing V, as shown in Table 3.1. This indicates that λ decreases with increasing V and that breakup results in smaller droplets. This is in qualitative agreement with theoretical predictions for the breakup of electrified jets [31], and was already seen in Fig. 3.6(a-c), where $V = 2$ kV and there are three drops after breakup, and Fig. 3.6(d-f), where $V = 4$ kV and there are four drops after breakup for toroidal droplets with the same ξ.

To quantitavely account for the breakup results, we consider the theoretical framework introduced in Section 3.5.1 [33]. The parameters in the theory are $d = b/\alpha_0$ and $N_E = \epsilon_r\epsilon_0 V^2/2\gamma a_0$. We can directly calculate the value of N_E in our experiments. However, obtaining d is not obvious, since the geometry in the theory and the geometry in the experiment different. We then choose d such that the electric stress on the surface of the jet in the theory is the same as the average electric stress on the surface of our tori. Recall that the theory considers two concentric cylinders subjected to a voltage difference V [see Fig. 3.14(a)]. For this geometry, the electric field at the interface of the jet is given by:

$$E_{cyl} = \frac{V}{\alpha_0\, ln(d)}. \tag{3.34}$$

We calculate d from the condition:

$$E_{cyl} = \langle E_o(r = a_0)\rangle_\theta. \tag{3.35}$$

Note that we average along θ since $E_o(r = a_0)$ depends on the polar angle. Note also that d will also depends on ξ, as $\langle E_o(r = a_0)\rangle_\theta$ also depends on ξ [see Fig. 3.15(c)]. Since the breakup experiments considered in Table 3.1 correspond to values of ξ around 10 using this value, we obtain $d = 100$. We use this value to calculate $(ka_0)_{max}$. We then see that $(ka_0)_{max}$ increases with V, as shown in Table 3.1. In addition, the theoretical results are consistent with our experimental results, as also seen in the same table. To ilustrate the effect of changing d within values that are not far from those in our experiments, we calculate $(ka_0)_{max}$ for $d = 70$ and $d = 40$. These correspond to tori with ξ around 8 and 5, respectively. We observe that $(ka_0)_{max}$ increases as V increases, and that for $V \leq 2$ kV, the results are essentially the same. However, the values start to differ significantly for $V \geq 3.5$ kV, specifically for $d = 40$. In this cases, the tori expand and the points considered to extract $(ka_0)_{max}$ have $\xi > 6$. As a result, the theoretical change of $(ka_0)_{max}$ with V is robust and captures the experimental result reasonably well.

3.6 Saffman-Taylor Instability of Charged Toroidal Droplets

3.6.1 Introduction

The viscous fingering instability refers to the formation of finger-like structures when a fluid displaces another fluid of a higher viscosity in a confined quasi-two dimensional flow [104]. As a result, it often appears in two phase flow in porous media, which is relevant for applications like enhanced oil recovery, hydrology, and sugar refinement [105–107]. This phenomenon is typically explored experimentally under confinement between two parallel plates, in the so-called Hele-Shaw cell. In the initial experiments, the displacement was driven by air pressure or suction [104]. This pressure drives the upper liquid to displace the

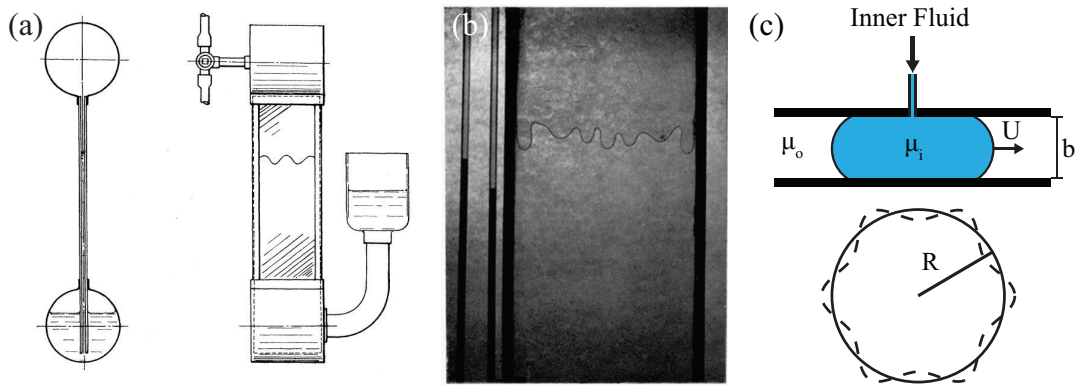

Figure 3.16: (a) A schematic of the initial Hele-Shaw cell experiments [104], where the upper liquid was driven by applying controlled air pressure. (left) A side-view shows that the plates are separated by a small distance, and (right) a front view showing the system used to controled the air pressure. (b) Experiment where air (top) displaces glycerine (bottom) in a Hele-Shaw cell. (c) Schematic of viscous fingering in a Hele-Shaw cell from a (top) side-view showing the plate-plate separation, b, and velocity, U, of the interface and (bottom) top-view showing an initial unperturbed interface with radius R and a perturbation for $n = 6$.

lower, as shown in Fig. 3.16 (a,b). Saffman and Taylor derived theoretically and determined experimentally that the critical condition for viscous fingering is that the displaced fluid must have a higher viscosity than the displacing fluid. Subsequent experiments used a radial Hele-Shaw cell, where the liquid is pumped through a hole in one of the two plates and moves radially outwards, as shown in Fig. 3.16(c). In either realization, the interface between the displacing and the displaced liquid moves at a constant speed in the early stages, before viscous fingers develop [see Fig. 3.16(c)].

To understand the instability let us consider the relevant equations of motion of the fluid. The quasi-two dimensional nature is captured by considering the average velocity along z. By defining the velocity as $v(r) = \langle u(r,z)\rangle_z$ and considering Poiseuille flow [79], we find that:

$$v(r) = -\frac{\kappa}{\mu}\frac{dp}{dr}, \tag{3.36}$$

where κ is the permeability, whose values depends on the geometry of the problem. In the case of a Hele-Shaw consisting of two parallel plates $\kappa = b^2/12$. Equation 3.36 is called

Darcy's law and relates the average velocity of a confined fluid with the pressure drop. Using equation 3.36, we consider the pressure change across the interface in Fig. 3.16(c) associated to a virtual local displacement δr, $\delta p = p_i - p_o = -[(\mu_i - \mu_o)v/\kappa]\delta r$. We see that if $\mu_o > \mu_i$, then $\delta p > 0$ and the instability that caused δr amplifies [108].

3.6.2 Observations of Viscous Fingers in Charged Toroidal Droplets

In order to facilitate the expansion of the torus when charged, we lower the interfacial tension by using water with 16 mM sodium dodecyl sulfate (SDS) as inner liquid, and 2% w/w 65 cSt aminopropyl terminated silicone (ATSO) in 60,000 cSt trimethyl terminated silicone oil as outer liquid. For this pair of liquids, the interfacial tension, as measured using the pendant drop method [109], is $\gamma = (3.0 \pm 0.5) \cdot 10^{-4}$ N/m. This value of γ is two orders of magnitude lower compared to the previous experiments. We measure the dynamic viscosity of the outer liquid to be $\mu_o = (53 \pm 1)$ Pa $\cdot$ s using steady state shear rheology. The viscosity of the inner liquid is $\mu_i = 1$ mPa $\cdot$ s. Therefore, $\mu_i < \mu_o$, and our liquids satisfy the criterion for the Saffman-Taylor instability to develop. Note, that this criterion is for two fluids with a flat interface. In the case of a circular interface, the velocity of the fluid-fluid interface has to have a critical value that depends on the viscosity contrast, R, γ, and the number of fingers developed (n) [110]. Note that there is always a sufficiently large n for any non-zero velocity, such that the interface is unstable.

The typical rotation speed of the cuvette for generating the toroidal droplets is $\omega \sim 0.5$ rad/s, the amount of liquid pumped is $20 - 40$ μL, and the range of voltages applied is $0 - 1500$ V. Since the surface tension is low, the experiments can take as long as 10 minutes, which is enough time for charge to leak through the silicone oil. We have observed this charge leak indirectly in experiments where we removed the needle after making the droplet. In these experiments, tori that initially expanded reverted to shrinking after $3 - 4$ minutes. We believe that this phenomenon is because of charge leaking through the silicone oil, which in turn will reduce the strength of the electric stresses. As a result, we perform

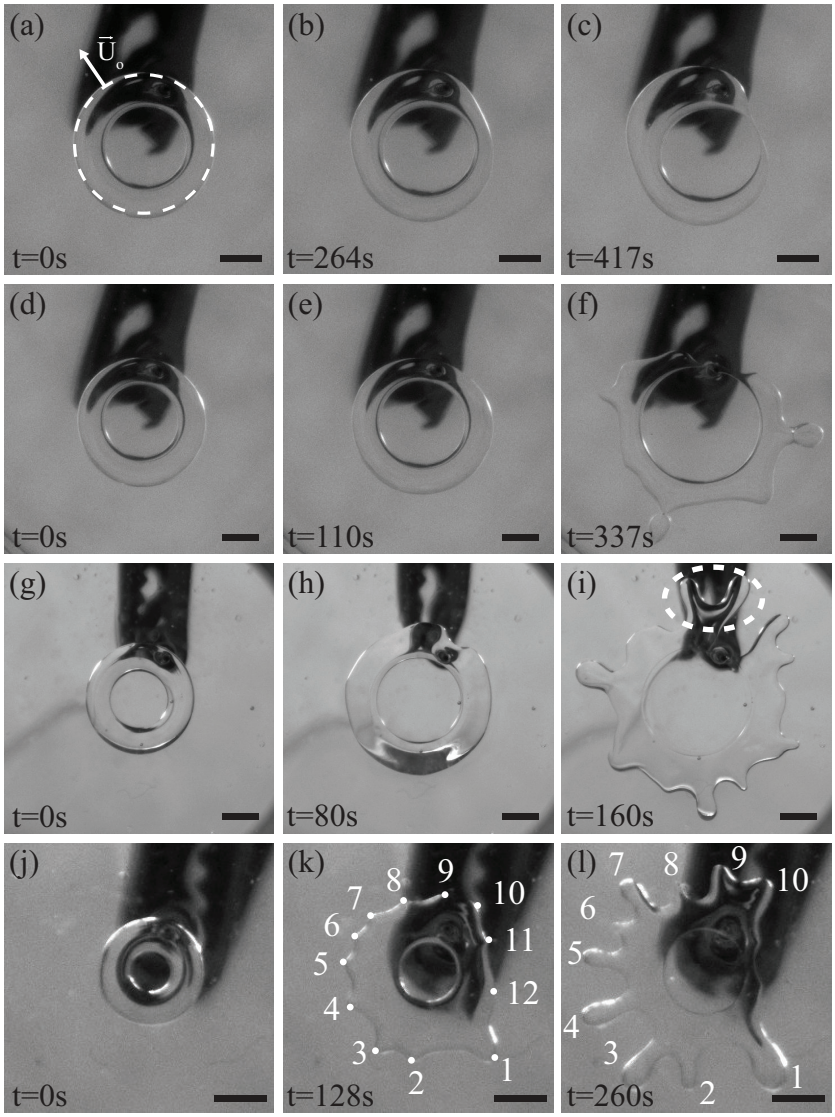

Figure 3.17: Snapshots of the evolution of (a-c) a breaking torus with $R_0/a_0 = 3.5$ and $V = 500$ V, (d-f) a torus with $R_0/a_0 = 3.7$ and $V = 800$ V where both break-up and viscous fingering are at play, and (g-i) a torus with $R_0/a_0 = 3.2$ and $V = 1500$ V that exhibits visous fingering. The dashed circle in (a) represents the outer rim of the torus at t=0; the velocity in this region is $\vec{U}_o$. (j-l) A torus with $R_0/a_0 = 2.0$ and $V = 800$ V, illustrating that some of the initial perturbations do not develop into fingers due to volume conservation. The scale bar in all images correspond to 2mm.

our experiments at constant V by leaving the needle in contact with the toroidal droplet after the formation of the droplet.

For low enough voltage, the torus either shrinks or expands before breaking due to Rayleigh-Plateau instabililities; an example of the latter is shown in Fig. 3.17(a-c) for a torus with an aspect ratio $\xi = R_0/a_0 \approx 3.5$ and at $V = 500$ V. For a similar torus at $V = 800$ V, we observe that the interface distorts, eventually resulting in the formation of fingers; this evolution is exemplified in Fig. 3.17(d-f). At an even higher voltage of $V = 1500$ V, the interface clearly develops initial perturbations in the outer part of the torus, which evolve into a large number of fingers, as shown in Fig. 3.17(g-i). We note that it is not uncommon to observe that some of the initial perturbations do not grow at later stages. This is observed at places that can be far or close to the needle, and that are different for different tori. Hence, despite the fact that the needle could have some local effects in the evolution of the torus, we believe the disappearance of fingers is most likely due to volume conservation. In contrast to experiments with Hele-Shaw cells, where the inner liquid is constantly pumped, our tori contain a fixed volume. As a result, when some of the fingers grow, they consume the available liquid, undermining the growth of nearby fingers; an example of this is shown in Figs. 3.17(j-l). We also note that individual fingers can divide into two fingers, consistent with what is observed in radial Hele-Shaw cell experiments [111] and is highlighted using a dashed circle in Fig. 3.17(i); this is also observed at places that could be close or far from the needle, suggesting once again, that even if the needle can induce local perturbations, it does not affect the overall evolution of the torus. We note, however, that finger division is not frequently observed; we believe this is again due to volume conservation. Note that the shadow seen in all images in Fig. 3.17 is due to the alligator clip used to maintain the metallic needle in place.

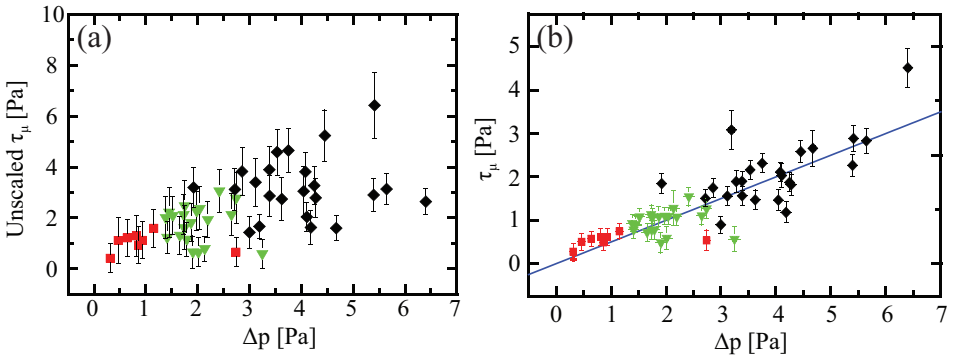

Figure 3.18: The viscous stress, τ_μ, estimated from the drag on a (a) infinite and (b) finite cylinder as a function of the pressure drop at the toroidal interface $\Delta p = p(\theta = \pi) - p(\theta = 0)$. (■) Expanding tori that break; (♦) tori that evolve via viscous fingering instabilities; and (▼) tori that exhibit both breaking and viscous fingering. The line corresponds to $\tau_\mu = (0.49 \pm 0.10)\Delta p$.

3.6.3 Controlling the Rate of Expansion with Applied Voltage

We find that the torus expands faster the higher the applied voltage; this can be seen by visually inspecting Figs. 3.17(b,e,h) and suggests that the speed of expansion affects the appearance of fingers. To determine what sets the expansion speed, we consider the normal stress balance at the interface, which is given by:

$$p(\theta) - p_o = 2\gamma H - \frac{1}{2}\epsilon E^2. \tag{3.37}$$

We can estimate the pressure difference $\Delta p = p(\theta = 0) - p(\theta = \pi)$ along the expansion direction. To estimate U_o, we compare Δp with the viscous stress on a cylinder. From dimensional analysis, we expect that the viscous stress should scale as $\tau_\mu \approx 2\pi\mu_o U_o/\alpha_0$. By plotting τ_μ as a function of Δp, we find that they exhibit a trend, but the data are very scattered [see Fig. 3.18(a)]. However, in this relation we have neglected the fact the geometry of the torus depends on ξ as well. We then consider the viscous stress exerted on a torus as the drag force exerted on a **finite cylinder** with aspect ratio $\xi_c = L/\alpha_0$, where L is the length of the cylinder, that is moving at a speed U_o and oriented perpendicular to the

flow direction, and inside a liquid with viscosity μ_o [112]:

$$\tau_\mu = \frac{2\pi\mu_o U_o}{\alpha_0 \ln(0.83\xi_c)}. \tag{3.38}$$

In our case, we take $\xi_c = \xi$ and $\alpha_0 = a_0$, and obtain τ_μ using equation 3.38. We find that τ_μ is now linear with Δp, as shown in Fig. 3.18(b). Furthermore, the slope of a linear fit to the data is 0.5, and hence, $\tau_\mu \approx 0.5\Delta p$, confirming that the expansion speed, for a torus with a given geometry inside a given outer liquid, can be controlled with Δp, and thus with V.

3.6.4 Determining Transition from Rayleigh-Plateau to Saffman-Taylor Instability

Since, V controls the expansion rate, it also affects the time scale associated with the observation of viscous fingering. If break-up happens before this instability can develop, however, no fingers are observed. To confirm this, we consider the relevant time scales in either case. For break-up, which is essentially due to Rayleigh-Plateau instabilities, we take $t_{R-P} = 2\mu_o a_o/\gamma$, where the prefactor 2 is obtained for the case of $\mu_i/\mu_o << 1$ [16]. For the Saffman-Taylor instability, the relevant time scale is $t_{S-T} = a_o/U_o$ [110], corresponding to the time for the interface of the torus to move its tube radius. Hence, we expect the transition from break-up to viscous fingering to occur when:

$$t_{S-T} < t_{R-P} \Rightarrow Ca = \frac{\mu_o U_o}{\gamma} > 0.5 \tag{3.39}$$

where Ca is a capillary number. Experimentally, we observe the clear development of fingers for $Ca \gtrsim 0.4$, as shown in Fig. 3.19 with a dashed line, which is consistent with our expectations.

We need to note that, this t_{R-P} is set using the growth of the fastest unstable mode, ω_{max}, as $t_{R-P} = 1/\omega_{max}$. Therefore, the presence of charge can affect t_{R-P}, since charge alters the fastest unstable mode. Fig. 3.14 shows the dispersion relation for different values of N_E that correspond to our experiments discussed in Section 3.5.2. We find that even though the

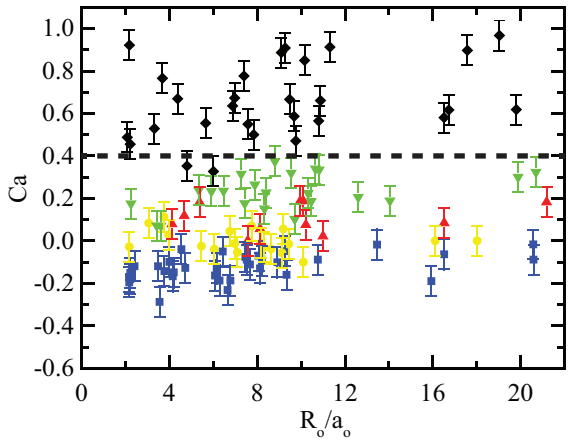

Figure 3.19: State diagram in terms of the capillary number Ca and the aspect ratio R_o/a_o. The symbols represent (■) shrinking tori, (●) tori with stationary central-circle radius, (▲) expanding tori that break, (♦) tori evolvoing via viscous fingering instabilities, and (▼) tori that exhibit both breaking and viscous fingering. The dashed line represents the critical capillary number where only viscous fingering is observed.

fastest unstable mode, $(ka_0)_{max}$, changes with N_E, the corresponding growth rate remains almost constant. As a result, we assume that t_{R-P} remains constant in our experiments.

3.6.5 Comparison to Radial Hele-Shaw Cell

To further confirm that the instability we observe is indeed viscous fingering, we consider the fastest growing mode. Theory has been developed for the case of a radial Hele-Shaw cell [110]. The basic equation that describes the velocity is Darcy's law, which describes the local average velocity in a two dimensional situation. Note that for porous media, this approximation is appropriate since the pore size is small compared with the distance traveled by the fluid through the medium. In the case of a Hele-Shaw cell, the velocity is the average velocity between the parallel plates, which is given by:

$$\boldsymbol{u} = -\frac{b^2}{12\mu}\boldsymbol{\nabla} p, \tag{3.40}$$

where b is the distance between the plates [see Fig. 3.16(c)]. Note that the prefactor $b^2/12$ is intrinsic to this geometry and in general is referred to as the permeability. This

prefactor is derived by calculating the average velocity between two plates for a Poiseuille flow. Returning to the stability analysis, the base solution is obtained by solving equation 3.40 for the velocities of both inner and outer liquids, u_{inner} and u_{outer}, respectively, for an unperturbed interface. This is given by a velocity potential, $\Phi^{(0)}$, as[110]:

$$\Phi_j^{(0)} = -R \cdot U \left[\ln\left(\frac{r}{R}\right) + \frac{\mu_2}{\mu_j} \right], \tag{3.41}$$

where r is the radius from the center of the Hele-Shaw cell, and $j = 1$ or 2 corresponds to the solution for the inner and outer liquids, respectively [see Fig. 3.16(c)]. The velocity is calculated from the potential as $\vec{v} = \nabla\Phi^{(0)}$. The boundary conditions at the interface are:

$$u_{inner} = u_{outer} \tag{3.42}$$

$$p_{inner} - p_{outer} = 2\gamma H, \tag{3.43}$$

which correspond to the kinematic boundary condition and the normal stress balance, respectively. The interface is then sinusoidally perturbed using a number n of wavelengths as:

$$\rho = R + \delta\, f(t) e^{in\phi}, \tag{3.44}$$

where ρ is the perturbed radius of the interface, δ the amplitude of the perturbation at $t = 0$, and $f(t)$ a function of time showing how fast the perturbation grows. The value of n determines the number of fingers that develop and corresponds to the different modes in the problem. By solving the perturbed velocity using equation 3.40 subjected to the same boundary conditions, a differential equation describing $f(t)$ for each n can be obtained [110]. By imposing $df/dt = 0$, we are considering the mode that grows the fastest; the value of n for this mode is n_m. Note this mode is associated with the n most likely seen

experimentally. It is given by [110, 113]:

$$n_m = \sqrt{\frac{1}{3}\left(\frac{12\mu_o}{\gamma}\frac{UR^2}{b^2} + 1\right)} \tag{3.45}$$

where U is the velocity of the interface, and R the radius of the stable circle before any fingers develop [see Fig. 3.16(c)]. To compare with our experimental results, we consider $U = U_o$, $R = R_0 + a_0$ and $b = 2a_0$. This results in equation 3.45 taking the form:

$$n_m = \sqrt{\frac{1}{3}\left(\frac{12\mu_o}{\gamma}\left[U_o\left(\frac{\xi+1}{2}\right)^2\right] + 1\right)}. \tag{3.46}$$

Since the theory is a linear stability analysis, the validity of the result is restricted to the early stages of the instability, where the perturbations are still small. We therefore measure n_m right after the perturbations in the outer part of the torus become apparent [see Fig. 3.17(k)], and plot n_m as a function of $U_o\,[(\xi+1)/2]^2$. We find that the number of fingers grows as $U_o\,[(\xi+1)/2]^2$ increases, as shown in Fig. 3.20 and consistent with what is expected from equation 3.46. By performing a non-linear least squares fit of the data to equation $n_m = \sqrt{\frac{1}{3}\,(A\,U_o\,[(\xi+1)/2]^2 + B)}$, where A and B are fitting parameters, we obtain $A = (6.2\pm0.2)\cdot10^6$ s/m and $B = 190\pm70$. The fit correctly describes the data, as shown with a continuous line in Fig. 3.20. Furthermore, from the values of μ_o and γ in our experiments, we find $A = \frac{12\mu_o}{\gamma} = (2.1 \pm 0.3)\cdot 10^6$ s/m, which is comparable to the value of A obtained from the fit. We do not expect perfect agreement since $12\mu_o/\gamma$ is a specific value for a Hele-Shaw cell, while we are considering a toroidal droplet expanding in an unbounded space. Since the error in B is large, we cannot conclude anything meaningful from the behavior of n_m for low $U_o\,[(\xi+1)/2]^2$. Indeed, enforcing $B = 1$ and leaving A as the only fitting parameter, we see that the fit still qualitatively describes the data, as shown with a dashed line in Fig. 3.20, with $A = (8.3 \pm 0.6)\cdot 10^6$ s/m, which is not far from our previous result. This selection of $B = 1$, however, results in a non-integer n_m, further reflecting the innacuracy of the analytical treatment for low values of $U_o\,[(\xi+1)/2]^2$.

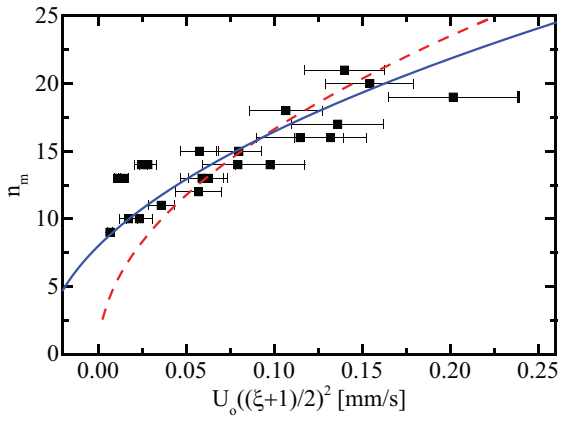

Figure 3.20: Plot of the number of perturbations, n_m, in the early stages of evolution, as illustrated in Fig. 3.17(k), as a function of $U_o\,[(\xi+1)/2]^2$. The continuous line is a non-linear least squares fit to the data according to equation $n_m = \sqrt{\frac{1}{3}\,(A\,U_o\,[(\xi+1)/2]^2 + B)}$, where A and B are fitting parameters. The dashed line is a similar fit with $B = 1$ and A as the only fitting parameter.

Thus, our data conform to the functional form prescribed by equation 3.46 despite the different geometry in our problem and the fact that we did not explicitly account for the presence of charge on the toroidal surface. This suggests that the key to our results is the quasi-two dimensional flow that results from the uneven charge density distribution on the torus, further supporting the idea that the main role of the charge is to set the value of U_o, which is ultimately the quantity that enters in the theoretical treatment of the radial Hele-Shaw cell. However, explicitly performing the linear stability analysis of the full problem, considering both the presence of surface charge and the toroidal geometry of our experiments, would provide a more accurate analysis of the experimental situation. Our analysis, nevertheless, captures the essential aspects of our observations.

3.6.6 Charged Toroidal Droplets and the Rayleigh Limit

An important concept we need to address in our experiments, since we are dealing with charged droplets, is the so-called Rayleigh limit. This limit is related to the maximum amount of charge a spherical droplet can hold before deforming. The Rayleigh limit is calculated by finding the charge density needed to balance electric and surface tension

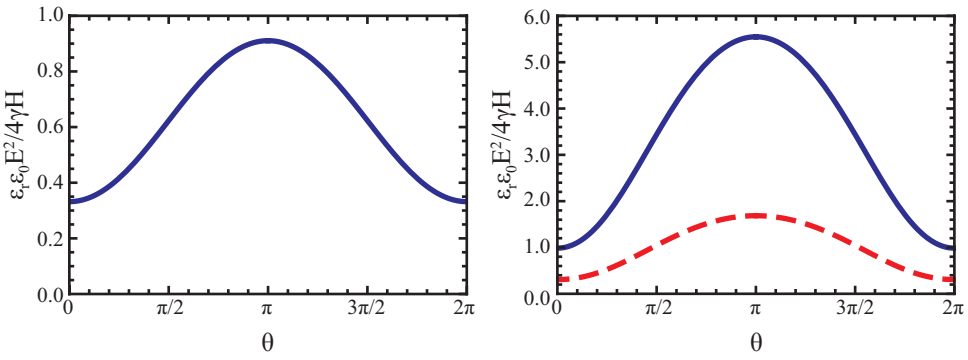

Figure 3.21: Plot of the number of perturbations, n_m, in the early stages of evolution, as illustrated in Fig. 3.17(k), as a function of $U_o\ [(\xi + 1)/2]^2$. The continuous line is a non-linear least squares fit to the data according to equation $n_m = \sqrt{\frac{1}{3}\left(A\ U_o\ [(\xi + 1)/2]^2 + B\right)}$, where A and B are fitting parameters. The dashed line is a similar fit with $B = 1$ and A as the only fitting parameter.

stresses for a spherical droplet with radius r: $\frac{1}{2}\epsilon_r\epsilon_0 E^2 = \frac{\gamma}{r}$. Using $E = \frac{Q}{4\pi\epsilon_r\epsilon_0 r}$, we obtain:

$$Q_{R.L.} = 8\pi\left(\epsilon_r\epsilon_0\gamma r^3\right)^{\frac{1}{2}}. \tag{3.47}$$

We see that for larger γ and larger r, a spherical droplet can hold more charge while remaining spherical. For toroidal droplets, the charge density and mean curvature vary around the torus, and more importantly, they vary in a way that unables the balance of the two stresses. As a result, it is impossible to assign a Rayleigh limit for a toroidal droplet. Instead, we calculate a local ratio of the electric to surface tension stresses for some of our experiments. Fig. 3.21(a) shows the ratio of $\frac{1}{2}\epsilon_r\epsilon_0 E^2$ to $2\gamma H$ as a function of θ for an experiment where we observe fingers. We find that the electric stresses are always smaller than the surface tension stresses, and hence that we are below the local Rayleigh limit for toroidal droplets. This confirms that our observation of viscous fingering do not rely on our drops locally violating the Rayleigh limit.

We plot the same quantity for another experiment where we also see that exhibits fingers, but at higher voltage than before [see solid line in Fig. 3.21(b)]. In this case, we find that indeed we are above this local Rayleigh limit we have defined. This, however, does

not imply we are truly above the equivalent Rayleigh limit for spheres, since we know that our droplets in these conditions deviate from the toroidal shape appreciably. In particular, the torus flattens as we have seen in Section 3.4, which in turn will change the geometry and increase the surface area. As a result, the capacitance can potentially increase, and the surface tension stresses will increase since the curvature also increases.

As an estimate, let us assume that a_0 doubles in size, while the inner radius $(R_0 - a_0)$ remains the same. As a result the effective radii are $R_{eff} = R_0 + a_0$, and $a_{eff} = 2a_0$, and the effective aspect ratio is $\xi_{eff} = (\xi + 1)/2$. The surface area also increases, and we estimate the new area as an annulus between $R_{eff} - a_{eff}$ and $R_{eff} + a_{eff}$, which results to an area of $8\pi R_{eff} a_{eff}$. We then estimate the decrease in the surface charge density according to the change in surface area. Finally, assuming that the cross section remains an ellipse, the minimum radius of curvature (corresponding to the maximum curvature) is given by $a_0/2$. By including all these, we can estimate a new Rayleigh limit, as shown by the dashed line in Fig. 3.21(b). We find that by including these estimates, we find that some regions of the torus are above the Rayleigh limit. This estimation shows that the torus can redistribute the charge by becoming flatter and hold more charge instead of expelling it. This allows us to conclude that the change of the shape of the torus as it evolves can accommodate more charge on its surface, which enables neglecting a dominant role related to the Rayleigh limit.

3.7 Conclusions

We have shown that charge can qualitatively change the behavior seen for neutral toroidal droplets and cause the expansion of the droplet rather than its shrinkage. We account for the expansion with a simple model considering the pressure drop across a charged toroidal interface. It is the competition between surface tension stresses and the electrical stresses that determines whether a toroidal droplet shrinks or expands. The model treats the torus as electrostatically equilibrated, which is consistent with the fact that the electrical relaxation

time is small compared to the characteristic time scale associated to the droplet evolution. This indicates the torus is equipotential. Additionally, and also in contrast to what is seen for neutral toroidal droplets, charged droplets almost always end up breaking via Rayleigh-Plateau instabilities, appropriately modified to account for the presence of charge. Since in the thin torus limit, we can correctly think of a toroidal droplet as approaching the cylindrical limit, slender electrified toroidal droplets can be seen as a model system with which to test instability theories for electrified jets. In this sense, charged toroidal droplets are advantageous compared to jets in electrospray, as these last ones are typically non-equipotential and have surface charge densities that, as a result, are hard to control and quantify.

We have also shown that the geometry of a charged toroidal droplet can result in a steady quasi-two dimensional expansion that precedes the formation of viscous fingering. This illustrates that it is possible for Saffman-Taylor instabilities, which most commonly occur in confined flows when a fluid displaces another more viscous fluid, can develop in a three-dimensional setting. In our experiments, it is the uneven surface charge density between the inside and outside regions of the torus that ultimately enables the formation of fingers. This instability is in direct competition with the Rayleigh-Plateau instability, which would cause the torus to break. As a result, the instability that grows the fastest is the one that determines the fate of the toroidal drop. By controlling the expansion speed with the applied voltage, we are able to decrease the time scale associated with viscous fingering so that it is the viscous fingering instability what controls the evolution of the torus. The number of fingers in the experiments qualitatively follows the expected number of fingers obtained from linear stability analysis in radial Hele-Shaw cells, supporting the conclusion that our observations are related to Saffman-Taylor instabilities. Furthermore, this qualitative agreement suggests that the charge mostly sets the expansion speed, without qualitatively affecting the properties of the growing fingers. However, more detailed theoretical calculations are needed to fully obtain a detailed picture of the problem. Most importantly, the breaking of axisymmetry in a torus is key to our observations, suggesting

that similar behavior is also possible in situations where due to the three-dimensional character of the flows, viscous fingering would not be anticipated. This could potentially extend the relevance of this instability to situations other than two phase flows in porous media, which is perhaps where it is currently of most importance.

We believe our results open the way to additional work in electrohydrodynamics using toroidal droplets as a novel platform. Additionally, there is still ample room for theory to be developed where all the effects in our experiments are accounted for. For example, for the breakup of charged toroidal droplets, and for viscous fingering in charged toroidal droplets, the current theories do not include the effects of the electric stresses nor the effect of the toroidal geometry. In addition, it might be necessary for more complex approaches to fully understand the problem, by including the coupling between the flow field, shape, and electrostatics.

CHAPTER 4

BREAKUP OF LIQUID TORI IN A SHEAR-THINNING FLUID

4.1 Introduction

The research presented so far has been focused on the evolution of toroidal droplets consisting of pure Newtonian fluids. A Newtonian fluid is a fluid for which the viscous stress, τ, is linearly proportional to the local strain rate, $\dot{\varepsilon}$, with the viscosity, μ, as the proportionality constant, i.e. $\tau = \mu\dot{\varepsilon}$. The Navier-Stokes equations used so far were derived assuming a Newtonian liquid.

However, there are fluids that are non-Newtonian. In this case, the viscosity is a function of $\dot{\varepsilon}$: $\mu = \mu(\dot{\varepsilon})$. If $\mu(\dot{\varepsilon})$ is an increasing function of $\dot{\varepsilon}$, the fluid is called a shear-thickening fluid. Corn starch in water, for example, is a shear-thickening fluid. In contrast, if $\mu(\dot{\varepsilon})$ is a decreasing function of $\dot{\varepsilon}$, the fluid is called a shear-thinning fluid; ketchup and molasses are shear-thinning fluids; they move slowly in the bottle but spread easily when sheared. We expect that this non-linear behavior will affect the breakup dynamics.

Recall, that we discussed the dispersion relation in the case of two viscous Newtonian fluids in Section 3.5.1. There, we can see that the fastest unstable mode changes from $(k\alpha_0)_{max} \approx 0.13$ in the case of $\beta = 10^3$ to $(k\alpha_0)_{max} \approx 0.25$ in the case of $\beta = 10^{-3}$. In addition, by calculating the growth rates of the fastest unstable mode in both case, we find that the growth rate for $\beta = 10^3$ is almost three times higher compared to $\beta = 10^{-3}$. As a result, a simple exchange of liquids, even for Newtonian fluids, is not symmetric about $\beta = 1$ and can alter significantly the breakup dynamics.

The breakup dynamics of non-Newtonian liquids has been studied both for liquid jets [34, 55–65], and for liquid bridges [40–54], only in the case where the inner fluid is non-Newtonian. However, as far as we are aware, the inverse problem of the breakup of New-

tonian jets surrounded by a non-Newtonian fluid has not been studied. Based on the results on fluid exchange with Newtonian liquids, this is fundamentally important.

Here, we first discuss research performed in collaboration with Procter & Gamble, where our work on the breakup of Newtonian jets in non-Newtonian liquids began. We will then address the problem using toroidal droplets. Our main result is that one can use the linear theory to understand the breakup dynamics inside non-Newtonian liquids by incorporating the non-linearity of the outside medium via the strain-rate dependent viscosity.

4.2 Initial Motivation: Making Drops for P&G

We collaborated with Procter and Gamble (P&G) to produce droplets made of a P&G liquid-like material in a polymer liquid. To do this, we use a glass-based microfluidic setup. The liquids are poly-ethylene glycol (PEG) of average molecular weight 8000 (outer liquid) and Magnasoft (inner liquid). We note our PEG is solid at room temperature and melts at about 60 °C [114]. Our experiments are done at $T = 68-70$ °C. Magnasoft is a proprietary material by P&G that is silicone oil based. The known viscosities of the liquids are $\mu_i \approx 1.5$ Pa·s (from P&G) and $\mu_o \approx 2$ Pa·s right above the melting temperature (from Ref. [114]).

The idea is to produce the droplets at a temperature where the PEG is liquid in the device and solidifies as soon as it exits the microfluidic device. Thus, the emulsion of Magnasoft in PEG can be sent via mail easily to P&G. Since PEG is miscible with water, adding water will dissolve the PEG and make the Magnasoft emulsion accessible to P&G scientists.

4.2.1 Microfluidic Setup

Microfluidic Device

To generate droplets, we use a glass-based microfluidic device [74], consisting of an outer capillary with a square cross section of inner side l and a cylindrical capillary with a circular cross section of outer diameter equal to l, as defined in Fig. 4.1(a). This capillary is pulled

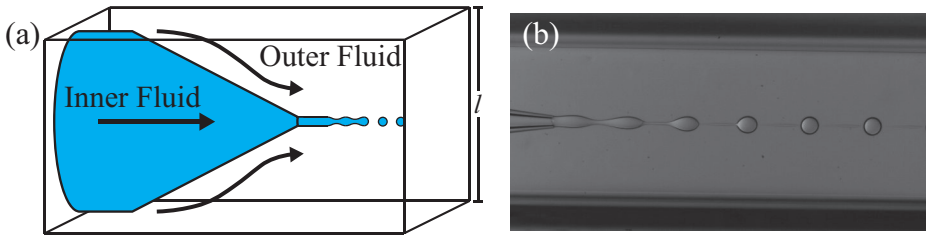

Figure 4.1: (a) Schematic of a co-flow microfluidic device with a pulled capillary with a cylindrical cross-section insde a capillary with a square cross section of side l. (b) An experiment with glycerol and 1,000 cSt silicone oil for inner and outer liquids, respectrively.

to make a tip at one of its end with typical diameter of $\sim 20\,\mu$m, and introduced in the other capillary, as shown in Fig. 4.1(a). We pump the inner liquid (dispersed phase) through the cylindrical capillary and the outer liquid (continuous phase) through the gaps between the circular and square cross section of the capillaries [see Fig. 4.1(a)]. The inner liquid can either drip at the tip or form a jet. In the later case, the jet breaks into droplets due to Rayleigh-Plateau instabilities. The transition between the two regimes is controlled by the capillary number of the continuous phase, Ca_o [74], which is given by:

$$Ca_o = \frac{\mu_o U}{\gamma}, \tag{4.1}$$

where μ_o is the viscosity of the continuous phase, U the typical speed of the fluid, and γ the interfacial tension. For $Ca_o < 1$, the viscous stresses are not strong enough to deform the spherical droplet and form a jet, and thus, the inner liquid drips at the tip. In contrast, for $Ca_o > 1$, the viscous stresses are able to induce the formation of a jet. Since in our experiments, μ_o is high, the typical flow rates needed to form a jet, corresponding to $Ca_o > 1$ are not high. However, also due to the large μ_o, the pressure drop across the microfluidic device is high and, thus, large forces are needed to pump the continuous phase. From Poiseuille flow, we know that the pressure drop scales as $\Delta P \sim 1/l^4$. To reduce the amount of force needed to pump the PEG, we use capillaries (VitroCom) with the largest available l, which is $l = 2$ mm.

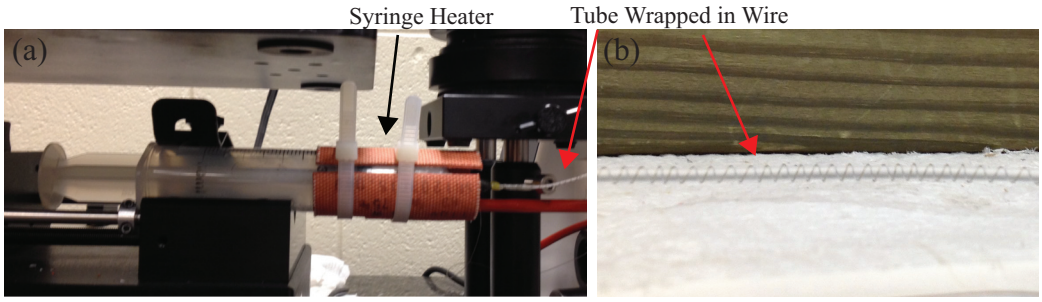

Figure 4.2: (a) A 60 mL syringe wrapped with the heating pad, mounted on a Harvard Apparatus syringe pump. (b) Plastic tubing wrapped with a metallic wire of total resistance $R = 0.1\ \Omega$. A voltage is applied through the wire using a small voltage/high current power supply.

Syringe heater

To maintain a high temperature inside the syringe, we use a syringe heater (New Era) consisting of a heater control unit, which allows control of the temperature with sensitivity $\pm$ 0.1 °C, and a heating pad that is wrapped around the syringe. Prior to any experiment, we determined the maximum temperature our syringes, which are made of polycarbonate, can withstand. We find that at 88 °C, the syringe softens and melts. As a result, we always kept the temperature of the syringe between 80 and 85 °C. We heated the syringe with the PEG 8000 for about 25-35 minutes before any experiment to assure that the PEG is thoroughly melted, and that all of the trapped air is eliminated. An image of the syringe containing the PEG 8000 and surrounded by the heating pad is shown in Fig. 4.2(a).

Pumping through the tubing

The biggest challenge is to be able to pump the continuous phase through the tubing that connects the syringe to the microfluidic device, as PEG typically solidifies very soon after it gets out of the syringe and into the tubing. Hence, we need to keep the tubing warm enough to allow for proper flow. This was achieved by wrapping the tubing with metallic wire in a helical form with a pitch of $\sim$ 1 mm [see Fig. 4.2(b)]. The wires used were measured to have a resistance of 0.1 Ohms. A low voltage-high current power supply was

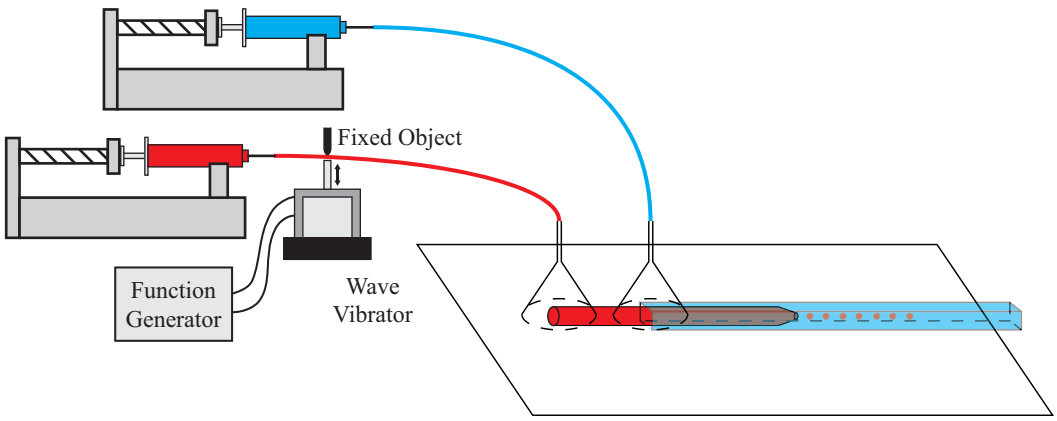

Figure 4.3: A schematic showing the application of a pressure perturbation in the inner liquid using a wave vibrator. The wave vibrator squeezes the tube carrying the inner liquid as it oscillates using a fixed object. The oscillation frequency and amplitude is controlled using a function generator.

then used to pass current through the wire. Due to Joule heating, the wire warms up. The typical current needed to melt the PEG inside the tubing is about $I \approx 3.6$ A.

Heating the device

In addition to the syringe and tubing, the microfluidic device itself needs to be kept at high enough temperature to keep the PEG in its liquid phase. This is done using a heavy duty heat gun in combination with a contained structure built from cardboard. The containment box has holes to let air in and out as well as to let the light from the microscope to properly pass. An image of the experimental setup can be seen in Fig. 4.4. A thermocouple is used to measure the temperature inside the box during the experiment.

Inducing Pressure Perturbations

We have already mentioned that jets typically break via the fastest unstable mode [see Chapter 3.5.1]. This implies that we do not have control over the size of the resultant droplets after the formation of the jet. We note that in co-flow devices, like our setup, the natural way to change the drop size is by changing the flow rate of the continous phase.

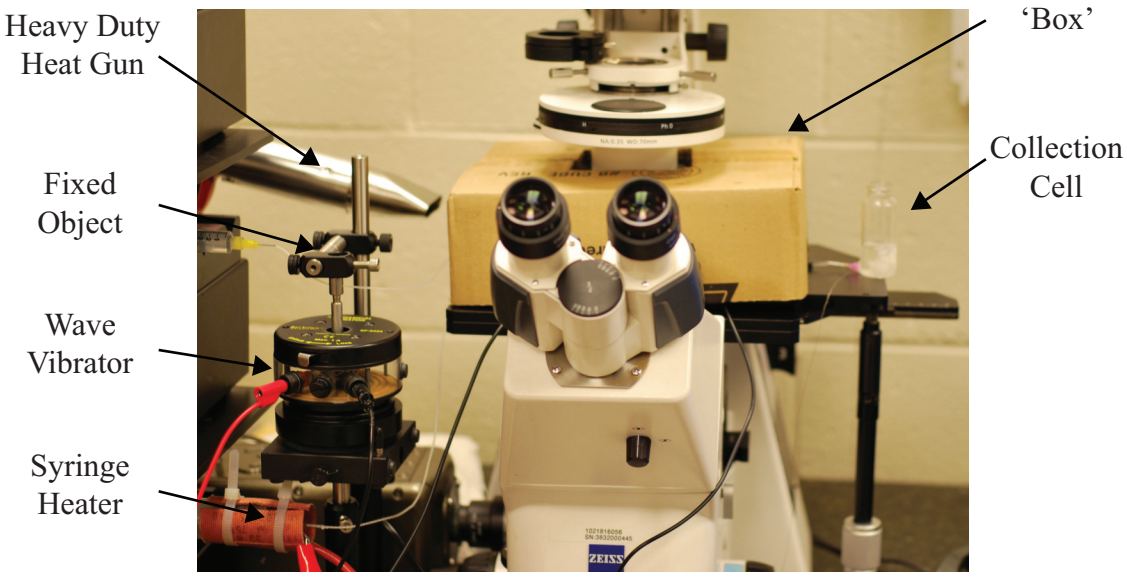

Figure 4.4: The final setup. The outer liquid is kept warm with a syringe heater, while the tube is kept warm by flowing electric curent through the mettalic wire that is wrapped around trhe tube. A mechanical perrtubation is applied in the inner liquid using the wave vibrator and a fixed object. The device is kept warm using a heavy duty heat gun and the hot air is confined around the device uasing a modified cardbox. We collect the product in a vial that is kept warm due to the hot air current coming out of the box.

In our case, due to μ_o being so large, the range of speeds we can achieve are limited. In addition, equilibration times are very long making the process rather ineffective. Hence, to change the size of the droplets, we imposed an external perturbation to excite modes other than the fastest unstable mode. We follow the procedure descirbed in prior work [115, 116].

We induce pressure perturbations using a mechanical wave vibrator (PASCO scientific, SF-9324). The plastic tubing carrying the inner fluid is placed between the wave driver and a fixed object. As the wave driver oscillates, the tubing is periodically squished against the fixed object. The mechanical wave vibrator is controlled using a function generator (SRS, DS345), which allows to freely change the frequency, shape, and amplitude of the mechanical vibrator [see Fig. 4.3 for a schematic and Fig. 4.4 for the experimental setup].

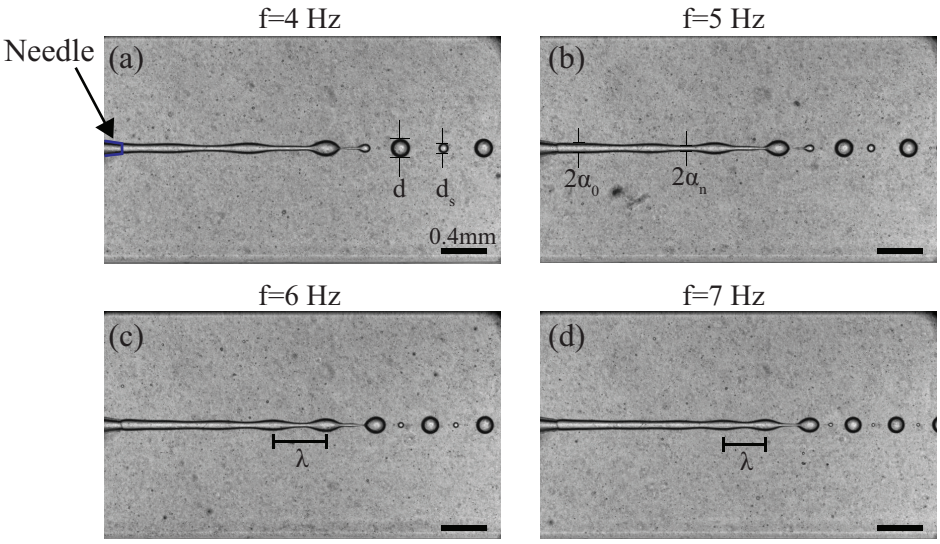

Figure 4.5: Jet breakup in a co-flow microfluidic device using Magnasoft and PEG 8000 for the inner and outer liquid, respsectively. The inner and outer flow rates are Q_{in} = 0.5 mL/hr, and Q_{out} = 40 mL/hr, respectively, while the applied perturbation has a frequency of (a) f = 4 Hz, (b) f = 5 Hz, (c) f = 6 Hz, and (d) f = 7 Hz. We measure the wavelength of the perturbation, λ, the initial unpeturbed radius α_0, and the evolution of the neck radius, α_n.

4.2.2 Experimental Results

In our experiments, the flow rates of the inner and outer liquids are fixed to Q_{in} = 0.5 mL/hr and Q_{out} = 40 mL/hr, respectively, and we apply pressure perturbations with different frequencies. The disturbance on the jets are well defined and cause breakup into droplets with a well defined diameter, as shown in Fig. 4.5(a-d). In addition, it is clear from the figure that the wavelength of the perturbation decreases with increasing frequency. Interestingly, the satellite droplets also decrease in size; these droplets are formed from secondary breakup of the transient jet produced between the main droplets.

From these images, we can extract the wavelength of the instability, λ, and the main and satellite droplet diameter, d and d_s. We record a video of the breakup process over a few seconds, and measure these quantities over 10-15 breakups. Table 4.1 summarizes the results from these experiments. From λ and f, we calculate the propagation speed of the wave. We find that it is a approximately constant and equal to the average speed of

Table 4.1: A table showing the applied frequencies f, and the measured λ, d, and d_s for the pressure perturbation of a Magnasoft jet in melted PEG 8000.

f	λ	$U_{jet} = f \cdot \lambda$	d	d_s
4.000 Hz	(660 ± 20) μm	(2.64 ± 0.08) mm/s	(180 ± 10) μm	(100 ± 10) μm
5.000 Hz	(570 ± 20) μm	(2.9 ± 0.1) mm/s	(170 ± 10) μm	(80 ± 10) μm
6.000 Hz	(470 ± 20) μm	(2.8 ± 0.1) mm/s	(160 ± 10) μm	(60 ± 10) μm
7.000 Hz	(380 ± 20) μm	(2.7 ± 0.1) mm/s	(150 ± 10) μm	(30 ± 10) μm

the inner liquid, which we calculate from the flow rate and the cross sectional area of the jet: $Q_{in}/\pi\alpha_0^2 \approx 2.7$ mm/s. This confirms that the perturbations induced by our vibrator are convected downstream where they induce breakup of the jet. We, thus, believe that the droplets are formed due to convective Rayleigh-Plateau instabilities [117]. This would imply that the complex liquids we are using behave as simple liquids on the timescale associated to breaking. To address whether this is true, we perform rheology.

4.2.3 Rheology of the Materials

We use shear rheology to quantify the mechanical properties of the materials (see Appendix D.3). We used is a cone-plate tool with a diameter of 25 mm and an angle of 2.014^o. The preshear protocol used for both materials is a constant shear rate of $\dot{\varepsilon} = 20$ s^{-1} for 15 minutes followed by a 15 minute time sweep in order to ensure that the system does not evolve over time. For PEG 8000, we fixed the temperature to 70 °C, while for Magnasoft, we fixed the temperature to 60 °C. From the oscillatory rheology in the linear regime, we find that both materials are predominantly viscous, with $G'' > G'$ [see Fig. 4.6(a)]. Furthermore, G'' is linear with ω. This linearity is characteristic of simple liquids with proportionality constant the viscosity. A linear fit of the data gives a value of $\mu = (1.66 \pm 0.01)$ Pa·s for PEG 800, and $\mu = (1.26 \pm 0.01)$ Pa·s for Magnasoft.

In addition, we perform steady state rheology where we apply a stress and measure the strain rate. For Magnasoft, τ is linear with $\dot{\varepsilon}$ [see Fig. 4.6(b)], consistent with simple liquid behavior, where the proportionality constant is again the viscosity. From a linear fit to the data, we find $\mu = (1.348 \pm 0.001)$ Pa·s, consistent with the value obtained using

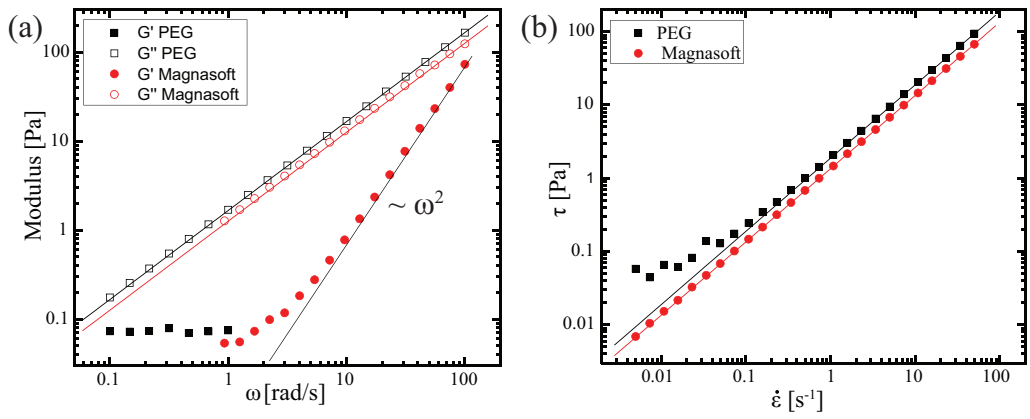

Figure 4.6: (a) Oscillatory rheology of PEG 8000 (squares) and Magnasoft (circles) using a strain of $\varepsilon = 0.01$. For both materials G'' is linear with ω as expected for a simple liquid. For Magnasoft, we observe that $G' \propto \omega^2$ as expected for Maxwell's model at low frequencies. For PEG, we do not have the resolution to measure G' for $\omega > 1$ rad/s. (b) The steady state rheology of PEG 8000 (squares) and Magnasoft (circles). The lines correspond to the linear fit to extract the corresponding viscosities.

oscillatory rheology and the value provided by P&G. For PEG 8000, we obtain that τ is linear with $\dot{\varepsilon}$ for sufficiently high $\dot{\varepsilon}$, as shown in Fig. 4.6(b). From this region, we obtain $\mu = (1.884 \pm 0.001)$ Pa·s. Note, however, that for low $\dot{\varepsilon}$, τ seems to plateau, indicative of a possible influence from solid-like contributions to the rheology. Note also that in the linear oscillatory rheology, we found an appreciable contribution from G' at the lowest frequencies. However, for low ω in the oscillatory rheology, and low $\dot{\varepsilon}$, in the steady state rheology, the measured values approach the minimum torque that the rheometer can measure. As a result, it is hard to conclude anything definitive about these solid-like contributions. This behavior could also results from the proximity to the melting temperature; even if the manufacturer reported a melting temperature of 60 °C, our controls indicate that most likely is closer to 65 °C.

The rheology indicates that for the characteristic times involved in the breakup experiments, our materials exhibit Newtonian behavior. As a result, the breakup process should be similar to the breakup process of cylindrical jets made of a simple liquid inside another, immiscible simple liquid.

Table 4.2: The measured growth rate, ν, and mode, $k\alpha_0$, for experiments with different frequencies. We report the expected dimensionless growth rate $\nu\frac{\mu_o\alpha_o}{\gamma}$ as expected from Tomotika [16] for the measured $k\alpha_0$. By comparing with the measured ν, we find the corresponding value of μ_o/γ.

ν	$k\alpha_0$	$\nu\frac{\mu_o\alpha_o}{\gamma}$	$\frac{\mu_o}{\gamma}$
(13 ± 1) s^{-1}	0.32 ± 0.03	0.028	(58 ± 9) s/m
(22 ± 2) s^{-1}	0.39 ± 0.04	0.034	(170 ± 30) s/m
(41 ± 5) s^{-1}	0.39 ± 0.04	0.034	(90 ± 10) s/m
(32 ± 3) s^{-1}	0.51 ± 0.05	0.040	(32 ± 8) s/m
(25 ± 3) s^{-1}	0.51 ± 0.05	0.040	(40 ± 8) s/m
(18 ± 2) s^{-1}	0.55 ± 0.05	0.041	(70 ± 10) s/m

4.2.4 Comparison with Tomotika

To confirm this, we use Tomotika's analysis for the breakup of viscous jets [see Chapter 3.5.1]. We define the neck of the jet to be the region with the smallest radius. We refer to this radius as a_n [see Fig. 4.5(b)]. In linear stability analysis [16],

$$a_n = a_0 - \epsilon e^{\nu t}, \tag{4.2}$$

where ν is the growth rate. We can calculate ν in our experiments by monitoring how a_n changes with time; we do this for different frequencies of the pressure waves, which correspond to different λ. We summarize the result for ν and $k\alpha_0$ in Table 4.2.

Using the viscosities obtained from averaging the viscosities measured in oscillatory and steady state rheology, $\mu_i = (1.30 \pm 0.01)$ Pa·s and $\mu_o = (1.77 \pm 0.01)$ Pa·s, we can theoretically calculate the dimensionless growth rate expected for the experimental values of $k\alpha_0$ [see Table 4.2]. We cannot measure γ using the pendant drop method, because of the difficulty of keeping PEG melted. However, we expect the value to be around $\gamma \approx 30$ mN/m [118]. We then calculate the value of μ_o/γ for the experimental dimensionless growth rate by matching it with the theoretical expectations of Tomotika [see Table 4.2]. We find $\mu_o/\gamma = (80 \pm 45)$ s/m in the range of $0.3 < k\alpha_0 < 0.6$, which is consistent with the ratio of $\mu_o/\gamma = 59$ s/m expected for our system.

Using these experimental procedures and understanding, we generated droplets for P&G with different sizes. Once the emulsion was made, the PEG 8000 solidified with the Magnasoft droplets embedded inside the PEG. These pellets were then shipped to P&G where they were melted to recover the Magnasoft droplets. Those Magnasoft droplets were then used for internal P&G studies.

4.3 Behavior with non-Newtonian Materials

4.3.1 Motivation

In the experiments in collaboration with P&G, the outer liquid behaved as a Newtonian fluid, even though PEG 8000 has some viscoelastic response. This raised the question of how the behavior would change if the outer liquid used is non-Newtonian. There has been prior work on the breakup of non-Newtonian jets inside Newtonian liquids. Specifically, for a jet made of a shear-thinning fluid, the breakup dynamics are much more abrupt compared to the case of a Newtonian fluid [39]. The breakup dynamics change even more when considering a jet of a viscoelastic fluid. In this case, the elasticity of the fluid significantly slows down the breakup of the jet, resulting in the beads-on-a-string configuration, where droplets are connected by transient jets that break over long periods of time [34, 36, 37].

However, the inverse case of the breakup of Newtonian jets in a non-Newtonian medium has not been studied. We know from looking at simple fluids that exchanging the inner and outer fluids does not yield a symmetric result in the growth rates or associated dimensionless wavenumbers. Thus, the existing work on non-Newtonian jets in a Newtonian liquid cannot a priori be used to understand the inverse problem. Here, we explicitly address this using an outside shear-thinning fluid.

4.3.2 Some Theoretical Remarks

In Chapter 3.5.1, we talked about how linear stability analysis is used to extract the dispersion relation for a liquid jet and, in particular, to obtain the fastest unstable mode. From the

stability analysis, we found that a perturbation grows exponentially as:

$$\alpha = \alpha_0 + \epsilon e^{\nu t + ikz}. \tag{4.3}$$

However, this expression is only valid for small perturbations. When the perturbation, $\epsilon e^{\nu t+ikz}$, is comparable to the radius of the jet α_0, linear stability analysis is not valid anymore. In the Stokes regime, where the non-linear convective term in the Navier-Stokes equations is absent, the validity of the linear regime can persist for longer times. However, since the calculation of the perturbed area and curvature of the jet involve non-linear equations, this extension is limited. Fortunately, similarity solutions have been derived to describe the breakup of a jet at large deformation. In the case of a Newtonian jet, for low Reynolds number and large deformations, the neck radius decreases linearly with time [119]:

$$\frac{\alpha_n}{\alpha_0} = \frac{1}{14.1\alpha_0}\frac{\gamma}{\mu}(t_c - t), \tag{4.4}$$

where t_c is the breakup time. Hence, for a Newtonian liquid, the perturbation initially grows exponentially and later becomes linear with time.

Non-Newtonian fluids, either shear-thickening or shear-thinning, can often be described as power-law fluids. A power-law fluid has a constitutive equation that is given by:

$$\tau_{pl} = K\dot{\varepsilon}^{\,n}, \tag{4.5}$$

where τ_{pl} is the viscous stress of a power-law fluid, and K and n are constants. For $n = 1$, the fluid is Newtonian and $K = \mu$. For $n > 1$, the fluid is a shear-thickinning fluid, while for $n < 1$, it is a shear-thinning fluid. In this case, the similarity solution for large deformations is [39, 62]:

$$\frac{\alpha_n}{\alpha_0} = \Phi(n)\frac{\gamma}{K}(t_c - t)^n, \tag{4.6}$$

where $\Phi(n)$ is a pre-factor that depends on the power n. Note that this equations reverts to

equation 4.4 for $n = 1$.

A simple model to describe the behavior of a viscoelastic fluid is Maxwell's model; it considers that the material response can be represented by a Newtonian viscous damper in series with an ideal elastic spring. The stress response of the viscous damper is given by $\sigma_V = \mu\dot{\varepsilon}_V$, where ε_V is the associated strain. For the stress response of the elastic spring, we have $\sigma_E = G\varepsilon_E$, where ε_E is the associated strain, and G is the elastic modulus of the spring. Since the two are attached in series, the total strain exerted will be the sum of the viscous and elastic strains, while the total stress will be the same [120]: $\sigma = \sigma_E = \sigma_V$ and $\varepsilon = \varepsilon_E + \varepsilon_V$. Using this model, the response to a step strain consists of an abrupt jump in stress due to the elastic response of the spring, that decays exponentially in time as $e^{-t\lambda}$ with $\lambda = \mu/G$; this time corresponds to the relaxation time of the materials associated with the long-time fluid flow behavior.

For a jet consisting of a Maxwell fluid, the break-up dynamics for large deformations results from the balance between elastic and capillary stresses. In this case the similarity solution gives [121]:

$$\frac{\alpha_n}{\alpha_0} = \left(\frac{G}{\sigma/\alpha_0}\right)^{1/3} e^{-\frac{t}{3\lambda}}. \tag{4.7}$$

The exponential decay illustrates that the dynamics of a jet consisting of a viscoelastic fluid slows down very close to pinch-off; this prolongs the breakup of the jet, explaining the formation of the beads-on-a-string configurations observed experimentally.

4.4 Preparation and Properties of Carbopol Mixtures

4.4.1 Sample Preparation Method

To study how a non-Newtonian fluid affects the breakup of a Newtonian jet, we use Carbopol mixtures as the continuous phase. Carbopol (Lubrizol) consists of ionic granular-sized hydrogels made of poly(acrylic acid) (PAA). In water and at neutral pH, the PAA is negatively charged and the particles are highly swollen [122].

To prepare the Carbopol mixtures, we first prepare the acqueous solution that we use to swell the PAA hydrogels [123]. This solution is a mixture of water, glycerol and ethanol. Glycerol is used to increase the viscosity of the solution, while ethanol decreases surface tension [124]. We then dissolve Carbopol (ETD 2020, Lubrizol), in the aqueous mixture. At this point, the mixture has a low pH of $\sim$ 3.5 due to the ionization equilibrium of the PAA hydrogels, and hence the hydrogels are not swollen; in this state, the mixture is milky with appreciable scattering. The mixture is left overnight to allow time for the hydrogels to reach their equilibrium size in these conditions. The mixture is then brought to pH = 7 using a 2 M NaOH solution. The hydrogels fully swell and the mixture becomes clear and elastic. We use two different Carbopol mixtures. Mixture 1 consists of 40% wt. glycerol and variable concentrations of Carbopol (0.1% − 0.16% wt.), while mixture 2 consists of 2% glycerol, 30% ethanol and 0.3% Carbopol.

Due to the elasticity of the Carbopol mixtures, any air bubbles in the mixture take a long time to reach the free surface. In order to speed this process, the mixture is loaded into 50 mL centrifuge tubes and centrifuged at $\sim 100g$ for 2 min. The mixture then becomes completely clear of bubbles. This is essential as bubbles can affect both the imaging and dynamics of the experiment. Finally, we load the mixture in the cuvette used to make tori.

In the case of mixtures with higher glycerol concentration, the Carbopol is initially mixed and left overnight with water only. We then add glycerol in a second step and neutralize afterwards. The reason for this is that glycerol is not as polar as water and therefore it does not mix with the hydrogels as well as water does.

4.4.2 Rheology of Carbopol Mixtures

To characterize the material properties of the Carbopol mixtures we will use in the breakup experiments, we use both oscillatory and steady state rheology [see Appendix D.3]. These are performed in a cone-plate configuration with a diameter of 25 mm and an angle of 2.014^o. We first perform a strain sweep at an angular frequency of $\omega = 1$ rad/s in order

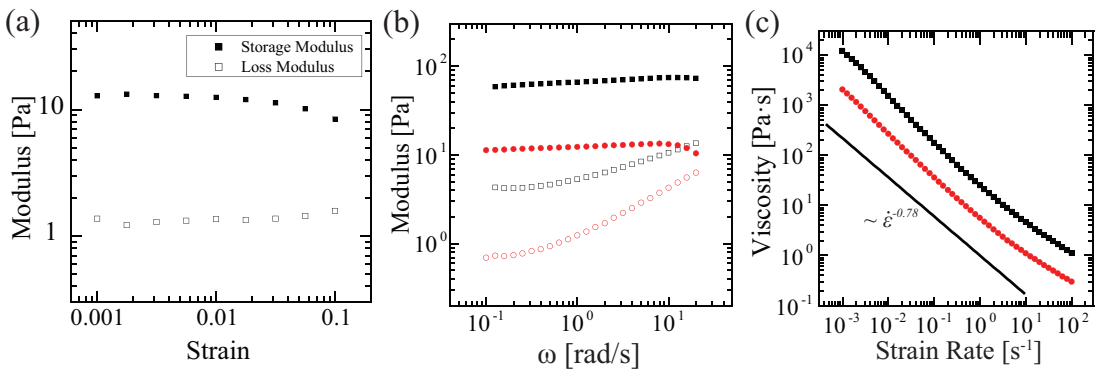

Figure 4.7: (a) A strain sweep of mixture 1 with 0.1% w/w Carbopol at $\omega = 1$ rad/s. (b) Oscillatory rheology using $\varepsilon = 0.01$ and (c) steady state rheology for mixture 1 with 0.1% w/w Carbopol (circles) and mixture 2 with 0.3% w/w (squares). For the oscillatory rheology the closed symbols refer to G' and the open to G''.

to find the linear regime, as shown in Fig. 4.7(a). From there, we use a strain for which both the elastic and viscous moduli, G' and G'', are frequency independent. We find that the linear regime is maintained up to a strain of ≈ 0.05. Fig. 4.7(b) shows the oscillatory rheology for mixtures 1 and 2. In both cases, $G' > G''$ and it is nearly ω-independent. The value of G' in this ω-range, $G'_{plateau}$, corresponds to the short-time elastic shear modulus of the mixture. We find $G'_{plateau} \approx 12$ Pa for mixture 1, while for mixture 2, we find $G'_{plateau} \approx 60$ Pa; we see that $G'_{plateau}$ is a factor of 5 higher for mixture 2 than for mixture 1. This correlates with the Carbopol concentration in the mixtures.

In addition to the oscillatory rheology, we also perform steady state rheology. We thus apply a stress and measure the resultant strain rate. From here, we plot the ratio of the stress to the strain rate, which is a viscosity, as a function of $\dot{\varepsilon}$ [see Fig. 4.7(c)]. It is evident that both mixtures 1 and 2 shear-thin. In particular, $\mu \propto \dot{\varepsilon}^{-0.78\pm0.05}$ over a large range of $\dot{\varepsilon}$. Hence, our Carbopol mixtures closely resemble a power-law fluid with an exponent of $n = 0.22 \pm 0.05$. Both mixtures seem to exhibit the same behavior, with the only difference the magnitude of the viscosity, which is a factor of ≈ 5 higher for mixture 2 than for mixture 1.

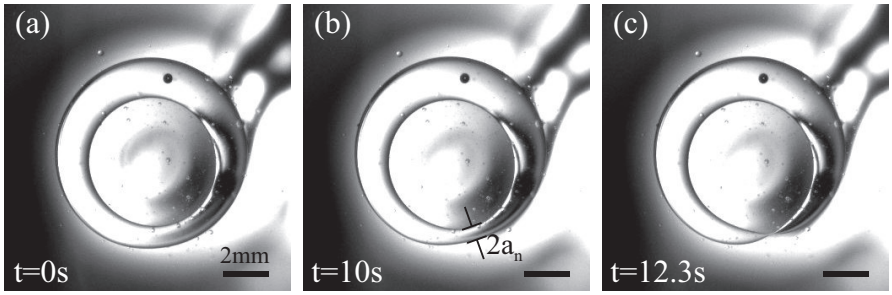

Figure 4.8: (a-c) The breakup of a 10 cSt silicone oil torus inside a 0.3% wt. carbopol mixture, showing that the neck radius, a_n, evolves slightly in the first 10 s followed by a rapid evolution in the next 2 s. The scale bar in alla images is 2 mm.

4.5 Break-up of Toroidal Droplets Inside Carbopol Mixtures

We produce toroidal droplets by injecting silicone oil through a metallic needle into a rotating cuvette containing the Cabopol mixture; the procedure is identical to that used with Newtonian liquids [see Section 2.2]. We use a $1,000$ cSt silicone oil as the inner liquid for mixture 1 and a 10 cSt silicone oil for mixture 2. The toroidal droplets generated have typical values of $0.51 \text{ mm} < a_0 < 1.2 \text{ mm}$ and $2.4 < \xi < 14.1$.

Fig. 4.8 exemplifies the breakup process of a toroidal droplet made of 10 cSt silicone oil in mixture 2. Interestingly, we observe that the torus evolves slightly towards breaking in the first 10 s [see Fig. 4.8(a,b)], and that it is only in the last $\sim$ 2 s where the neck evolves the most [see Fig. 4.8(b,c)]. In general, the breakup process can take anything from 15 seconds to 3 minutes, depending on a_0 and the materials used.

From the evolution of the neck, we obtain the strain:

$$\varepsilon = \frac{a_0 - a_n}{a_0}. \tag{4.8}$$

Consistent with our prior observation, ε initially increases slowly up to a point where it abruptly grows until breakup happens, as shown in Fig. 4.9(a). From ε, we obtain $\ln(\varepsilon)$. We find that $\ln(\varepsilon)$ is not linear with time, as shown in Fig. 4.9(b). This is very different from the exponential growth expected for simple liquids. We emphasize that the values of

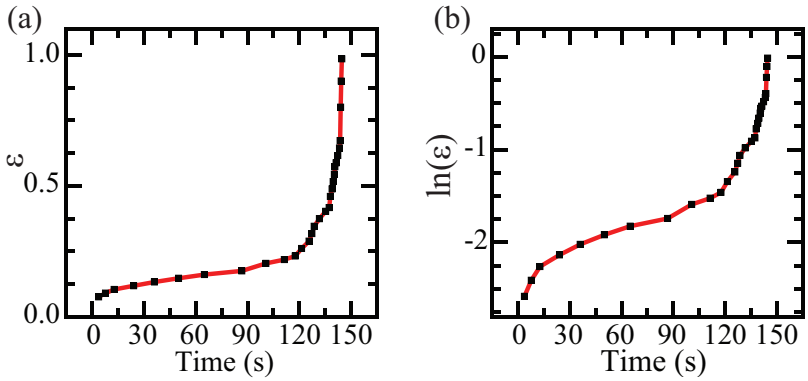

Figure 4.9: (a) The strain, ε and (b) $\ln(\varepsilon)$ as a function of time for a $1,000$ cSt solicone oil torus inside mixture 1 with 0.1% wt. carbopol.

ε are limited by the resolution of the camera. Hence, we only include points where the radius a_n has changed at least a pixel size; this is why the time intervals are not constant.

To understand our results, we consider the stability analysis of Tomotika and interpret the non-linear behavior in Fig. 4.9(b) due to the shear-thinning behavior of the Carbopol mixtures. Thus, we accept that $\varepsilon \sim e^{\nu t}$, such that $\frac{d(\ln \varepsilon)}{dt} = \nu$. From Tomotika's analysis, we have that $\nu \propto 1/\mu_o \Rightarrow \frac{d(\ln \varepsilon)}{dt} \sim 1/\mu_o$ [16]. Since $\mu_o = \mu_o(\dot{\varepsilon})$, a plot of ν^{-1} versus $\dot{\varepsilon}$ should reflect how μ_o changes with $\dot{\varepsilon}$. To test this, we obtain $\frac{d(\ln \varepsilon)}{dt}$ from the slope of $\ln(\varepsilon)$ versus t, and plot it versus $\dot{\varepsilon}$, obtained from the slope of ε versus t. Remarkably, the data from both Carbopol mixtures collapse on the same curve, as shown in Fig. 4.10, where we show data for 25 tori with different aspect ratios and tube radii. Additionally, we find that $\nu^{-1} \sim \dot{\varepsilon}^{\beta}$, with $\beta = -0.80 \pm 0.06$. This exponent is nearly identical to the exponent characterizing how μ_o depends on $\dot{\varepsilon}$, confirming our interpretation of the results. However, it is nevertheless remarkable that the data for both Carbopol mixtures scales together, since their viscosities are not the same [see Fig. 4.7(c)].

To understand this, we recall that viscoelastic jets break with characteristic time $\lambda = \mu_o/G'_{plateau}$. By scaling the outer fluid viscosity with the plateau modulus obtained in oscillatory rheology, we find that the curves for the viscosity of the Carbopol mixtures fall

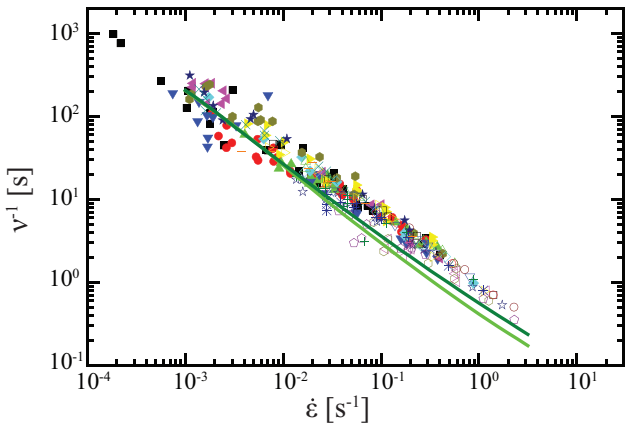

Figure 4.10: Plot of the local slopes of $\ln(\varepsilon(t))$ as a function of the slope of $\varepsilon(t)$ for all Carbopol mixtures showing all data collapsing on the same curve. The lines corespond to the viscosities as measured from the steady state rheologyscaled with their respective $G'_{plateau}$.

on top of each other, and in addition, they fall on top of the measured data, as shown with solid lines in Fig. 4.10. This indicates that in our experiments, $\nu \propto G'_{plateau}/\mu_o$, and that the non-linearities associated to shear-thinning enter the problem through μ_o. However, additional work treating the full non-linear problem at the outset is desirable. Our results nevertheless provide a framework that allows rationalizing the breakup of simple-fluid jets in non-Newtonian materials.

4.6 Conclusions

Work done in collaboration with P&G inspired us to study the breakup of a jet surrounded by a non-Newtonian material. We addressed this using toroidal droplets. We find that we can correlate instantaneous growth rates of the breakup process with the strain rate during the evolution. Importantly, this relation is also reflected in the shear-thinning behavior of the non-Newtonian material. As a result, we can describe the dynamics of the evolution by including the non-linearity in the linear theory for the breakup of jets through the dependence of the viscosity with $\dot{\varepsilon}$. Remarkably, the scaling factor for the breakup in the presence of different non-Newtonian materials is the short-time elastic modulus, reflecting

that the growth rate scales as $\nu \propto G'_{plateau}/\mu_o$.

CHAPTER 5
SUMMARY AND FUTURE DIRECTIONS

Geometry plays an important role in the evolution of liquid droplets. A toroidal droplet is unstable since its surface does not minimize the area for a given volume. There are two routes for toroidal droplets to transform into spheres; they can either break via Rayleigh-Plateau instabilities or shrink up to when the handle disappears. We refer to latter as the shrinking instability, which is inherent to the toroidal geometry and originates from the variation of the mean curvature, and hence of the Laplace pressure, around the tube of the torus. This pressure difference is larger in the outside of the torus than in the inside of the torus, thus driving the observed shrinking behavior.

This unique instability motivated both theoretical and computational work that were in contradiction with each other. While the theory assumed that the velocity is radial at the interface and that the cross-section remains circular during shrinking, the simulations found that the shape deforms significantly from circular as the droplet evolves. We perform particle image velocimetry experiments inside a shrinking torus to extract the flow field and determine the shape of the cross-section, and find that the cross-section of the torus significantly deviates from circular as the torus evolves. By exploiting the fact that our experiments are in the Stokes regime, we decompose the flow field to isolate the part that is due to only the shrinking process. We then use the radial and tangential components of the velocity at the interface and show that we need four modes of the many that contribute to the stream function, written in toroidal coordinates, to account for the circulation inside the torus, the source location in the flow field, the magnitude of the velocity, and the shape deformation during shrinking. However, the dominant mode in our experiments is the same as the one considered in the theory, which is causing the observed increase in the tube radius of the toroidal droplet as it shrinks.

Charging a toroidal droplet can reverse the shrinking instability and cause the expansion of the droplet. The transition from a shrinking to an expanding torus can be modeled using a simple pressure balance accounting for the effect of the electric stresses on the pressure jump across the interface. We calculate these stresses by considering that our droplet can be treated as a perfect toroidal conductor; we confirm this by measuring the capacitance for our toroidal droplets and seeing it agrees with the theoretical expectations for a toroidal conductor. Hence, the torus can be considered as electrostatically equilibrated and, thus, as equipotential. Interestingly, and in contrast to the neutral case, we find that charged droplets almost always end up breaking via Rayleigh-Plateau instabilities. Since in the thin torus limit, toroidal droplets approach the cylindrical limit, we test instability theories for electrified jets by looking at the breakup of slender and charged toroidal droplets. We compare the experimentally obtained dimensionless wavenumber of the fastest unstable mode, $(ka_0)_{max}$, with theoretical predictions, finding agreement between the two, and suggesting we can indeed use toroidal droplets as a platform to study charged jet breakup.

Remarkably, for higher electric stresses, we observe the torus develops finger-like structures as it expands. This is similar to the Saffman-Taylor instability that occurs in quasi-two dimensional systems. The toroidal confinement induces an inherent anisotropy, where the charge density is unevenly distributed around the tube causing the torus to evolve in a quasi-two dimensional fashion. As a result, even though our experimental system is three dimensional, the toroidal geometry enables Saffman-Taylor instabilities to develop. We find that this instability is in direct competition with the Rayleigh-Plateau breakup, which would cause the torus to break. This results in a critical capillary number of $Ca = 0.4$ above which the torus exhibits fingers. We further confirm that our observations are related to Saffman-Taylor instabilities by showing that the number of fingers in the experiments qualitatively follows the expected number of fingers obtained from linear stability analysis in radial Hele-Shaw cells. This suggests that, qualitatively, the charge sets the expansion speed of the torus without affecting significantly the properties of the growing fingers.

Finally, we exploit the fact that thin toroidal droplets break similar to cylindrical jets to address the breakup of a Newtonian jet inside a shear-thinning material using these type of droplets. Using linear stability analysis, we calculate the instantaneous growth rates during the breakup process and show that their strain-rate dependence mimics the strain-rate dependence of the viscosity. This implies that we can describe the breakup dynamics by including the non-linear behavior of the viscosity directly into the linear theory. Additionally, we find the scaling factor relating the viscosity and the growth rate to be the short-time elastic modulus. As a result, $\nu \propto G'_{plateau}/\mu_o$, reflecting the effect of the viscoelastic nature of the outer material on the breakup dynamics.

We believe that to completely understand some of our experimental results, theory needs to be developed. In particular, in the case of the Saffman-Taylor instability in toroidal droplets, work needs to be done to include the effect of the geometry and charge in the problem. It is important to note that we have considered the electrostatics and hydrodynamics separately. However, they are coupled since the geometry affects the electrostatic stresses, while the electrostatic stresses affect the flow field, which in turn changes the shape of the torus. As a result, to completely understand our experimental results, this coupling must be considered. In addition, for the breakup of toroidal droplets in a shear-thinning material, theoretical work dealing with the full non-linear problem explicitly would allow exploring the limits of our findings and confirming our interpretations. Our work will hopefully inspire theoretical groups to perform these calculations.

Another future direction of our research is an additional transition that happens for charged toroidal droplets at even higher voltages than those explored in detail in this work. At these higher voltages, the torus develops perturbations similar to the Saffman-Taylor instability. However, the perturbations develop much faster, in greater numbers, and grow quickly in a dendritic pattern; the perturbations are very thin and split multiple times as they evolve [see Fig. 5.1(a-c)].

It would also be interesting to study the effect of inertia on the flow field inside a shrink-

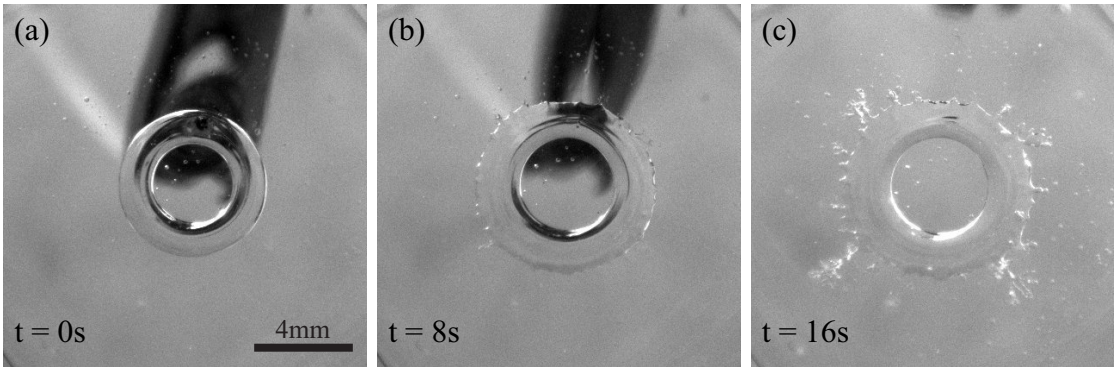

Figure 5.1: The evolution of a torus made of 16 mM SDS in 2% w/w amynopropyl terminated silicone oil 60,000 cSt silicone oil. The applied voltage is 4 kV.

ing droplet. For low *Re*, the flow field observed results from the viscous stresses exerted on the interface. By increasing *Re*, the inertial terms of the Navies-Stokes equations become important, and compete with those associated to viscous stresses. As a result, the shape and flow field of such droplets will be very different from what we have seen at low *Re*. In addition, the relevant equations of motion are non-linear, and thus, decomposing the flow field to extract the component that corresponds to shrinking is not possible. Hence, such experiments need to be done in perfect density matched conditions or under microgravity so that gravitational effects are negligible.

Appendices

APPENDIX A
INTERFACIAL TENSION MEASUREMENT USING THE PENDANT DROP METHOD

An important parameter in all of our experiments is interfacial tension, which qualitatevely-accounts for the energy cost of molecules being at the interface in contact with another substance. Young and Laplace found that the effect of surface tension results in a pressure difference across the interface [125, 126]:

$$\Delta p = p_{in} - p_{out} = 2\gamma H, \tag{A.1}$$

where p_{in} and p_{out} are the pressures at both sides of the interface, γ the interfacial tension, and H the mean curvature. The mean curvature is defined using the two principal radii of curvature, R_1 and R_2, as:

$$H = \frac{1}{2}\left(\frac{1}{R_1} + \frac{1}{R_2}\right). \tag{A.2}$$

Specifically, the two principal radii of curvature are given along the direction of the surface with the minimum and maximum curvatures, and these directions are always orthogonal to each other. However, H is invariant if any other radii of curvature along any two orthogonal directions are used. As a result, we do not need to calculate the principal curvatures, but rather any two curvatures along orthogonal paths.

A common method to measure the interfacial tension between two liquids is the pendant drop method [127]. This method uses a drop formed by the more dense liquid hanging at the end of a cylindrical capillary immersed in the less dense liquid. A schematic of the setup is shown in Fig. A.1. We define a Cartesian coordinate system with the center at the bottom of the drop [see Fig. A.1]. In addition, we define the angle φ to be the angle of the tangent plane with respect to the x-axis on the curve at each point. Therefore, the radius of curvature

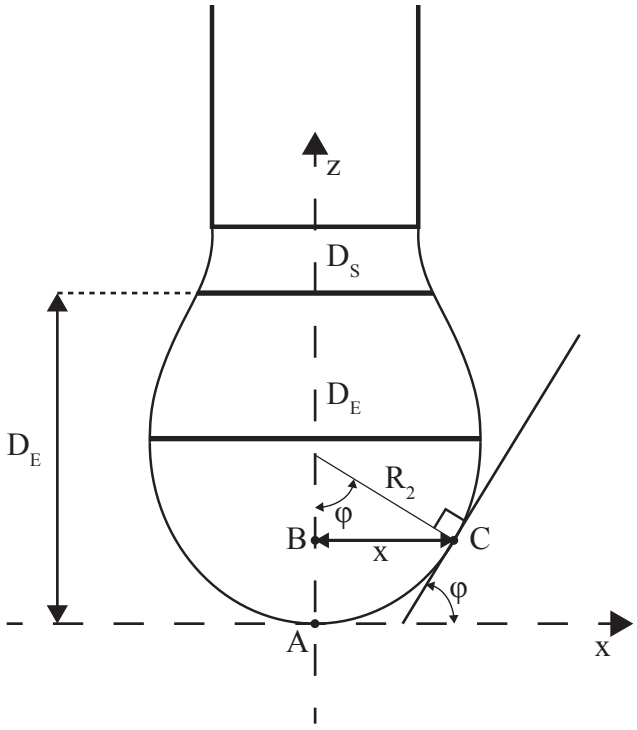

Figure A.1: A schematic of a pendant drop, and the coordinate system used.

at a point C on the curve is given by the perpendicular distance $R_2 = x/\sin(\phi)$, as shown in the schematic in Fig. A.1. For a system at rest, the stress must be balanced everywhere. As a result, the pressure across the interface due to the Young-Laplace pressure, must be balanced with the hydrostatic pressure, i.e.:

$$\begin{aligned}\Delta p_C &= p_{in,C} - p_{out,C} \\ &= (p_{in,A} - \rho_{in} g z) - (p_{out,A} - \rho_{out} g z) \\ &= \Delta p_A + (\Delta\rho) g z \end{aligned} \tag{A.3}$$

where Δp_A and Δp_C are pressure differences at points A and C, respectively, $\Delta\rho = \rho_{out} - \rho_{in}$ is the difference of the densities of the two liquids, g is the gravitational acceleration, and z is the height. Using R_2 and the Young-Laplace pressure at $A \equiv (x, z) = (0, 0)$ and at point C, we find that:

$$\gamma\left(\frac{1}{R_1} + \frac{\sin(\phi)}{x}\right) = \frac{2\gamma}{R_0} + (\Delta\rho)\, g z, \tag{A.4}$$

where R_0 is the radius of curvature at $(x, z) = (0, 0)$, and R_1 the other radius of curvature at point C.

To find the curve that describes the profile of the drop, we write the curve equation in parametric form:

$$x = x(s) \text{ and } z = z(s), \tag{A.5}$$

where s is the arclength of the curve measured from the origin. From geometric considerations, we find the differential form of the curve:

$$\frac{dx}{ds} = \cos(\phi) \tag{A.6}$$

and

$$\frac{dz}{ds} = \sin(\phi). \tag{A.7}$$

In addition, the curvature on the plane of the schematic in Fig. A.1 is given by definition as [128]:

$$\frac{1}{R_1} = \frac{d\phi}{ds}. \tag{A.8}$$

By combining equations A.4 and A.8, and non-dimensionalizing with R_0, i.e. $\tilde{s} = s/R_0$, $\tilde{x} = x/R_0$, and $\tilde{z} = z/R_0$, we arrive at a set of differential equations that describe the curve of the pendant drop:

$$\begin{aligned} \frac{d\tilde{x}}{d\tilde{s}} &= \cos(\phi), \\ \frac{d\tilde{z}}{d\tilde{s}} &= \sin(\phi), \\ \frac{d\phi}{d\tilde{s}} &= 2+\beta - \frac{\sin(\phi)}{\tilde{x}}, \end{aligned} \tag{A.9}$$

where $\beta = \frac{(\Delta\rho)gR_0^2}{\gamma}$ is the Bond number, which reflects the relevant strength between gravitational forces and surface tension forces.

One method to find the interfacial tension is to numerically solve equations A.9 for

different β, and to find the β that fits the experimental profile best.

Another method is based on the ratio $\sigma = \frac{D_S}{D_E}$, where D_E is the maximum horizontal distance of the pendant drop and D_S is the horizontal distance of the drop at height D_E from the bottom of the droplet; these are shown in Fig. A.1. For a range of β from 0.1 to 0.5, it has been numerically solved that β depends on σ as [127]:

$$\beta = 0.12836 - 0.7577\sigma + 1.7713\sigma^2 - 0.5426\sigma^2. \tag{A.10}$$

Hence, by measuring σ, we can calculate β.

Note that both methods measure β, and not the surface tension, γ. As a result, R_0 needs to be determined independently. This is done numerically by fitting a circle locally at $(x, z) = (0, 0)$. Note that both methods are limited to the range of β they can measure. Specifically, $\beta \in [0.1, 0.5]$ for either method to provide a good estimate of γ [127]. Hence, this limits the values of γ that can be measured. For example, if an interfacial tension needs to be measured that is two orders of magnitude smaller than the most usual values, which are in the 10 mN/m range, R_0 needs to decrease by one order of magnitude smaller to keep β in the right range. This can be done by decreasing the radius of the cylindrical capillary by an order of magnitude. Similarly, if the two fluids have a small density difference, then R_0 needs to be increased by increasing the radius of the cylindrical capillary.

APPENDIX B

LIQUIDS AND COMPONENTS USED IN THE VARIOUS EXPERIMENTS

During the thesis, we have performed a number of experiments with different liquids. It is important to know the bulk and surface properties of the different fluids we have used. Here, we summarize the materials, their properties and in which experiments they have been used.

In most experiments that study the breakup of liquid tori, we used glycerol as the inner liquid. This is important, because if we used water, the experiments will only break into a single sphere. The reason is that the viscosity contrast in the case of water is $\beta = \mu_i/\mu_o = O(10^{-5})$. For such a small viscosity contrast the fastest unstable mode from stability analysis is $(k\alpha_0)_{max} \approx 0$ (see Section 3.5.1). As a result, the corresponding wavelength is very large and the torus will break only into a single drop. In contrast, by using glycerol as the inner liquid, $\beta \approx 1/20$, and the fastest unstable mode has $(k\alpha_0)_{max} \approx 0.53$ [16]. Subsequently, the corresponding wavelength is shorter than $2\pi R_0$ allowing the observation of multiple breakups.

For experiments were we wanted to control the value of γ and decrease it if needed, we used water as the inner liquid. We used surfactants to lower the interfacial tension. Since glycerol is a non-polar molecule, it does not dissolve a polar sufactant and, hence, it does not allow using common surfactants. A surfactant that is commonly used in our experiments is sodium dodecyl sulfate (SDS). For all surfactants there is a critical concentration above which the surface tension remains unchanged. This is called the critical micelle concentration (CMC) and it depends on both the surfactant and the solvent [129]. For SDS in water, the CMC is about 8 mM [130]. Hence, in our experiments we are typically using concentrations that are higher than the CMC to ensure that the experiments were performed with the same interfacial tension. We report all the different combinations

Table B.1: A list that contains the inner and outer liquids used in different experiments, the sections in the thesis that these experiments were used, and the measured interfacial tension.

Section	Inner Liquid	Outer Liquid	γ
Chapter 2 Section 3.4	0.1% w/w PEG 8000 in H_2O	60,000 cSt Silicone Oil	28 ± 1 mN/m
Sections 3.2-3.5	Glycerol	30,000 cSt Silicone Oil	32 ± 2 mN/m
Section 3.2	16mM SDS in H_2O	30,000 cSt Silicone Oil	11 ± 1 mN/m
Section 3.6	16mM SDS in H_2O	2% w/w ATSO in 60,000 cSt Silicone Oil	0.35 ± 0.05 mN/m

of liquids we have used in Table B.1, together with the measured interfacial tension.

In many experiments, it is important to know some physical parameters of the liquids. One important quantity is the dielectric constant. For water, $\epsilon_{water} = 78.5\epsilon_0$ [131]. For glycerol, $\epsilon_{glyc} = 42.5\epsilon_0$ [102]. For silicone oil, we found that $\epsilon_{S.O.} = 3.75\epsilon_0$ [see Section 3.2.3]. Another important quantity is the electrical conductivity. For silicone oil, we measured it to be $\sigma_{S.O.} = 10^{-13}$ S/m [132]. For glycerol, $\sigma_{glyc} = 2.87 \cdot 10^{-6}$ S/m [102]. For a 16mM SDS in water, $\sigma_{SDS} = 9.8 \cdot 10^{-2}$ S/m.

The addition of surfactants can cause other effects in our experiments besides the decrease of interfacial tension. In particular, when a spherical droplet sediments, the circulation inside the droplet can cause concentration gradients at the interface. As a result, Marangoni stresses opposing the circulation can be generated and cause the droplet to sink similar to a solid sphere instead of a liquid sphere [83]. To determine if this is the case in our system, we compare experiments with different surfactant concentrations. Fig. B.1(a-c) shows the evolution of a torus with inner liquid of 10 mM SDS in water and outer liquid 30,000 cSt silicone oil, at different shrinking stages. Since different experiments will have different size tori, we scale the dynamics in our experiments with the capillary time that is the charactersitc time scale in our experiments [3], $t_{cap} = \mu_o a_0/\gamma$. This shows that the evolution takes longer for larger tori. We set then the dimensionless time scale as $\tau = t/t_{cap}$.

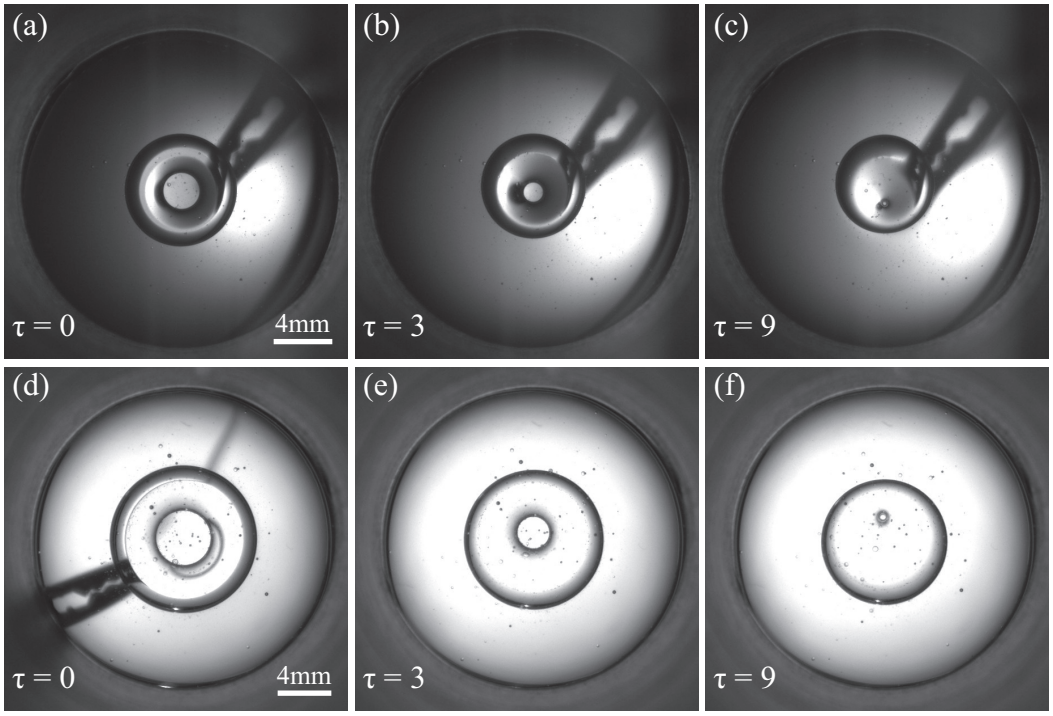

Figure B.1: The evolution of two tori in 30,000 cSt silicone oil with (a-c) $\xi \approx 1.9$ made out of 10mM SDS in water and (d-f) $\xi \approx 2.1$ $\xi \approx 1.9$ made out of 60mM SDS in water. The time reported is scaled with the capillary time $t_{cap} = \frac{\mu_o a_0}{\gamma}$.

We then show another torus with similar aspect ratio, but different size and with an inner liquid of 60 mM SDS in water [see Fig. B.1(d-f)]. We show that for the same τ the evolution between the two experiments is identical, and therefore we do not have an effect from Marangoni stresses in our experiments.

APPENDIX C
STOKES STREAMFUNCTION OF A GENERALIZED ORTHOGONAL COORDINATE SYSTEM

In the Stokes regime the inertial terms in the Navier-Stokes equations are negligible resulting in the Stokes equations:

$$\mu \Delta \boldsymbol{V} = \boldsymbol{\nabla} p, \tag{C.1}$$

$$\boldsymbol{\nabla} \cdot \boldsymbol{V} = 0, \tag{C.2}$$

where μ is the viscosity, $\boldsymbol{V}$ the velocity, and p the pressure. Equation C.1 corresponds to the stress balance within the liquid, while equation C.2 is the incompressibility condition using mass continuity.

The stream function in the Stokes regime is defined in the case of two dimensional flow with only two nonzero velocity components. Let the coordinates of our system be:

$$q_1 = q_1(x, y, z), \tag{C.3}$$

$$q_2 = q_2(x, y, z), \tag{C.4}$$

$$q_3 = q_3(x, y, z) \tag{C.5}$$

and the velocity to be:

$$\boldsymbol{V}(q_1, q_2, t) = u_1 \hat{\boldsymbol{e}}_{\mathbf{1}} + u_2 \hat{\boldsymbol{e}}_{\mathbf{2}} + 0 \hat{\boldsymbol{e}}_{\mathbf{3}}, \tag{C.6}$$

where $\hat{\boldsymbol{e}}_{\boldsymbol{i}}$ is the unit vector along q_i. The stream function is defined such that incompressibility (Eq.C.2) is satisfied. For a generalized orthogonal coordinate system the divergence

of a vector function $\boldsymbol{A}(q_1, q_2, q_3)$ is writen as [133]:

$$\boldsymbol{\nabla} \cdot \boldsymbol{A} = \frac{1}{h_1 h_2 h_3} \left(\frac{\partial}{\partial q_1} (A_1 h_2 h_3) + \frac{\partial}{\partial q_2} (A_2 h_3 h_1) + \frac{\partial}{\partial q_3} (A_3 h_1 h_2) \right), \tag{C.7}$$

where

$$h_i^2 = g_{ii} = \left(\frac{\partial x}{\partial q_i} \right)^2 + \left(\frac{\partial y}{\partial q_i} \right)^2 + \left(\frac{\partial z}{\partial q_i} \right)^2 \tag{C.8}$$

with g_{ii} the diagonal elements of the metric tensor of our coordinate system. In our case, $u_3 = 0$. Therefore, the incompressibility condition (Eq. C.2) is written as:

$$\boldsymbol{\nabla} \cdot \boldsymbol{V} = \frac{1}{h_1 h_2 h_3} \left(\frac{\partial}{\partial q_1} (u_1 h_2 h_3) + \frac{\partial}{\partial q_2} (u_2 h_3 h_1) \right) = 0. \tag{C.9}$$

We can therefore define the stream function, Ψ, as:

$$u_1 = \frac{1}{h_2 h_3} \frac{\partial \Psi}{\partial q_2}, \tag{C.10}$$

$$u_2 = -\frac{1}{h_3 h_1} \frac{\partial \Psi}{\partial q_1}, \tag{C.11}$$

which automatically satisfies equation C.9.

Another way to define the stream function by exploiting the incompressibility condition is by writing the velocity as $\boldsymbol{V} = \boldsymbol{\nabla} \times \vec{\Psi}_{curl}$, where $\vec{\Psi}_{curl} = \Psi_{curl} \hat{\boldsymbol{e}}_{\boldsymbol{3}}$. This always satisfies incompressibility, since $\boldsymbol{\nabla} \cdot \boldsymbol{\nabla} \times \boldsymbol{A} = 0$ for any $\boldsymbol{A}$. The curl of a vector function $\boldsymbol{A}$ in an orthogonal coordinate system is given by [133]:

$$\begin{aligned} \boldsymbol{\nabla} \times \boldsymbol{A} = & \frac{\hat{\boldsymbol{e}}_{\boldsymbol{1}}}{h_2 h_3} \left[\frac{\partial}{\partial q_2} (h_3 A_3) - \frac{\partial}{\partial q_3} (h_2 A_2) \right] + \\ & \frac{\hat{\boldsymbol{e}}_{\boldsymbol{2}}}{h_3 h_1} \left[\frac{\partial}{\partial q_3} (h_1 A_1) - \frac{\partial}{\partial q_1} (h_3 A_3) \right] + \\ & \frac{\hat{\boldsymbol{e}}_{\boldsymbol{3}}}{h_1 h_2} \left[\frac{\partial}{\partial q_1} (h_2 A_2) - \frac{\partial}{\partial q_2} (h_1 A_1) \right] \end{aligned} \tag{C.12}$$

In our case, we have $\vec{\Psi}_{curl} = \Psi_{curl}\hat{\boldsymbol{e}}_{\boldsymbol{3}}$. Therefore the velocity is written as:

$$\boldsymbol{V} = u_1\hat{\boldsymbol{e}}_{\boldsymbol{1}} + u_2\hat{\boldsymbol{e}}_{\boldsymbol{2}} = \boldsymbol{\nabla} \times \vec{\Psi}_{curl} = \frac{\hat{\boldsymbol{e}}_{\boldsymbol{1}}}{h_2 h_3}\frac{\partial}{\partial q_2}\left(h_3\Psi_{curl}\right) - \frac{\hat{\boldsymbol{e}}_{\boldsymbol{2}}}{h_3 h_1}\frac{\partial}{\partial q_1}\left(h_3\Psi_{curl}\right). \tag{C.13}$$

This definition is identical to the previous except for a prefactor in the stream function. Specifically, we can write $\Psi_{curl} = \frac{\Psi}{h_3}$, and we recover back equations C.10 and C.11.

Now that we have defined our stream function, we want to derive a differential equation to solve for Ψ. We are starting with the momentum equations from Stokes equations (Eq. C.1). By applying the curl on both sides, we find that:

$$\Delta(\boldsymbol{\nabla} \times \boldsymbol{V}) = \Delta\boldsymbol{\omega} = 0, \tag{C.14}$$

where $\boldsymbol{\omega} = \boldsymbol{\nabla}\times\boldsymbol{V}$ is the vorticity. In the above equation, we used the fact that the Laplacian commutes with the curl, and we moved the curl with the $\boldsymbol{V}$. This is also called the vorticity equation in the Stokes regimes. Taking a closer look at the vorticity, we write:

$$\boldsymbol{\omega} = \boldsymbol{\nabla} \times \boldsymbol{V} = \boldsymbol{\nabla} \times \boldsymbol{\nabla} \times \left(\frac{\Psi}{h_3}\hat{\boldsymbol{e}}_{\boldsymbol{3}}\right). \tag{C.15}$$

Assuming that $\boldsymbol{h_1}$, $\boldsymbol{h_2}$, and $\boldsymbol{h_3}$ are independent of $\boldsymbol{q_3}$, we find using equation C.12:

$$\boldsymbol{\omega} = -\frac{\hat{\boldsymbol{e}}_{\boldsymbol{3}}}{h_1 h_2}\left(\frac{\partial}{\partial q_1}\left(\frac{h_2}{h_1 h_3}\frac{\partial\Psi}{\partial q_1}\right) + \frac{\partial}{\partial q_2}\left(\frac{h_1}{h_2 h_3}\frac{\partial\Psi}{\partial q_2}\right)\right). \tag{C.16}$$

This assumption is important, otherwise we have extra terms from equation C.12 along $\hat{\boldsymbol{e}}_{\boldsymbol{1}}$ and $\hat{\boldsymbol{e}}_{\boldsymbol{2}}$. However, this is a reasonable assumption for many coordinate systems, like spherical, cylindrical, and toroidal, for which h_i are independent of the azimuthal angle, and for Cartesian, for which $h_i = 1$ for all i.

From the vorticity equation (Eq. C.14), we use the vector calculus identity, $\Delta\boldsymbol{\omega} =$

$\nabla(\nabla \cdot \boldsymbol{\omega}) - \nabla \times \nabla \times \boldsymbol{\omega}$. Since $\boldsymbol{\omega} = \nabla \times \boldsymbol{V}$, we know that $\nabla \cdot \boldsymbol{\omega} = 0$. Therefore, the vorticity equation can also take the form:

$$\nabla \times \nabla \times \boldsymbol{\omega} = 0, \tag{C.17}$$

which is very similar to equation C.15. By defining F such that $\boldsymbol{\omega} = \frac{F}{h_3}\hat{\boldsymbol{e}}_{\boldsymbol{3}}$, we can write equation C.17 similarly to equation C.15. In addition, we can write $F = -E^2\Psi$ using equation C.16, where E^2 is a second order differential operator defined as:

$$E^2 = \frac{h_3}{h_1 h_2}\left(\frac{\partial}{\partial q_1}\left(\frac{h_2}{h_1 h_3}\frac{\partial}{\partial q_1}\right) + \frac{\partial}{\partial q_2}\left(\frac{h_1}{h_2 h_3}\frac{\partial}{\partial q_2}\right)\right). \tag{C.18}$$

Similarly to deriving equation C.16 for Ψ, we find that:

$$\begin{gathered}\nabla \times \nabla \times \boldsymbol{\omega} = 0 \Rightarrow \\ \nabla \times \nabla \times \left(\frac{F}{h_3}\hat{\boldsymbol{e}}_{\boldsymbol{3}}\right) = -\frac{\hat{\boldsymbol{e}}_{\boldsymbol{3}}}{h_3}E^2 F = \frac{\hat{\boldsymbol{e}}_{\boldsymbol{3}}}{h_3}E^2 E^2 \Psi = 0.\end{gathered} \tag{C.19}$$

As a result, we arrive at the equation that describes the stream function: $E^2 E^2 \Psi = 0$.

As a final remark, the operator E^2 in some coordinate systems is the same as the Laplacian, but this is not true for all coordinate systems. Specifically, the scalar Laplacian for an orthogonal coordinate system is given by [133]:

$$\Delta = \frac{1}{h_1 h_2 h_3}\left(\frac{\partial}{\partial q_1}\left(\frac{h_2 h_3}{h_1}\frac{\partial}{\partial q_1}\right) + \frac{\partial}{\partial q_2}\left(\frac{h_3 h_1}{h_2}\frac{\partial}{\partial q_2}\right) + \frac{\partial}{\partial q_2}\left(\frac{h_1 h_2}{h_3}\frac{\partial}{\partial q_3}\right)\right). \tag{C.20}$$

This expression is the same as equation C.18 for a two-dimensional system only if $h_3 = \pm 1$. For example, this is true for a Cartesian coordinate system, or a cylindrical coordinate system when $q_3 = z$ or $q_3 = r$, but not for $q_3 = \phi$ since in this case $h_\phi = r$.

APPENDIX D

RHEOLOGY

D.1 Basics of Deformation, Stress, and Flow

Rheology refers to the study of flow and deformation of materials. In rheology, we measure the response of a material as we apply a strain deformation or stress. In our case, we use shear rheology, in that the stress or strain is applied tangential to the interface of the material. This is depicted, for a material sandwiched between two plates in Fig. D.1. We call the deformation from its initial state as Δx. The strain in this case is defined as $\epsilon = \frac{\Delta x}{h}$, where h is the distance between the plates. Hence, ϵ corresponds to the local deformation relative from the initial state. The shear stress is given by the average force, F, exerted on the plate, i.e. $\sigma = \frac{F}{A}$ with A the surface area.

To understand the meaning of the response functions of a material, we will first consider the straight forward simpler cases of a pure fluid and a solid. In the case of a pure solid, $\sigma = G\epsilon$, where G is the elastic shear modulus. For a pure fluid, $\sigma = \mu\dot{\epsilon}$, where μ is the viscosity and $\dot{\epsilon} = \frac{d\epsilon}{dt}$ is the strain rate. Therefore, for a liquid the stress scales linearly with $\dot{\epsilon}$, in contrast to a solid.

In order to characterize a material there are different tests that we can perform. In a creep test, a constant stress is applied on the material and the resultant strain is measured over time; the response function in this case is the creep compliance. In a stress relaxation test, a constant strain is applied and the resultant stress is measured as a function of time. For such a situation the response function is the relaxation modulus. In both of these example, the response function is time dependent.

We, however, will focus on two other tests: oscillatory rheology, where the stress/strain oscillates back and forth, and controlled shear-rate (CSR) rheology, where we impose a

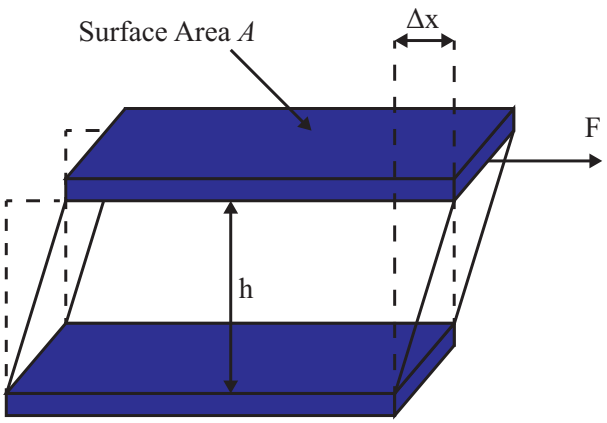

Figure D.1: Schematic of shear stress applied on a material. The stress is given by F/A, while the strain is given by $\Delta X/h$.

stress and measure the strain rate.

D.2 Steady-State Rheology

In a creep test, a constant stress, σ_0, is applied and we measure the resultant strain as a function of time. A typical ϵ vs. t curve for a viscoelastic material is shown in Fig. D.2(a). Initially, the strain reaches a value close to σ_0/G due to its short-time elastic response, but over time the material flows and reaches a steady-state where $\dot{\epsilon}$ is constant. Hence, we can use the steady-state to extract the long-time viscosity: $\eta = \sigma_0/\dot{\epsilon}$.

Similarly, we can plot σ vs. $\dot{\epsilon}$ in a CSR test and extract the viscosity of the material as $\sigma/\dot{\epsilon}_0$ as a function of $\dot{\epsilon}$. This test can elucidate whether a material, for example, shear-thins. Importantly, if the material has a yield stress, it will not flow for stresses σ_0 less than the yield stress, τ_{ys}.

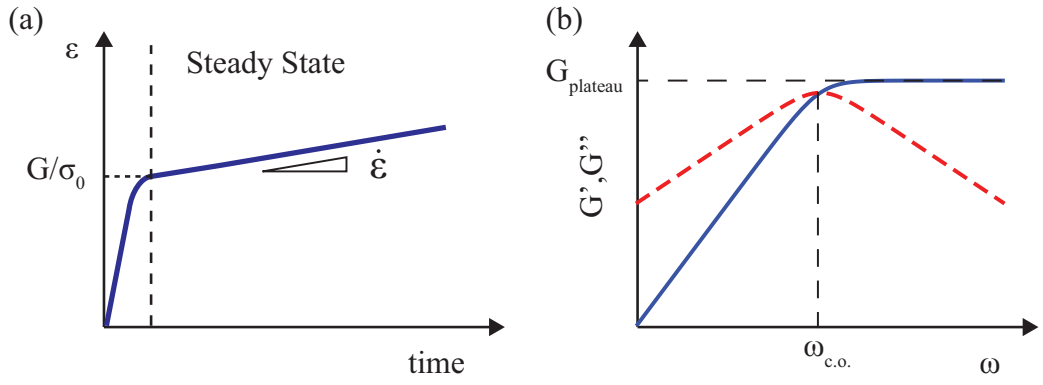

Figure D.2: Typical plots of a viscoelastic material for (a) a creep test and (b) oscillatory rheology with G' and G'' the solid and dsahed lines,respectively.

D.3 Oscillatory Rheology

D.3.1 Storage and Loss Modulus

Oscillatory rheology characterizes the material response in frequency space. To probe the viscoelastic behavior at a frequency ω, we apply a sinusoidal shear deformation:

$$\epsilon = \epsilon_0 \sin(\omega t) \tag{D.1}$$

and measure the resultant response $\sigma(t)$. For an elastic material, $\sigma_e = G\epsilon = \sigma_0 \sin(\omega t)$. Therefore, the response is in phase with the input signal. On the other hand, the response of a pure viscous liquid is $\sigma_v = \mu\dot{\epsilon} = \mu\epsilon_0\omega\cos(\omega t)$ and it is out-of-phase with ϵ by $\pi/2$. Note that the amplitude of σ_v grows linearly with ω.

For viscoelastic materials, we write the response, $\sigma(t)$, as:

$$\sigma(t) = G'\epsilon_0 \sin(\omega t) + G''\epsilon_0 \cos(\omega t), \tag{D.2}$$

where G' is the in-phase component, called the elastic or storage modulus, and G'' is the out-of-phase component, called the viscous or loss modulus. Generally, the storage and

loss moduli are frequency dependent, i.e. $G' = G'(\omega)$ and $G'' = G''(\omega)$. For frequencies where $G'(\omega) > G''(\omega)$ the material is considered solid-like, while for $G'(\omega) < G''(\omega)$ it is considered liquid-like. A typical curve of a viscoelastic material is shown in Fig. D.2(b). For a viscoelastic material at high frequencies, $G' > G''$, and the material is solid-like and has a constant G', called plateau modulus, $G_{plateau}$. In contrast, for low frequencies, $G'' > G'$, and the material is liquid-like, and has a $G'' \propto \omega^n$. For a pure liquid, $n = 1$ and $G'' = \mu\omega$. The time associated with the change from liquid-like to solid-like behavior is called the relaxation time, $t_{rel} = 2\pi/\omega_{c.o.}$ with $\omega_{c.o}$ the crossover frequency where $G' = G''$.

It is very critical to note here that we made an assumption in the above derivation, which is that that we can write the response, $\sigma(t)$, as given in equation D.2. This implies that we assumed that $\sigma(t)$ is linear with ϵ and $\dot{\epsilon}$, which is not necessarily true. Think about an elastic spring. Hooke's law assumes that as soon as you stop applying a force, the spring will return to its initial position. However, if we stretch the spring long enough that it permanently deforms, it will not be able to return to its initial state. These permanent deformations change the measured spring constant, and as a result the spring becomes non-linear. This can happen in soft materials, when high enough strain can cause the system to permanently rearrange causing non-linear responses.

D.3.2 Lissajous Curves and the Linear Regime

A plot of $\sigma(t)$ as a function of $\epsilon(t)$ is called a Lissajous curve. If equation D.2 holds, this curve is an ellipse and we are within the linear regime [see Fig. D.3(a)]. In the non-linear regime, we must take into account higher order terms that change the shape of the Lissajous curve. An example of such a shape change is shown in Fig. D.3(b) As a result, one way to determine whether we are in the linear regime or not is to look at the Lissajous curve associated to our experiments. Alternatively, we can perform a strain sweep and identify the region where G' and G'' are strain independent. In this case, we perform an experiment at constant ω for different ϵ_0. For small ϵ_0, we will be in the linear regime, and G' and G''

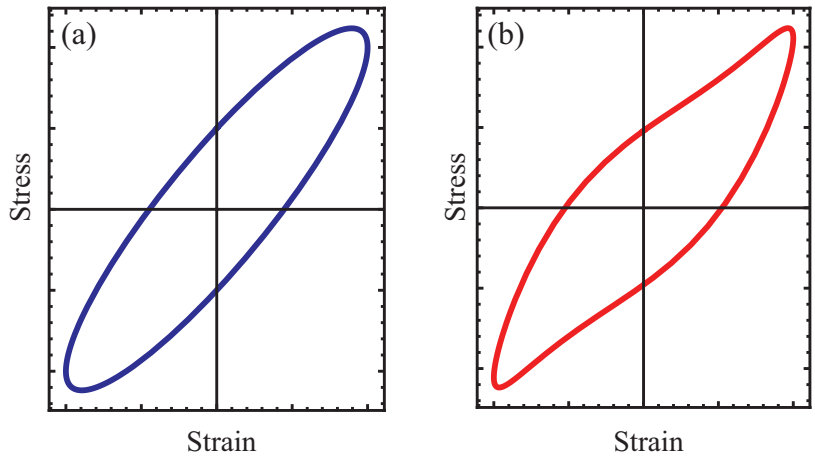

Figure D.3: (a) Characteristic Lissajous curves of a viscoelastic material (a) a linear response and (b) a non-linear response.

are constant. Above a threshold ϵ_0, the moduli will change with ϵ_0, indicating the onset of the non-linear regime.

D.4 An Example: Rheology of ULC Microgels

Here, we demonstrate some rheological measurements with an example. We consider a suspension of ultra-low crosslinked (ULC) microgels that has been used in our lab in connection to biomedical applications.

D.4.1 Why ULC Microgels?

Fibrin/Microgel Constructs

ULC microgels are composed of poly(N-isopropylacrylamide) (pNIPAM) copolymerized with acrylic acid (AAc) and synthesized in the absence of exogenous cross-linker. Cross-linking and branching of the polymer chains forming these unique particles occurs via rare parasitic chain transfer reactions, leading to extremely deformable particles [134, 135].

This extreme deformability has been used to develop materials enabling cell invasion. In particular, it has been seen that connected networks of ULC particles can be dynamically

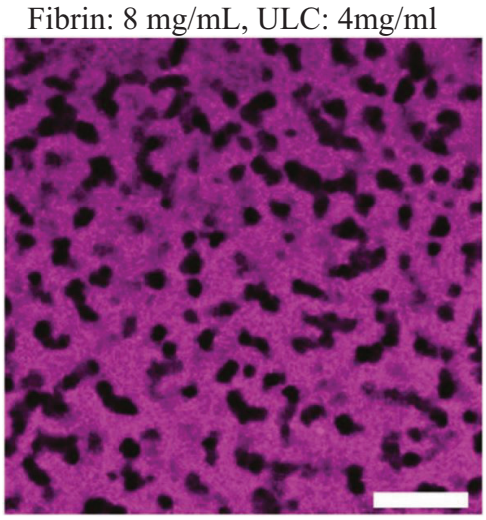

Figure D.4: A constuct made from an initial solution of 8 mg/ml fibrin, 4 mg/ml ULC microgels and 1 U/ml of thrombin.

assembled inside fibrin, which is a fibrous protein involved in the clotting of blood that is formed through a polymeric reaction of monomer fibrinogen in the presence of thrombin, an enzyme that catalyzes the reaction. It has been found that by including microgel particles in the initial mixture of fibrinogen and thrombin, the polymerization drives the particles into clusters first, and eventually into a connected network that spans the fibrin matrix. The parameters that determine if this will occur or not are the volume fraction of the particles and the concentration of thrombin, which determines how fast the polymerization reaction occurs. A slice of the system using confocal-microscopy can be seen in Fig. D.4, where the bright color corresponds to fluorescently labeled fibrin, while the black voids are the ULC microgels [136].

From a collection of slices along the z-direction, we can extract the microgel network. To do this, we first binarize the images in each stack. The threshold intensity value chosen is based on Otsu's method [137], which assumes that the intensity histogram of an image can be represented by two Gaussian distributions. The method scans through all possible intensities, and fits a single Gaussian distribution below that intensity and another one above that intensity, while keeping track of the error, which is given by the sum of squared

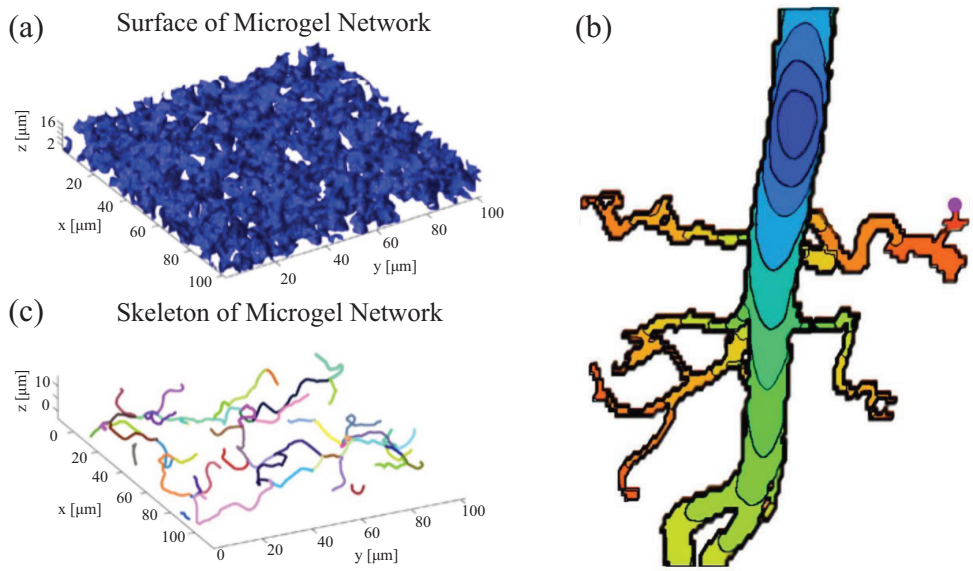

Figure D.5: (a)The surface of the microgel network after binarizing the image using Otsu's method. (b) A two-dimensional network with the solution of the eikonal equation from Ref. [138]. The colors represent contour plots of constant arrival times T. The distance traveled is larger for points at the center of the network corresponding to the skeleton of the network. (c) The measured skeleton for the microgel network shown in Fig. D.5(a).

residuals. The value of the intensity that minimizes the error is used as the threshold intensity. To have smoother edges, we use a median filter on a 10 μm by 10 μm window for each slice. After these processes, we can plot the surface that corresponds to the microgel network, as shown for an example in Fig. D.5(a).

Once we have the microgel network, we can extract the skeleton of the network. The skeleton is a line going through the network that represents the connectivity, branching and central line of the network. It will allow us to quantify the number of branches, and the radius of the "tunnels" in the network. The way we perform the skeletonization is using the eikonal equation, which we solve using the fast marching method. The eikonal equation is given by:

$$|\nabla T|F = 1, \tag{D.3}$$

where T is the arrival time and F the velocity of the propagation at every point. The way to think about this is that you have a source point in your network that the skeleton starts

from. From this point there is a propagation, similar to a wave, moving away from the source point, but confined inside the network, and the velocity of this propagation is given by F. We can represent this concept by writing in the following form:

$$F = \left| \frac{d\vec{r}}{dt} \right|. \tag{D.4}$$

The right hand side by definition is the magnitude of the velocity, and it is set to be equal to F. By inverting the right hand side, we arrive back to equation D.3. This allows us to understand the meaning of the absolute value, since equation D.4 tells us that the propagation does not have a specific direction and it expands uniformly out, but the magnitude is fixed to a given value F. Hence, in equation D.3, the arrival time $T(x, y, z)$ tells you the minimum time needed to move from the source point to a point (x, y, z) inside the network. This process is represented in Fig. D.5(b), where the "wave" starts at the top of the branch at the center of the circular dark blue region. The colors represent fronts with the same arrival time. In order to extract the center line, the velocity is chosen as $F(x, y, z) = (d(x, y, z)/D)^2$, where $d(x, y, z)$ is the distance map that is defined as the minimum distance from a given point (x, y, z) inside the network to the surface of the network, and D is the maximum value of $d(x, y, z)$ [138]. As a result, the propagation velocity is larger further from the surface, and it decreases to zero closer to the surface. This can be seen in Fig. D.5(b), where for a given arrival time T, the front of the "wave" has moved further along the center of the network. Hence, the path between two points that minimize the travel time gives the skeleton of the network.

Since equation D.3 has an absolute value, it is not trivial how to solve it. The reason is that the direction of propagation is not known since the absolute value eliminates this information. This is overcomed by using the fast marching method [139]. In this method, the direction of propagation is chosen such that the distance moved, $(\Delta x, \Delta y, \Delta z)$, in a time step, ΔT, is maximized. The direction of propagation is picked independently for each

Cartesian coordinate (x, y, z).

In the code, the way to pick the two points used to calculate a path of minimum time is through the distance map, d. The code finds all the local maxima of d. The reason is that local maxima in d are expected to be at locations where multiple "tunnels" of the network meet, since at those points the local volume of the network increases and, thus, there would be points that have a larger distance from the surface of the network compared to points inside the "tunnels" of the network. The code then selects the point with the maximum local distance, $D = d(\vec{r} = \vec{r}_0)$, at $\vec{r}_0 = (x_0, y_0, z_0)$. Then, the code locates the local maximum in d that is closest to point $\vec{r}_0$. Using these two points the code solves the eikonal equation and finds the path of minimum time, and stores all these points as a single branch. Then the code repeats this process for all other local maxima of d that are at least $2D$ away from all points of all measured branches. Similarly as before, it locates the closest local maximum of d, and calculates the next branch. When there are no more local maxima in d a distance $2D$ away from all branches, the program ends. We can then plot all the branches for the microgel network. This is shown in Fig. D.5(c).

Cell Spreading and Invasion

Fibrin is very dense, and can stop bleeding from an open wound, but, as a result, it does not allow for cells to rapidly enter and heal the wound. Our constructs can potentially be used to allow cells to penetrate the fibrin matrix, allowing for faster healing. In addition, since they are mostly made of fibrin, they essentially retain the mechanical properties of the pristine fibrin matrix and are able to prevent bleeding.

The key to cell penetration is that cells can move through the connected microgel networks in the constructs. How fast they do it is determined by the structural relaxation time of the ULC suspension in the "tunnels". As we mentioned, the relaxation time, t_{rel}, determines the time scale over which a viscoelastic material is predominantly liquid-like. At microscopic scales, this corresponds to the time for particles to spontaneously rearrange

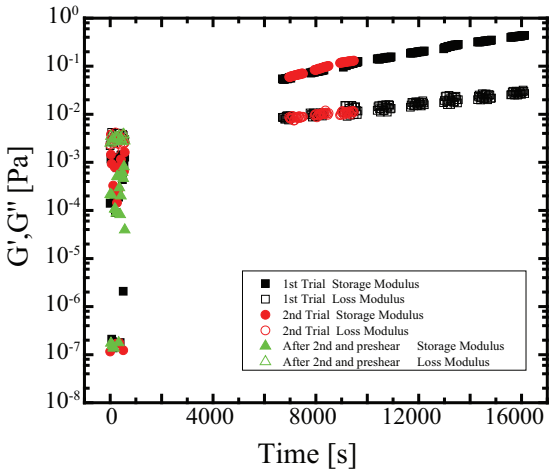

Figure D.6: Monitoring G' and G'' as function of time of a ULC microgel suspension at $\zeta = 0.6$. We used $\omega = 1$ rad/s and $\epsilon_0 = 0.01$.

due to thermal fluctuations. Hence, one of our contributions was to measure the rheological properties of the ULC suspension to confirm this idea.

D.4.2 Tool Selection and Preshear

To properly perform rheology, the tool used needs to be picked carefully and the material needs to be prepared appropriately. Any rheometer has a torque limit, a minimum torque that the rheometer can reliably measure. Every tool that is used has a conversion from torque to stress. As a result, different tools have different minimum stress that they can measure with the same rheometer. In general, the higher the surface area in contact with the sample, the larger the torque for a given stress. As a result, if we need to measure a material that is very soft, we need to use a tool with high surface area. However, there can be situations where the torque is below the torque limit. In this case, the points acquired cannot be trusted. Such an example is shown in Fig. D.6, where G' and G'' is measured for a ULC suspension over time. For the first 100 minutes, the sample is below the torque limit, and the points are disregarded. We have included some points at the beginning of the experiment to demonstrate that for such a situation, G' and G'' significantly fluctuate and

cannot be trusted.

We also need to prepare the sample appropriately. A difficulty with viscoelastic materials is that they have memory, and, thus, their response depends on the deformation history. This often times results in measurements that are not reproducible. To erase their memory, we need to develop a preshearing protocol. What we do is to shear the fluid at a high constant shear-rate for an extensive amount of time. For example, we find that shearing the material at $\dot{\epsilon} = 30\ s^{-1}$ for 10-15 minutes eliminates the deformation history and sets a reproducible state for the material. To determine if this is the case, we choose to monitor the material properties using a time sweep. This time sweep is at a constant frequency and strain. What we do is to monitor the evolution of G' and G'' for some time after the preshear, and repeat the experiment a few times applying the preshearing protocal in between. Since we recover the same time-dependence of G' and G'', this confirms the preshear protocol is effective.

D.4.3 Steady-State Rheology of ULC Microgels

To ensure physiological conditions, the solution used to re-suspend the microgels is 25mM HEPES buffer with 150 mM NaCl. The HEPES buffer fixes $pH \approx 7.4$. In the fibrin constructs, we estimate that the generalized volume fraction in the space occupied by the microgels is $\zeta = N \cdot v_{p,dil}/V_{total} \approx 0.6$, where N is the number of particles, $v_{p,dil}$ is the particle volume in dilute conditions, and V_{total} is the total available volume for the suspension.

The tool we use is a double gap couette made of titanium. We use the double gap to increase the contact ares and, hence, the torque in our experiments, since the viscosity of the suspension is small. We use a titanium tool to avoid corrosion due to the high salt concentration in the samples. All the experiments are done at a temperature of 37±0.1 °C. We note that the double gap couette uses a large amount of sample volume, 3.5 mL.

We also use an evaporation blocker to minimize evaporation. This is needed since the experiments can take several hours at a relatively high temperature. The evaporation

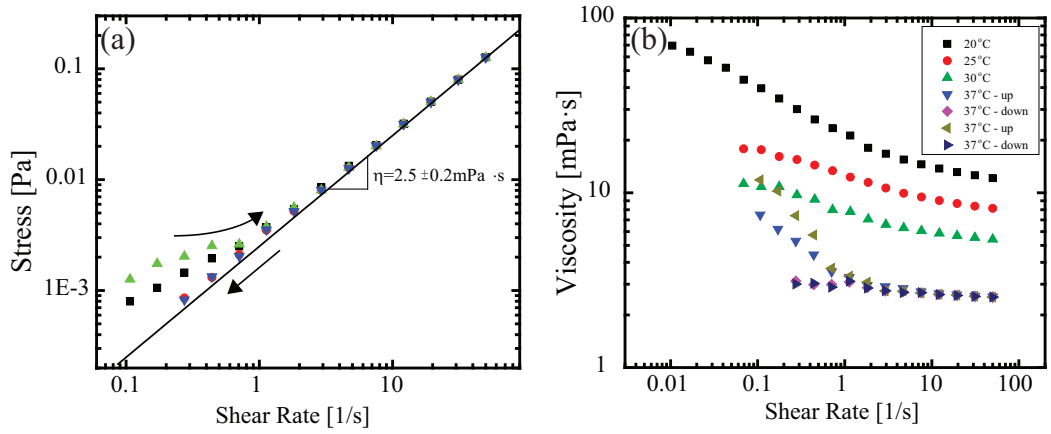

Figure D.7: (a) σ vs. $\dot{\epsilon}$ of the steady-state rheology of a ULC microgel suspension with $\zeta = 0.6$. We measured the stress with increasing $\dot{\epsilon}$ (▲,■) and decreasing $\dot{\epsilon}$ (▼,●). The viscosity is given by the slope of the curve. (b) The viscosity as a function of $\dot{\epsilon}$ for multiple temperatures for the same sample as (a).

blocker uses a simple fluid of low viscosity to prevent the air surrounding the sample from escaping. As a result, the air around the sample becomes saturated, reducing evaporation. The fluid we use is 10 cSt silicone oil. Silicone oil of lower viscosity consists of polymer chains that are shorter, therefore evaporating easier. Using the 10 cSt silicone oil, we confirmed the sample does not evaporate during the experiments. In addition to the evaporation blocker, there is a dimple at the top of the tool , which we fill with water in order to saturate the air faster. Finally, we preshear the sample at $\dot{\epsilon} = 25\ \mathrm{s}^{-1}$ for 15 minutes, and perform a time sweep at $\omega = 1$ rad/s and $\epsilon_0 = 0.01$ for 15 minutes, several times before any measurements.

We first performed experiments at $\zeta = 0.6$ at 37 °C, both increasing and decreasing $\dot{\epsilon}$. We find that for $\dot{\epsilon} > 1\ \mathrm{s}^{-1}$ the data is the same irrespective of whether we perform the experiment with ascending or descending $\dot{\epsilon}$ [see Fig. D.7(a)]. By fitting a line to the linear part of the data at sufficiently high $\dot{\epsilon}$, we can extract the viscosity of the material. We find $\mu = 2.5 \pm 0.2\ \mathrm{mP} \cdot \mathrm{s}$, which is very close to the viscosity of water. However, we observe that the data differ for low $\dot{\epsilon}$, exhibiting a mild hysteresis.

We performed experiments at different temperatures, as shown in Fig. D.7(b). We find

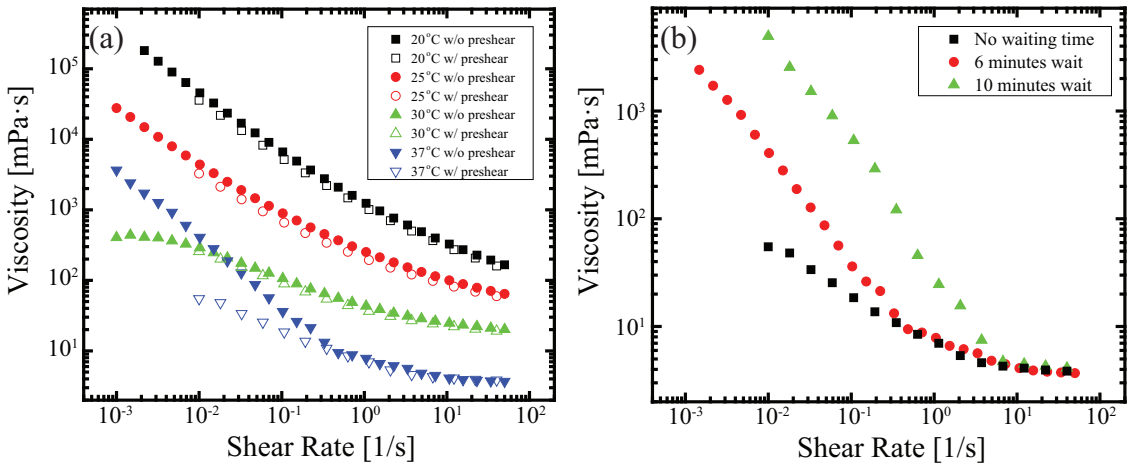

Figure D.8: (a) μ vs. $\dot{\epsilon}$ of a ULC microgel suspension with $\zeta = 1.0$ for different temperatures. The closed symbols correspond to measurements without preshear while the closed with preshear. (b) Steady-state rheology at $T = 37\,^{\circ}\text{C}$, waiting difeerent amount of times between preshear and steady-state rheology.

that the viscosity increases with decreasing temperature. This is due to fact that p-NIPAM particles are hydrophilic at temperature below 32.5 °C while they are hydrophobic for larger temperatures [140]. As a result the microgels swell as the temperature decreases, which in turn increases ζ and the sample becomes stiffer. The reported ζ correspond to the ζ if the sample is at $T = 37\,^{\circ}\text{C}$. In all cases, we see that the suspension shear-thins. However, the hysteresis only persists for the sample at $T = 37\,^{\circ}\text{C}$; it disappears at lower temperatures. This is an indication that whatever is happening is determined by temperature.

We then study the case of $\zeta = 1.0$. Learning from our previous experience, where we observed some hysterisis, we wanted to further test the preshear specifically for a sample at $T = 37\,^{\circ}\text{C}$. For that reason, we performed steady-state rheology with and without preshear. We find that the viscosity is the same except for $T = 37\,^{\circ}\text{C}$, where there is a difference between the two measurements [see Fig. D.8(a)]. At this concentration, the difference is so extreme that the viscosity is almost an order of magnitude different at low $\dot{\epsilon}$. To further test what is the cause of this behavior, we performed experiments that have been presheared, but we wait different amounts of time between the preshear and the steady-state rheology measurement. We find that the viscosity increases the more we wait between the

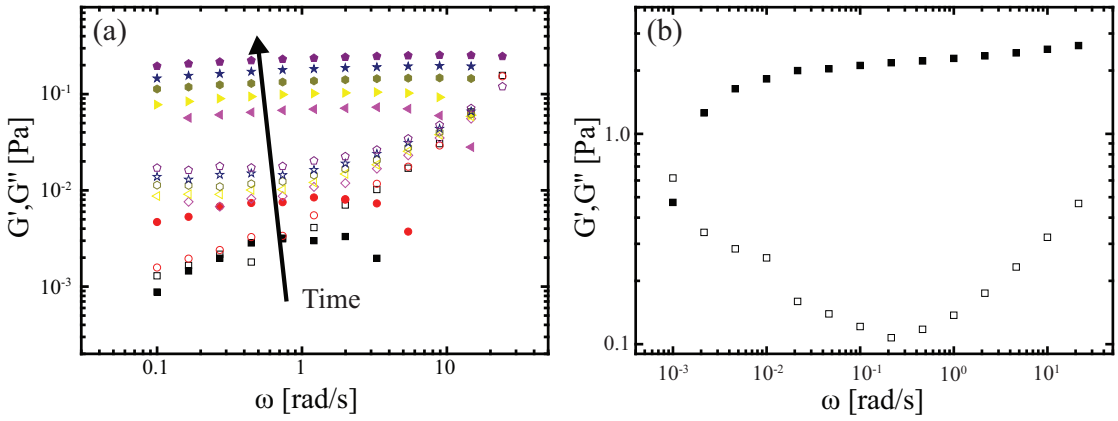

Figure D.9: (a) The oscillatory rheology between the intervals in Fig. D.6. The sample becomes more solid like with time. (b) Oscilaltory rheology of a ULC microgel suspension at $\zeta = 0.6$ with $\epsilon_0 = 0.01$ after 3 hours in the rheometer.

preshear and the steady-state rheology measurement, indicating that the system evolves over experimental times at this temperature [see Fig. D.8(b)].

D.4.4 Oscillatory Rheology of ULC Microgels

From what we have learned so far, the sample at $T = 37\,^{\circ}\mathrm{C}$ evolves in time, with the viscosity becoming larger over time. To further investigate what is happening, we perform oscillatory rheology, and monitor G' and G'' over time. In addition, we performe quick frequency sweeps every 15 minutes. We start with a sample at $\zeta = 0.6$ and use $\omega = 1$ rad/s and $\epsilon = 0.01$. We find that at early times, we measure torques below the torque limit, which we cannot trust, since we cannot extract meaningful data. However, we nevertheless show the data for the first 15 minutes, to show what the rheometer measures right at the beginning. We find that after about 100 minutes, the sample has become stiff enough such that the torque is above the torque limit. Surprisingly, we find that the sample is solid-like, with $G' > G''$ [see Fig. D.6], and that both moduli increase over time. We have repeated the experiment a few times, finding that the time scale for this behavior is persistent between experiments. By looking at the frequency sweeps, we find that the material is liquid-like right at the beginning of the experiment. However, it is solid-like for a range of ω [see

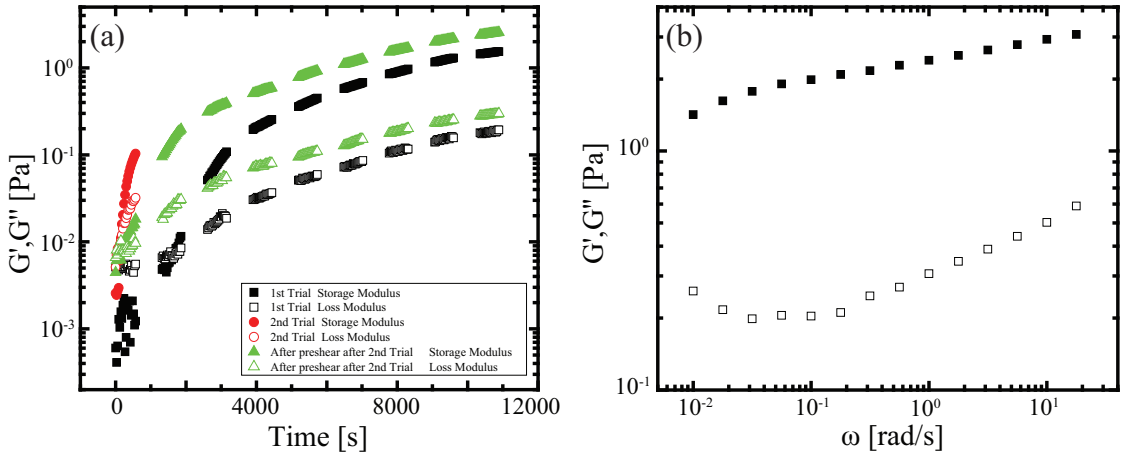

Figure D.10: (a) Monitoring G' and G'' as function of time of a ULC microgel suspension at $\zeta = 1.0$. We used $\omega = 1$ rad/s and $\epsilon_0 = 0.01$. (b) The oscillatory rheology of the sample after 4 hours in the rheometer.

Fig. D.9(a)]. After 3 hours in the rheometer, we perform a final frequency sweep using an extensive range of ω. We find that the material remains solid-like for frequencies as low as 0.02 rad/s [see Fig. D.9(b)].

Finally, we perform the same experiment for a sample with $\zeta = 1$. In this case, we find that the sample is above the torque limit immediatelly. We also find that the material stiffens fast, over a time of one hour [see Fig. D.10(a)]. Repeated experiments show consistently similar trends, however, the time scales are not as consistent as in the case of $\zeta = 0.6$. As before, we perform a frequency sweep for a higher ω-range to find that the suspension is solid-like for the whole range, with the plateau modulus being a little higher than in the case of $\zeta = 0.6$ [see Fig. D.10(b)].

From the oscillatory measurements, we can finally extract the information that we need on the structural relaxation of the microgel suspension inside the "tunnels". From Fig. D.9(b), we estimate that the crossover frequency in the case of $\zeta = 0.6$ to be $\omega_{c.o.} \approx 1.2 \cdot 10^{-3}$ rad/s. As a result, the characteristic timescale for particles to rearrange is: $t_{rel} = 2\pi/\omega_{c.o.} \approx$ 1.5 hours. Furthermore, we can estimate a characteristic timescale for the motion of the cells in the microgel network by considering the measured characteristic speed of the cells

inside the tunnels, $u_{cell} \approx 13$ μm/s, and the typical size of the cells ($d \sim 20$ μm), as $t_{cell} = d/u_{cell} \approx 1.5$ hours. This is consistent with the structural relaxation time of the microgel suspension, confirming that indeed the cells use the structural relaxation of the ultrasoft colloidal assembly to move through the network.

REFERENCES

[1] C. Boys, *Soap-Bubbles, their colors and forces which mold them*. Dover Science Books, 1958.

[2] E. Pairam and A. Fernández-Nieves, "Generation and stability of toroidal droplets in a viscous liquid," *Phys. Rev. Lett.*, 102, no., p. 234 501, 2009.

[3] Z. Yao and M. Bowick, "The shrinking instability of toroidal liquid droplets in the stokes flow regime," *Euro. Phys. J. E*, 34, no., pp. 1–6, 2011.

[4] P.-G. De Gennes and J. Prost, *The physics of liquid crystals*. Oxford: Clarendon Press, 1993.

[5] H. Hopf, "Vektorfelder in n-dimensionalen mannigfaltigkeiten," *Mathematische Annalen*, 96, no., pp. 225–249, 1927.

[6] H. Poincaré, "Mémoire sur les courbes définies par une équation différentielle (ii)," *Journal de mathématiques pures et appliquées*, no., pp. 251–296, 1882.

[7] J. Friedel, *Dislocations: International Series of Monographs on Solid State Physics*. Elsevier, 2013, vol. 3.

[8] F. Nabarro, *Theory of crystal dislocations*. Clarendon Pr., 1967.

[9] F. Nava, K. Tu, O. Thomas, J. Senateur, R. Madar, A. Borghesi, G. Guizzetti, U. Gottlieb, O. Laborde, and O. Bisi, "Electrical and optical properties of silicide single crystals and thin films," *Mater. Sci. Rep.*, 9, no., pp. 141–200, 1993.

[10] L. Thylén, M. Qiu, and S. Anand, "Photonic crystals–a step towards integrated circuits for photonics," *ChemPhysChem*, 5, no., pp. 1268–1283, 2004.

[11] T. Lopez-Leon, V. Koning, K. Devaiah, V. Vitelli, and A. Fernandez-Nieves, "Frustrated nematic order in spherical geometries," *Nature Phys.*, 7, no., pp. 391–394, 2011.

[12] E. Pairam, J. Vallamkondu, V. Koning, B. van Zuiden, P. Ellis, M. Bates, V. Vitelli, and A. Fernandez-Nieves, "Stable nematic droplets with handles," *Proc. Nat. Acad. Sci.*, 110, no., pp. 9295–9300, 2013.

[13] G. Taylor, "Disintegration of water drops in an electric field," 280, no., pp. 383–397, 1964.

[14] J. Plateau, "Mémoire sur les phénomènes que présente une masse liquide et soustraite à l'action de la pesanteur.," *Nouveaux mémoires de l'Académie Royale des Sciences et Belles-Lettres de Bruxelles*, 23, no., 1849.

[15] L. Rayleigh, "On the capillary phenomena of jets," 29, no., pp. 71–97, 1879.

[16] S. Tomotika, "On the instability of a cylindrical thread of a viscous liquid surrounded by another viscous fluid," *Proc. Roy. Soc. A*, 150, no., pp. 322–337, 1935.

[17] J. Fernández de La Mora, "The fluid dynamics of taylor cones," *Annu. Rev. Fluid Mech.*, 39, no., pp. 217–243, 2007.

[18] J. Fernandez de la Mora, J. Navascues, F. Fernandez, and J. Rosell-Llompart, "Generation of submicron monodisperse aerosols in electrosprays," *J. Aerosol Sci.*, 21, no., S673–S676, 1990.

[19] I. Romero-Sanz and J. Fernandez de la Mora, "Spatial structure and energy distribution of electrosprays of ionic liquids in vacuo," *J. Appl. Phys*, 95, no., pp. 2123–2129, 2004.

[20] I. Romero-Sanz, R. Bocanegra, J. Fernandez de la Mora, and M. Gamero-Castano, "Source of heavy molecular ions based on taylor cones of ionic liquids operating in the pure ion evaporation regime," *J. Appl. Phys.*, 94, no., pp. 3599–3605, 2003.

[21] J. Melcher, *Field-coupled surface waves*. MIT, 1963.

[22] A. Huebner and H. Chu, "Instability and breakup of charged liquid jets," *J. Fluid Mech.*, 49, no., pp. 361–372, 1971.

[23] A. Basset, "Waves and jets in a viscous liquid," *Amer. J. Math.*, 16, no., pp. 93–110, 1894.

[24] J. Schneider, N. Lindblad, C. Hendricks Jr, and J. Crowley, "Stability of an electrified liquid jet," *J. Appl. Phys.*, 38, no., pp. 2599–2605, 1967.

[25] G. Taylor, "Electrically driven jets," 313, no., pp. 453–475, 1969.

[26] D. Saville, "Electrohydrodynamic stability: Fluid cylinders in longitudinal electric fields," *Phys. Fluids*, 13, no., pp. 2987–2994, 1970.

[27] ——, "Stability of electrically charged viscous cylinders," *Phys. Fluids*, 14, no., pp. 1095–1099, 1971.

[28] M. Cloupeau and B. Prunet-Foch, "Electrostatic spraying of liquids in cone-jet mode," *J. Electrostat.*, 22, no., pp. 135–159, 1989.

[29] G. Artana, G. Touchard, and H. Romat, "Absolute and convective instabilities in an electrified jet," *J. Electrostat.*, 40, no., pp. 33–38, 1997.

[30] A. Yarin, W. Kataphinan, and D. Reneker, "Branching in electrospinning of nanofibers," *J. Appl. Phys.*, 98, no., p. 064 501, 2005.

[31] R. Collins, M. Harris, and O. Basaran, "Breakup of electrified jets," *J. Fluid Mech.*, 588, no., pp. 75–129, 2007.

[32] F. Li, X.-Y. Yin, and X.-Z. Yin, "Instability of a viscous coflowing jet in a radial electric field," *J. Fluid Mech.*, 596, no., pp. 285–311, 2008.

[33] Q. Wang and D. Papageorgiou, "Dynamics of a viscous thread surrounded by another viscous fluid in a cylindrical tube under the action of a radial electric field: Breakup and touchdown singularities," *J. Fluid Mech.*, 683, no., pp. 27–56, 2011.

[34] M. Goldin, J. Yerushalmi, R. Pfeffer, and R. Shinnar, "Breakup of a laminar capillary jet of a viscoelastic fluid," *J. Fluid Mech.*, 38, no., pp. 689–711, 1969.

[35] Y. Amarouchene, D. Bonn, J. Meunier, and H. Kellay, "Inhibition of the finite-time singularity during droplet fission of a polymeric fluid," *Phys. Rev. Lett.*, 86, no., p. 3558, 2001.

[36] Y. Christanti and L. Walker, "Surface tension driven jet break up of strain-hardening polymer solutions," *J. Non-Newton. Fluid Mech.*, 100, no., pp. 9–26, 2001.

[37] Y. Christanti and L. Walker, "Effect of fluid relaxation time on jet breakup due to a forced disturbance of polymer solutions," *J. Rheol.*, 46, no., pp. 733–748, 2002.

[38] R. Larson, *Constitutive Equations for Polymer Melts and Solutions: Butterworths Series in Chemical Engineering*. Butterworth-Heinemann, 2013.

[39] P. Doshi, R. Suryo, O. Yildirim, G. McKinley, and O. Basaran, "Scaling in pinch-off of generalized newtonian fluids," *J. Non-Newton. Fluid Mech.*, 113, no., pp. 1–27, 2003.

[40] A. Sanz, "The influence of the outer bath in the dynamics of axisymmetric liquid bridges," *J. Fluid Mech.*, 156, no., pp. 101–140, 1985.

[41] M. Mahajan, M. Tsige, P. Taylor, and C. Rosenblatt, "Stability of liquid crystalline bridges," *Phys. Fluids*, 11, no., pp. 491–493, 1999.

[42] J. Nicolás, "Hydrodynamic stability of high-viscosity cylindrical liquid bridges," *Phys. Fluids A: Fluid Dyn. (1989-1993)*, 4, no., pp. 1620–1626, 1992.

[43] O. Yildirim and O. Basaran, "Deformation and breakup of stretching bridges of newtonian and shear-thinning liquids: Comparison of one-and two-dimensional models," *Chem. Eng. Sci.*, 56, no., pp. 211–233, 2001.

[44] X. Zhang, R. Padgett, and O. Basaran, "Nonlinear deformation and breakup of stretching liquid bridges," *J. Fluid Mech.*, 329, no., pp. 207–246, 1996.

[45] J. Choi and T. Kato, "Static and dynamic behavior of liquid nano-meniscus bridge," *Tribol. T.*, 44, no., pp. 19–26, 2001.

[46] S. Berg, R. Kröger, and H. Rath, "Measurement of extensional viscosity by stretching large liquid bridges in microgravity," *J. Nonnewton. Fluid Mech.*, 55, no., pp. 307–319, 1994.

[47] G. McKinley and T. Sridhar, "Filament-stretching rheometry of complex fluids," *Ann. Rev. Fluid Mech.*, 34, no., pp. 375–415, 2002.

[48] A. Bazilevskii, V. Entov, M. Lerner, and A. Rozhkov, "Failure of polymer solution filaments," *Polym. Sci. Ser. A Chem. Phys.*, 39, no., pp. 316–324, 1997.

[49] A. Bazilevskii, V. Entov, and A. Rozhkov, "Failure of an oldroyd liquid bridge as a method for testing the rheological properties of polymer solutions," *Polym. Sci. Ser. A*, 43, no., pp. 1161–1172, 2001.

[50] A. Bazilevsky, V. Entov, and A. Rozhkov, "Liquid filament microrheometer and some of its applications," in *Third European Rheology Conference and Golden Jubilee Meeting of the British Society of Rheology*, Springer, 1990, pp. 41–43.

[51] M. Yao, S. Spiegelberg, and G. McKinley, "Dynamics of weakly strain-hardening fluids in filament stretching devices," *J. Nonnewton. Fluid Mech.*, 89, no., pp. 1–43, 2000.

[52] G. McKinley, O. Brauner, and M. Yao, "Kinematics of filament stretching in dilute and concentrated polymer solutions," *Korea-Aust. Rheol. J*, 13, no., pp. 29–35, 2001.

[53] J. Wang, D. Joseph, and T. Funada, "Purely irrotational theories of the effects of viscosity and viscoelasticity on capillary instability of a liquid cylinder," *J. Nonnewton. Fluid Mech.*, 129, no., pp. 106–116, 2005.

[54] Y.-C. Liao, H. Subramani, E. Franses, and O. Basaran, "Effects of soluble surfactants on the deformation and breakup of stretching liquid bridges," *Langmuir*, 20, no., pp. 9926–9930, 2004.

[55] S. Middleman, "Stability of a viscoelastic jet," *Chem. Eng. Sci.*, 20, no., pp. 1037–1040, 1965.

[56] V. Entov and E. Hinch, "Effect of a spectrum of relaxation times on the capillary thinning of a filament of elastic liquid," *J. Nonnewton. Fluid Mech.*, 72, no., pp. 31–53, 1997.

[57] M. Renardy, "Similarity solutions for jet breakup for various models of viscoelastic fluids," *J. Nonnewton. Fluid Mech.*, 104, no., pp. 65–74, 2002.

[58] ——, "A numerical study of the asymptotic evolution and breakup of newtonian and viscoelastic jets," *J. Nonnewton. Fluid Mech.*, 59, no., pp. 267–282, 1995.

[59] V. Tirtaatmadja, G. McKinley, and J. Cooper-White, "Drop formation and breakup of low viscosity elastic fluids: Effects of molecular weight and concentration," *Phys. Fluids (1994-present)*, 18, no., p. 043 101, 2006.

[60] R. Mun, J. Byars, and D. Boger, "The effects of polymer concentration and molecular weight on the breakup of laminar capillary jets," *J. Nonnewton. Fluid Mech.*, 74, no., pp. 285–297, 1998.

[61] M. Renardy, "Some comments on the surface-tension driven break-up (or the lack of it) of viscoelastic jets," *J. Nonnewton. Fluid Mech.*, 51, no., pp. 97–107, 1994.

[62] G. McKinley, "Visco-elasto-capillary thinning and break-up of complex fluids," *In: Bindings DM, Walters K, editors. Rheology reviews. Nuneaton: The British Society of Rheology*, no., pp. 1–48, 2005.

[63] M. Goldin, R. Pfeffer, and R. Shinnar, "Break-up of a capillary jet of a non-newtonian fluid having a yield stress," *Chem. Eng. J.*, 4, no., pp. 8–20, 1972.

[64] P. Arratia, J. Gollub, and D. Durian, "Polymeric filament thinning and breakup in microchannels," *Phys. Rev. E*, 77, no., p. 036 309, 2008.

[65] P. Arratia, L. Cramer, J. Gollub, and D. Durian, "The effects of polymer molecular weight on filament thinning and drop breakup in microchannels," *New J. Phys.*, 11, no., p. 115 006, 2009.

[66] Y. Renardy, S. Popinet, L. Duchemin, M. Renardy, S. Zaleski, C. Josserand, M. Drumright-Clarke, D. Richard, C. Clanet, and D. Quéré, "Pyramidal and toroidal water drops after impact on a solid surface," *J. Fluid Mech.*, 484, no., pp. 69–83, 2003.

[67] A. Yarin, "Drop impact dynamics: Splashing, spreading, receding, bouncing," *Annu. Rev. Fluid Mech.*, 38, no., pp. 159–192, 2006.

[68] E. Villermaux and B. Bossa, "Single-drop fragmentation determines size distribution of raindrops," *Nature Phys.*, 5, no., pp. 697–702, 2009.

[69] S. Perrard, Y. Couder, E. Fort, and L. Limat, "Leidenfrost levitated liquid tori," *EPL (Europhys. Lett.)*, 100, no., p. 54 006, 2012.

[70] B. Texier, K. Piroird, D. Quéré, and C. Clanet, "Inertial collapse of liquid rings," *J. Fluid Mech.*, 717, no., R3, 2013.

[71] J. McGraw, J. Li, D. Tran, A.-C. Shi, and K. Dalnoki-Veress, "Plateau-rayleigh instability in a torus: Formation and breakup of a polymer ring," *Soft Matter*, 6, no., pp. 1258–1262, 2010.

[72] H. Mehrabian and J. Feng, "Capillary breakup of a liquid torus," *J. Fluid Mech.*, 717, no., pp. 281–292, 2013.

[73] M. Zabarankin, O. Lavrenteva, and A. Nir, "Liquid toroidal drop in compressional stokes flow," *Journal of Fluid Mechanics*, 785, no., pp. 372–400, 2015.

[74] A. Utada, A. Fernandez-Nieves, H. Stone, and D. Weitz, "Dripping to jetting transitions in coflowing liquid streams," *Phys. Rev. Lett.*, 99, no., p. 094 502, 2007.

[75] E. Castro-Hernandez, V. Gundabala, Fernández-Nieves, and J. Gordillo, "Scaling the drop size in coflow experiments," *New J. Phys.*, 11, no., p. 075 021, 2009.

[76] J. Plateau, *Statique expérimentale et théorique des liquides soumis aux seules forces moléculaires*. Gauthier-Villars, 1873, vol. 2.

[77] J.-J. Shu and A. Chwang, "Generalized fundamental solutions for unsteady viscous flows," *Phys. Rev. E*, 63, no., p. 051 201, 2001.

[78] R. Adrian and J. Westerweel, *Particle image velocimetry*, 30. Cambridge University Press, 2011.

[79] G. Batchelor, *An introduction to fluid dynamics*. Cambridge University Press, 2000.

[80] J. Hadamard, "Mouvement permanent lent dune sphere liquide et visqueuse dans un liquide visqueux," *C. R. Acad. Sci.*, 152, no., pp. 1735–1738, 1911.

[81] V. Levich, *Physicochemical hydrodynamics*. Prentice Hall, 1962.

[82] R. Clift, J. Grace, and M. Weber, *Bubbles, drops, and particles*. Courier Corporation, 2005.

[83] H. Sawistowski, "Surface-tension-induced interfacial convection and its effect on rates of mass transfer," *Chemie Ingenieur Technik*, 45, no., pp. 1093–1098, 1973.

[84] M. Sussman, P. Smereka, and S. Osher, "A level set approach for computing solutions to incompressible two-phase flow," *J. Comput. Phys.*, 114, no., pp. 146–159, 1994.

[85] S. Khuri and A. Wazwaz, "On the solution of a partial differential equation arising in stokes flow," *Appl. Math. Comput.*, 85, no., pp. 139–147, 1997.

[86] S. Majumdar and M. O'Neill, "On axisymmetric stokes flow past a torus," *Z. Angew. Math. Phys.*, 28, no., pp. 541–550, 1977.

[87] S. Khuri, "Biorthogonality condition for axisymmetric stokes flow in a toroidal region," *Appl. Math. Comput.*, 97, no., pp. 255–259, 1998.

[88] H. Masoud and J. Felske, "Analytical solution for stokes flow inside an evaporating sessile drop: Spherical and cylindrical cap shapes," *Phys. Fluids*, 21, no., p. 042 102, 2009.

[89] W. Hicks, "On toroidal functions," *Philos. Trans. R. Soc. Lond.*, 172, no., pp. 609–652, 1881.

[90] A. Basset, "On toroidal functions," *Am. J. Math.*, 15, no., pp. 287–302, 1893.

[91] A. Mitchell and D. Griffiths, *The finite difference method in partial differential equations*. John Wiley, 1980.

[92] J. Zeleny, "Instability of electrified liquid surfaces," *Phys. Rev.*, 10, no., p. 1, 1917.

[93] R. Collins, J. Jones, M. Harris, and O. Basaran, "Electrohydrodynamic tip streaming and emission of charged drops from liquid cones," *Nature Phys.*, 4, no., pp. 149–154, 2008.

[94] A. Neukermans, "Stability criteria of an electrified liquid jet," *J. Appl. Phys.*, 44, no., pp. 4769–4770, 1973.

[95] J. López-Herrera and A. Ganan-Calvo, "A note on charged capillary jet breakup of conducting liquids: Experimental validation of a viscous one-dimensional model," *J. Fluid Mech.*, 501, no., pp. 303–326, 2004.

[96] M. Hohman, M. Shin, G. Rutledge, and M. Brenner, "Electrospinning and electrically forced jets. i. stability theory," *Phys. Fluids*, 13, no., pp. 2201–2220, 2001.

[97] J. Doshi and D. Reneker, "Electrospinning process and applications of electrospun fibers," *J. Electrostat.*, 35, no., pp. 151–160, 1995.

[98] D. Reneker, A. Yarin, H. Fong, and S. Koombhongse, "Bending instability of electrically charged liquid jets of polymer solutions in electrospinning," *J. Appl. Phys.*, 87, no., pp. 4531–4547, 2000.

[99] D. Li and Y. Xia, "Electrospinning of nanofibers: Reinventing the wheel?" *Adv. Mater.*, 16, no., pp. 1151–1170, 2004.

[100] J. Jackson, *Electrodynamics*. Wiley Online Library, 1975.

[101] J. Hernandes and A. Assis, "Electric potential for a resistive toroidal conductor carrying a steady azimuthal current," *Phys. Rev. E*, 68, no., p. 046 611, 2003.

[102] A. Barrero, J. Lopez-Herrera, A. Boucard, I. Loscertales, and M. Marquez, "Steady cone-jet electrosprays in liquid insulator baths," *J. Colloid Interface Sci.*, 272, no., pp. 104–108, 2004.

[103] J. Eggers and E. Villermaux, "Physics of liquid jets," *Rep. Prog. Phys.*, 71, no., p. 036 601, 2008.

[104] P. Saffman and G. Taylor, "The penetration of a fluid into a porous medium or hele-shaw cell containing a more viscous liquid," 245, no., pp. 312–329, 1958.

[105] S. Hill, "Channeling in packed columns," *Chem. Eng. Sci.*, 1, no., pp. 247–253, 1952.

[106] F. Orr and J. Taber, "Use of carbon dioxide in enhanced oil recovery," *Science*, 224, no., pp. 563–570, 1984.

[107] A. White and T. Ward, "Co2 sequestration in a radial hele-shaw cell via an interfacial chemical reaction," *Chaos*, 22, no., p. 037 114, 2012.

[108] G. Homsy, "Viscous fingering in porous media," *Ann. Rev. Fluid Mech.*, 19, no., pp. 271–311, 1987.

[109] C. Stauffer, "The measurement of surface tension by the pendant drop technique," *J. Phys. Chem.*, 69, no., pp. 1933–1938, 1965.

[110] L. Paterson, "Radial fingering in a hele shaw cell," *J. Fluid Mech.*, 113, no., pp. 513–529, 1981.

[111] I. Bischofberger, R. Ramachandran, and S. R. N., "An island of stability in a sea of fingers: Emergent global features of the viscous-flow instability," *Soft Matter*, 11, no., pp. 7428–7432, 2015.

[112] H. Stone, "Interfaces: In fluid mechanics and across disciplines," *J. Fluid Mech.*, 645, no., pp. 1–25, 2010.

[113] A. Buka and P. Palffy-Muhoray, "Stability of viscous fingering patterns in liquid crystals," *Phys. Rev. A*, 36, no., p. 1527, 1987.

[114] CARBOWAX. (2011). Polyethylene glycol (peg) 8000, (visited on 05/03/2017).

[115] A. Sauret and H. Shum, "Forced generation of simple and double emulsions in all-aqueous systems," *Appl. Phys. Lett.*, 100, no., p. 154 106, 2012.

[116] Y. Song and H. Shum, "Monodisperse w/w/w double emulsion induced by phase separation," *Langmuir*, 28, no., pp. 12 054–12 059, 2012.

[117] A. Utada, A. Fernandez-Nieves, J. Gordillo, and D. Weitz, "Absolute instability of a liquid jet in a coflowing stream," *Phys. Rev. Lett.*, 100, no., p. 014 502, 2008.

[118] B. Song and J. Springer, "Determination of interfacial tension from the profile of a pendant drop using computer-aided image processing: 2. experimental," *J. Colloid Interface Sci.*, 184, no., pp. 77–91, 1996.

[119] D. Papageorgiou, "On the breakup of viscous liquid threads," *Phys. Fluids*, 7, no., pp. 1529–1544, 1995.

[120] R. Christensen, "Theory of viscoelasticity," no., 1982.

[121] S. Anna and G. McKinley, "Elasto-capillary thinning and breakup of model elastic liquids," *J. Rheol.*, 45, no., pp. 115–138, 2001.

[122] T. Tanaka, "Phase transitions in gels and a single polymer," *Polym.*, 20, no., pp. 1404–1412, 1979.

[123] E. Pairam, H. Le, and A. Fernández-Nieves, "Stability of toroidal droplets inside yield stress materials," *Phys. Rev. E*, 90, no., p. 021 002, 2014.

[124] G. Vazquez, E. Alvarez, and J. Navaza, "Surface tension of alcohol+ water from 20 to 50 c," *J. Chem. Eng. Data*, 40, no., 1995.

[125] T. Young, "An essay on the cohesion of fluids," *"Philos. Trans. R. Soc. Lond. B Biol. Sci.*, 95, no., pp. 65–87, 1804.

[126] P. d. Laplace, *Mecanique Celeste, Vol. 4*. 1805.

[127] F. Hansen and G. Rødsrud, "Surface tension by pendant drop: I. a fast standard instrument using computer image analysis," *J. Colloid interface Sci.*, 141, no., pp. 1–9, 1991.

[128] E. Kreyszig, "Principal normal, curvature, osculating circle," *Differential Geometry. New York: Dover*, no., pp. 34–36, 1991.

[129] A. Domínguez, A. Fernández, N. González, E. Iglesias, and L. Montenegro, "Determination of critical micelle concentration of some surfactants by three techniques," *J. Chem. Educ.*, 74, no., p. 1227, 1997.

[130] R. Williams, J. Phillips, and K. Mysels, "The critical micelle concentration of sodium lauryl sulphate at 25 c," *Trans. Faraday Soc*, 51, no., pp. 728–737, 1955.

[131] M. Uematsu and E. Frank, "Static dielectric constant of water and steam," *J. Phys. Chem. Ref. Data*, 9, no., pp. 1291–1306, 1980.

[132] H. Zhang, M. Edirisinghe, and S. Jayasinghe, "Flow behaviour of dielectric liquids in an electric field," *J. Fluid Mech.*, 558, no., pp. 103–111, 2006.

[133] G. Arfken and H. Weber, *Mathematical methods for physicists international student edition*. Academic press, 2005.

[134] J. Gao and B. Frisken, "Cross-linker-free n-isopropylacrylamide gel nanospheres," *Langmuir*, 19, no., pp. 5212–5216, 2003.

[135] H. Bachman, A. Brown, K. C. Clarke, K. Dhada, A. Douglas, C. Hansen, E. Herman, J. Hyatt, P. Kodlekere, Z. Meng, S. Saxena, M. Spears Jr, N. Welsch, and L. Lyon, "Ultrasoft, highly deformable microgels," *Soft Matter*, 11, no., pp. 2018–2028, 2015.

[136] A. Douglas, A. Fragkopoulos, M. Gaines, L. Lyon, A. Fernandez-Nieves, and T. Barker, "Dynamic assembly of ultrasoft colloidal networks enables cell invasion within restrictive fibrillar polymers," *Proc. Nat. Acad. Sci.*, 114, no., pp. 885–890, 2017.

[137] N. Otsu, "A threshold selection method from gray-level histograms," *IEEE Trans. Syst., Man, Cybern.*, 9, no., pp. 62–66, 1979.

[138] R. Van Uitert and I. Bitter, "Subvoxel precise skeletons of volumetric data based on fast marching methods," *Med. Phys.*, 34, no., pp. 627–638, 2007.

[139] M. Hassouna and A. Farag, "Multistencils fast marching methods: A highly accurate solution to the eikonal equation on cartesian domains," *IEEE Trans. Pattern Anal. Mach. Intell*, 29, no., 2007.

[140] H. Schild, "Poly (n-isopropylacrylamide): Experiment, theory and application," *Prog. Polym. Sci.*, 17, no., pp. 163–249, 1992.

VITA

Alexandros Alkiviadis Fragkopoulos was born August 1st, 1989 in Thessaloniki, Greece. He attended Mandoulides for primary and secondary school in Greece. In 2007, he left Greece to study abroad at Bard College in Annandale-on-Hudson, New York, receiving a dual Batchelor degrees in Physics and Mathematics. In 2011, he started his doctoral studies under the supervision of Prof. Alberto Fernandez-Nieves at the Georgia Institute of Technology.